The Abdus Salam
International Centre for Theoretical Physics

United Nations
Educational, Scientific and
Cultural Organization

IAEA
International Atomic Energy Agency

2167-8

Advanced School on Direct and Inverse Problems of Seismology

27 September - 8 October, 2010

Geophysical & Petrological Modelling of the Structure & Composition of the Crust & Upper Mantle in Complex Geodynamic Settings
The Tyrrhenian Sea & Surroundings

A. Peccerillo
Dept. of Earth Sciences
University of Perugia
Perugia
ITALY

Available online at www.sciencedirect.com
ScienceDirect
Earth-Science Reviews 80 (2007) 1–46
EARTH-SCIENCE REVIEWS
www.elsevier.com/locate/earscirev

Geophysical and petrological modelling of the structure and composition of the crust and upper mantle in complex geodynamic settings: The Tyrrhenian Sea and surroundings

G.F. Panza [a,b,*], A. Peccerillo [c,1], A. Aoudia [a,b,2], B. Farina [a]

[a] *Dipartimento di Scienze della Terra, Università degli Studi di Trieste, Trieste, Italy*
[b] *The Abdus Salam International Centre for Theoretical Physics, Earth System Physics Section, Trieste, Italy*
[c] *Dipartimento di Scienze della Terra, Università degli Studi di Perugia, Perugia, Italy*

Received 19 January 2006; accepted 2 August 2006
Available online 13 November 2006

Abstract

Information on the physical and chemical properties of the lithosphere–asthenosphere system (LAS) can be obtained by geophysical investigation and by studies of petrology–geochemistry of magmatic rocks and entrained xenoliths. Integration of petrological and geophysical studies is particularly useful in geodynamically complex areas characterised by abundant and compositionally variable young magmatism, such as in the Tyrrhenian Sea and surroundings.

A thin crust, less than 10 km, overlying a soft mantle (where partial melting can reach about 10%) is observed for Magnaghi, Vavilov and Marsili, which belong to the Central Tyrrhenian Sea backarc volcanism where subalkaline rocks dominate. Similar characteristics are seen for the uppermost crust of Ischia. A crust about 20 km thick is observed for the majority of the continental volcanoes, including Amiata–Vulsini, Roccamonfina, Phlegraean Fields–Vesuvius, Vulture, Stromboli, Vulcano–Lipari, Etna and Ustica. A thicker crust is present at Albani – about 25 km – and at Cimino–Vico–Sabatini — about 30 km. The structure of the upper mantle, in contrast, shows striking differences among various volcanic provinces.

Volcanoes of the Roman region (Vulsini–Sabatini–Alban Hills) sit over an upper mantle characterised by V_s mostly ranging from about 4.2 to 4.4 km/s. At the Alban Hills, however, slightly lower V_s values of about 4.1 km/s are detected between 60 and 120 km of depth. This parallels the similar and rather homogeneous compositional features of the Roman volcanoes, whereas the lower V_s values detected at the Alban Hills may reflect the occurrence of small amounts of melts within the mantle, in agreement with the younger age of this volcano.

The axial zone of the Apennines, where ultrapotassic kamafugitic volcanoes are present, has a mantle structure with high-velocity lid (V_s ~4.5 km/s) occurring at the base of a 40-km-thick crust. Beneath the Campanian volcanoes of Vesuvius and Phlegraean Fields, the mantle structure shows a rigid body dipping westward, a feature that continues southward, up to the eastern Aeolian arc. In contrast, at Ischia the upper mantle contains a shallow low-velocity layer (V_s=3.5–4.0 km/s) just beneath a thin but complex crust. The western Aeolian arc and Ustica sit over an upper mantle with V_s ~ 4.2–4.4 km/s, although a rigid layer (V_s=4.55 km/s) from about 80 to 150 km occurs beneath the western Aeolian arc. In Sardinia, no significant differences in the LAS structure are detected from north to south.

* Corresponding author. Dipartimento di Scienze della Terra, Università degli Studi di Trieste, Trieste, Italy. Fax: +39 405582111.
E-mail addresses: panza@dst.units.it (G.F. Panza), pecceang@unipg.it (A. Peccerillo), aoudia@dst.units.it (A. Aoudia), farinabm@dst.units.it (B. Farina).
[1] Fax: +39 755852603.
[2] Fax: +39 405582111.

0012-8252/$ - see front matter
doi:10.1016/j.earscirev.2006.08.004

The petrological–geochemical signatures of Italian volcanoes show strong variations that allow us to distinguish several magmatic provinces. These often coincide with mantle sectors identified by V_s tomography. For instance, the Roman volcanoes show remarkable similar petrological and geochemical characteristics, mirroring similar structure of the LAS. The structure and geochemical-isotopic composition of the upper mantle change significantly when we move to the Stromboli–Campanian volcanoes. The geochemical signatures of Ischia and Procida volcanoes are similar to other Campanian centres, but Sr–Pb isotopic ratios are lower marking a transition to the backarc mantle of the Central Tyrrhenian Sea. The structural variations from Stromboli to the central (Vulcano and Lipari) and western Aeolian arc are accompanied by strong variations of geochemical signatures, such as a decrease of Sr-isotope ratios and an increase of Nd-, Pb-isotope and LILE/HFSE ratios. The dominance of mafic subalkaline magmatism in the Tyrrhenian Sea basin denotes large degrees of partial melting, well in agreement with the soft characteristics of the uppermost mantle in this area. In contrast, striking isotopic differences of Plio-Quaternary volcanic rocks from southern to northern Sardinia does not find a match in the LAS geophysical characteristics.

The combination of petrological and geophysical constraints allows us to propose a 3D schematic geodynamic model of the Tyrrhenian basin and bordering volcanic areas, including the subduction of the Ionian–Adria lithosphere in the southern Tyrrhenian Sea, and to place constraints on the geodynamic evolution of the whole region.

Keywords: surface waves tomography; lithosphere–asthenosphere system; petrological–geophysical model; Tyrrhenian Sea; Italian volcanic provinces; magma sources; geodynamic model

1. Introduction

The structure and composition of the crust and upper mantle depend on the past geological history of a region and can be extremely variable both vertically and laterally. Understanding the structure of the lithosphere–asthenosphere system (LAS) is fundamental for gaining a better insight into several processes, including volcanism and seismicity, but also for unravelling the past geodynamic history of large regions. Information on the properties of the upper mantle and lower crust can be gained by geophysical investigations. Seismic wave velocities and gravimetric data are extensively used to investigate crustal and mantle structure (e.g., Christensen and Mooney, 1995).

Equally important information can be obtained from petrological and geochemical studies of magmas and of high-pressure xenoliths entrained in volcanic rocks (e.g., Nixon, 1987; Wilson, 1988 with references). Magmas are generated at various depths, from middle–upper crust to the asthenosphere, and are important potential carrier of information on the composition of the entire LAS (e.g., McNutt, 1998; Anderson, 2000). Ultramafic xenoliths represent samples of deep-seated rocks and provide direct evidence on the mineralogical and chemical characteristics of the lithosphere (e.g., Nixon, 1987; Menzies, 1990).

Most of the models of the Earth interior are based on single sets of either geophysical or petrological data, whereas integrated petrological, geochemical and geophysical studies are less frequent (e.g., Peccerillo and Panza, 1999). Yet, such an integrated approach is potentially able to furnish the maximum of information on the composition of LAS.

Combined petrological, geochemical and geophysical studies are particularly useful in complex areas where young and compositionally variable magmatism occurs. The careful study of the petrology and geochemistry of volcanic rocks can give information on composition and evolution history of magma source regions and on geodynamic setting of magma genesis. The parallel study of the mechanical characteristics of the lithosphere–asthenosphere can furnish data on amount of fluid present, vertical and lateral heterogeneities. Integration of these data gives a holistic model of the internal structures of the Earth, which optimizes the probability to match reality.

A particularly suitable area for applying the integrated petrological–geophysical approach to the study of LAS is the Tyrrhenian Sea area and the surrounding Apennines and Sardinia block. This is a particularly intriguing zone whose unique geological complexity is well expressed by the wide variety of Plio-Quaternary magmatic rocks (Table 1), which reveal the strong heterogeneity of the crust–mantle system (e.g., Peccerillo and Panza, 1999; Peccerillo, 2003, 2005). The setting is the result of the complex geodynamic evolution, which affected the Mediterranean during Neogene and Quaternary times (e.g., Doglioni et al., 1999) and generated a mosaic of compositionally and structurally distinct mantle domains that have undergone different evolutionary histories, in terms of compositional and structural modifications.

The geodynamic evolution of the Mediterranean area, as well as of other geologically complex settings, can be hardly unravelled when making use of models based on specialized single disciplines. This is due to the structure

Table 1
Summary of ages and petrological characteristics of Plio-Quaternary volcanic provinces in the Tyrrhenian Sea area. Ages in Ma are given in parentheses. Modified after Peccerillo (2005) and references therein

Magmatic province	Main magmatic centres and ages (in Ma)	Petrology
Tuscany (8 to 0.2 Ma)	*Acid intrusions*: Elba (8.5–6.8), Montecristo (7.1), Giglio (5), Campiglia–Gavorrano (5.9–4.3) *Acid volcanoes*: San Vincenzo (4.5), Roccastrada (2.5), Amiata (0.2), Cimini (1.3–0.9), Tolfa (3.5) *Mafic centres*: Capraia (7.6–4.6), Orciatico and Montecatini (4.1), Radicofani (1.3), Torre Alfina (0.9–0.8). Sisco (Corsica, 14 Ma)	– *Acid rocks*: hypabyssal intrusive and extrusive rocks formed by crustal anatexis or by mixing between crustal melts and calcalkaline to ultrapotassic mafic magmas. – *Mafic rocks*: extrusive and hypabyssal subvolcanic bodies with calcalkaline, potassic and ultrapotassic (*lamproitic*) composition. Also present as mafic enclaves in several acid intrusive and extrusive rocks.
Intra-Apennine (0.6 to 0.3 Ma)	San Venanzo (0.26), Cupaello (0.64), Polino (0.25), Acquasparta, Oricola (0.53) etc.	– Monogenic pyroclastic centres and rare lavas with an ultrapotassic melilititic (*kamafugite*) composition.
Roman Province (Latium) (0.8 to 0.02 Ma)	Vulsini (0.6–0.15), Vico (0.4–0.1), Sabatini (0.8–0.04), Colli Albani (0.6–0.02)	– Large volcanic complexes formed of potassic (trachybasalt to trachyte) and ultrapotassic (leucite tephrite to phonolite) pyroclastic rocks and minor lavas.
Ernici–Roccamonfina (0.7 to 0.1 Ma)	Ernici: Pofi, Ceccano, Patrica, etc. (0.7–0.1), Roccamonfina (0.58–0.1)	– Monogenetic pyroclastic and lava centres (Ernici), and a stratovolcano (Roccamonfina) formed of mafic to felsic ultrapotassic and potassic rocks exhibiting large variations of trace element abundances and radiogenic isotope signatures.
Campania and Pontine Islands (1 Ma to Present)	Somma–Vesuvio (0.03–1944 AD), Campi Flegrei (0.3–1538 AD), Ischia (0.15–1302 AD), Procida (0.05–0.01), Ventotene (0.8–0.1), younger Ponza (1).	– Shoshonitic, potassic (trachybasalt to trachyte) and ultrapotassic (leucite tephrite to phonolite) rocks forming stratovolcanoes and multi-centre complexes (Campi Flegrei, Ischia).
Vulture (0.8 to 0.1 Ma)	Vulture, Melfi	– Stratovolcano and a few parasitic centres formed by Na–K-rich tephrites, phonolites, foidites with haüyne. Possible carbonatite.
Aeolian arc (1 or 0.4 Ma to present)	Alicudi (0.06–0.03), Filicudi (1(?)–0.04), Salina (0.4–0.013), Vulcano (0.12–1888 AD), Lipari (0.2–580 AD), Panarea (0.15–0.05), Stromboli (0.2–Present)	– Stratovolcanoes with dominant calc-alkaline (basalt–andesite–rhyolite) and shoshonitic (basalt to rhyolite) compositions, with a few potassic alkaline products. Shoshonites are concentrated in the central–eastern sector of the arc.
Sicily (7 Ma to Present)	Etna (0.5–Present), Iblei (7–1.5), Ustica (0.75–0.13), Pantelleria (0.3–0.005), Linosa (1–0.5), Sicily Channel seamounts (Miocene to Present)	– Stratovolcanoes, diatremes, small plateaux, etc. formed of tholeiitic and Na-alkaline rocks (basanite, hawaiite, trachyte, peralkaline trachyte and rhyolite).
Sardinia (5.3 to 0.1)	Capo Ferrato (~5), Montiferro (4–2), Orosei–Dorgali (4–2), Monte Arci (3.7–2.3), Logudoro (3–0.1)	– Stratovolcanoes, basaltic plateaux and monogenetic centres composed of subalkaline and alkaline rocks mainly with Na affinity, and displaying strong trace element and radiogenic isotope variation from north to south.
Tyrrhenian Sea floor (12 Ma to Present)	Cornacya (12), Magnaghi (3), Marsili (1.8–0), Vavilov, Aceste, Anchise, Lametini, Palinuro, older Ponza (4.2), etc.	– Coexisting intraplate (oceanic tholeiites, Na-transitional and alkaline) and arc-type (arc-tholeiitic, calc-alkaline, potassic) rocks, with arc rocks becoming younger from west to south-east.

and composition variability of the LAS and to the intrinsic non-uniqueness of the inverse problem that is at the base of any geological model.

In this paper, we combine geophysical and petrological–geochemical data to work out a model for the LAS of the Central Mediterranean area. Petrological–geochemical discussion will be focused on Plio-Quaternary volcanic rocks, since mantle xenoliths are present only in few volcanoes and have not been extensively studied as volcanic rocks. The Italian area and surrounding regions are particularly suitable for this study, because of the large concentration of well studied volcanic centres and a wealth of surface wave tomography studies. We show that distinct physical structure of the LAS parallels compositional variability of volcanic rocks observed at the surface. The implication of the LAS model for evolution of the Tyrrhenian Sea and surroundings is discussed.

2. Methodological background

2.1. Petrology and geochemistry

The lower crust and the upper mantle (both lithospheric and asthenospheric) are the main sources of magmas erupted at the surface. Major, trace element and isotopic compositions of magmas can give important information on the composition and depths of their sources. An enormous amount of studies has been carried out with the aim of constraining compositions of source rocks and pressure conditions of magma generation. Much of the studies have been carried out on basaltic rocks, especially tholeiites from mid-ocean ridges, but a large quantity of data also exists on crustal anatectic rocks and on exotic magma types such as ultrapotassic rocks, kimberlites and carbonatites (e.g., Wendlandt and Eggler, 1980; Edgar, 1987; Gudfinnsson and Presnall, 2005). Although the results of different studies appear sometimes conflicting, for instance as regards the role of water on silica contents of magmas (e.g., Kushiro, 1990; Gaetani and Grove, 1998), the information available allows us to place constraints on the physico-chemical conditions (i.e., pressure, temperature, nature and abundance of fluid components) during magma genesis both in the mantle and in the crust.

It is beyond the scopes of this paper to provide a review of these studies. However, a few basic principles of igneous petrology and geochemistry will be given, in order to elucidate robustness of petrological–geochemical constraints on processes of magma genesis and on compositions of their sources. We will first consider primary magmas and will explore how major, trace element and isotope data can furnish information on physico-chemical conditions during petrogenesis and on source composition. Successively, the effects of shallow level processes on modification of primary magmas will be discussed. Contrary to the information from study of high-pressure xenoliths, evidence on the internal of the Earth arising from studies of magmas is indirect, and is based on experimental studies and on theories of element and isotope behaviour during magmatic processes. Such an approach is unavoidable for volcanic areas such as the Tyrrhenian Sea and surroundings, where mantle xenoliths are rare, restricted to a very few volcanoes, and not well studied from geochemical and isotopic point of view.

Major element, trace element and isotopic data of magmatic rocks are three distinct and somewhat independent types of compositional parameters, which should be always considered simultaneously by any study of igneous rocks. Their values depend on different factors acting during magma genesis and evolution. Therefore, they furnish distinct and complementary information on the origin and evolution of magmas.

2.2. Major elements

Major elements are the main chemical constituents of magmas. Their concentrations, expressed as wt.% of element oxides (SiO_2, TiO_2, Al_2O_3, Fe_2O_3, FeO, MnO, MgO, CaO, Na_2O, K_2O, P_2O_5, H_2O), are variable and range from a fraction of percent to some 70–80 wt.%. Major element abundances of primary magmas (i.e. of those magmas that have not suffered any compositional modification after their formation by partial melting or anatexis of source rocks) depend on the composition and relative amounts of the mineral phases that enter into the melt during anatexis. These, in turn, are a function of the abundances of minerals in the source rocks and on physico-chemical conditions during anatexis. Modalities of melt extraction from the parent rock also play an important role. In general terms, melts can be left in contact and continuously react and re-equilibrate with the residuum (equilibrium or batch melting), or may be removed and isolated from the source as soon as they are formed (fractional or Rayleigh melting). Probably, the most common case in nature is somewhat between these two extremes.

The relationships between these factors and the major element composition of magmas can be better understood by using simplified two- or three-component phase diagrams. Fig. 1 shows the forsterite (Mg_2SiO_4)-diopside ($CaMgSi_2O_6$)-silica (SiO_2) phase relationships at high pressure, and is useful to investigate mantle melting and the generation of

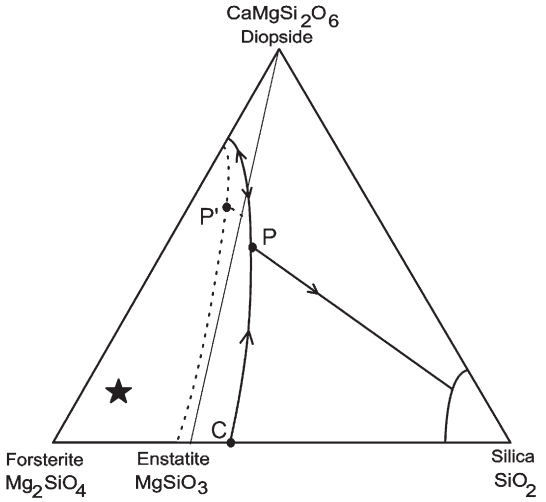

Fig. 1. Diagram showing simplified phase relationships for Forsterite–Diopside–Silica. *P* is a relative minimum temperature (peritectic point), and represents compositions of early formed liquids at 2 Gpa in wet conditions, starting from parent rocks whose composition lies in the subtriangle Forsterite–Diopside–Enstatite. *P′* is the position of minimum-temperature point in dry conditions or in the presence of CO_2. Curves represent paths of liquid compositional modifications with ongoing equilibrium melting after a mineral phase has been consumed. Arrows indicate decreasing temperature. For further explanation, see text.

basaltic magmas (Yoder, 1976). The subtriangle forsterite (Fo) – diopside (Di) – enstatite (En) contains ultramafic rocks such as mantle peridotite. A lherzolite (olivine+clinopyroxene+orthopyroxene) upper mantle plots within the Fo–Di–En subtriangle and is indicated by a star in Fig. 1. Point *P* is called peritectic point, and indicates the major element composition of liquids formed by melting of any rock falling in the subtriangle Fo–Di–En. The position of the peritectic point indicates that early liquids from a lherzolite are strongly enriched in the diopside component with respect to the source rock. In other words, diopside contributes more strongly to the melt than coexisting enstatite and forsterite. However, the position of the peritectic point changes with pressure and the nature of fluid present. At upper mantle pressure and hydrous conditions or also at low pressure, the peritectic point lies on the right of the Di–En join, in the subtriangle En–Di–Silica. This means that early melts formed at low pressure or at high-pressure hydrated conditions are oversaturated in silica. In contrast, at high pressure and dry or CO_2-saturated conditions, there is a reduction of the stability field of olivine (dashed line in Fig. 1) and the peritectic point shifts to the left of the Di–En join (*P′* in Fig. 1), inside the subtriangle Fo–Di–En. This means that liquids formed at *P′* are undersaturated in silica. In general, a positive relationship between pressure of melting and degree of silica undersaturation of magmas has been found by studies on several types of mantle rocks. Therefore, the degree of silica saturation can be taken as a parameter to estimate depths of magma generation for both "normal" and anomalous mantle rocks (e.g., containing exotic phases such as phlogopite or K-richterite; Wendlandt and Eggler, 1980; Melzer and Foley, 2000; Green and Falloon, 2005).

Additional important information arising from phase diagrams is how the composition of liquids changes with ongoing melting. For equilibrium melting, liquid composition remains at the point *P* (or *P′*) until a phase disappears completely (generally, it first happens for diopside, which more heavily contributes to melting). Successively melt composition changes along the line *P–C*, until a second mineral phase (generally orthopyroxene) disappears. Small melt fraction extracted continuously during fractional melting also has a composition at *P* (or *P′*). When diopside is completely melted, the residual rock consists of forsterite and orthopyroxene (harzburgite) and can be represented by a simple binary Forsterite–Silica phase diagram (not shown). Forsterite and Silica have enstatite as an intermediate product. Melting of an harzburgite occurs at much higher temperature than lherzolite. Enstatite melts incongruently (i.e., it gives a liquid plus forsterite) and generates mafic melts whose composition shows lower CaO wt.%, since melting is dominated by En that contains very little CaO, and higher MgO wt.% than melts formed from lherzolite. In summary, whereas batch melting generates liquids showing continuous major element variations, fractional melting gives somewhat bimodal liquid compositions. However, in both cases, liquids formed before a phase disappears show poorly variable major element composition, independently of the degree of partial melting. As it will be pointed out later, this is not the case for trace elements.

It must be pointed out that natural processes are much more complex than described above. For example, number of components in the real rocks is higher than number of phases and melting is not expected to occur at a single invariant point (e.g., Presnal, 1979). Moreover, most of the mineral phases occurring in nature are not pure compositions, but represent solid solutions between two or more end-members. Therefore, their compositions do not remain constant but change continuously during partial melting. The best known case is that of olivine, a major phase of the upper mantle. It consists of a solid solution of forsterite (Mg) and fayalite (Fe), and becomes increasingly richer in MgO

with ongoing fractional melting. As a result, also magmas generated later in the course of melting process become progressively richer in MgO. Clinopyroxenes also have intermediate compositions among various end-members and may contain high amounts of Na_2O and Al_2O_3, whose abundances change during melting (e.g., Konzett and Ulmer, 1999). Another important complexity arises from the presence of other minerals in addition to those reported in phase diagrams. In the upper mantle, spinel (or plagioclase or garnet), phlogopite and various types of amphiboles can occur in association with olivine and pyroxenes. Their presence strongly changes the phase relations described in the simplified diagrams of Fig. 1. Finally, melting can occur over a large rock section, whose composition may be variable. In this case the magma composition either represents the last equilibrated melt or is a sort of integrated composition of melts formed along the rock column. However, in spite of these complications, simplified diagrams allow us to understand the basic principles that govern major element composition of magmas during anatexis.

2.3. Trace elements

Trace elements are chemical components that are present at very low concentrations (parts per million, ppm, or lower) in the main phases, at a compositional level for which Henry's law is obeyed. Henry's law states that the activity of a trace element i in the host mineral j at equilibrium (a_i^j) is proportional to its concentration (x_i^j):

$$a_i^j = k_i^j x_i^j \tag{1}$$

where k_i^j is a constant. The equation that describes the variation of trace elements during batch melting (e.g., Shaw, 1970) is:

$$\frac{C_l^i}{C_0^i} = \frac{1}{D_{s/l}^i(1-F)+F} \tag{2}$$

where C_l^i is the concentration (in ppm) of the trace element i in the magma, C_0^i is the concentration of the same element in the source rock, F is the degree of partial melting, which ranges from zero (all the rock is solid) to unity (complete melting), and $D_{s/l}^i$ is the bulk partition coefficient between residual solid (i.e., the mineral phases left unmelted in the residue) and the coexisting liquid phase for the trace element i. $D_{s/l}^i$ is the sum of partition coefficients of the single mineral phases, for the particular element i ($K_{m/l}^i$), times the weight proportions of the single minerals present in the residue (X_m%):

$$D_{s/l}^i = \sum K_{m/l}^i X_m\% \tag{3}$$

where $K_m^i = C_m^i / C_l^i$, i.e. is the ratio between the abundance of the element i in a single residual mineral and in the coexisting liquid, which is determined experimentally for the various minerals–melt pairs for the element i.

Some elements have a tendency to go preferentially into the liquid rather than remaining in any solid phase (i.e., $D_{s/l}<1$). These elements are known as *incompatible* and, for normal mantle minerals, include Th, U, Ta, Nb, Rb, Ba, Light Rare Earth Elements (LREE), Zr, etc. Compatible elements, in contrast, preferentially remain in the solid phases rather than going into the melt (i.e., $D_{s/l}>1$). Compatible trace elements for mantle mineralogy include Ni, Cr, Co, and Sc. For strongly incompatible elements ($D_{s/l}^i \approx 0$) Eq. (2) becomes:

$$\frac{C_l^i}{C_0^i} \approx \frac{1}{F} \tag{4}$$

Eqs. (2) and (4) indicate that the concentration of a given trace element in a primary magma depends on the initial concentration of the element in the source rock, the degree of partial melting and the solid/liquid partition coefficients of the phases that are left in the residue after partial melting. For strongly incompatible elements, the abundances in the melt depend essentially on the composition of parent rock and on the degree of partial melting. A main point to make clear is that, whatever the degree of compatibility or incompatibility, the above equations show that the factors governing trace element distribution in the magmas are different from those of major elements. Therefore, information on magma genesis arising from trace elements are different and complementary with respect to those obtained from major elements.

Simple handling of Eq. (4) leads to conclude that concentration ratios of strongly incompatible elements i and j are equal to the ratio of the same elements in the source rock and remain constant with changing degree of partial melting:

$$\frac{C_l^i}{C_l^j} \approx \frac{C_0^i}{C_0^j} \approx \text{constant} \tag{5}$$

There are several problems in nature that make use of trace elements, much more complex than indicated by equations reported above. For instance, determining

the degree of partial melting of a source rock requires that the initial concentration of trace elements in the source should be known, something which is difficult to achieve. Most inferences on degrees of partial melting of magmas within the mantle are drawn by assuming near chondritic composition for source rocks. This is acceptable only for large degrees of partial melting over wide regions in the asthenosphere, but it is hardly applicable to alkaline and ultra-alkaline magmas such as ultrapotassic melts, which are formed by localised and probably small degrees of melting of compositionally anomalous portions of the upper mantle. Other problems may arise from uncertainties about the values of bulk partition coefficients, especially when accessory phases are present in the residue (e.g., Allegre and Minster, 1978).

However, ratios of incompatible elements are largely independent on most of these factors, and basically depend on the ratios of the source rocks. These, in turn, are the effect of the particular evolution history of rocks before melting events. For instance, high ratios of Large Ion Lithophile Elements (LILE; e.g., Rb, Cs, Ba) vs. High Field Strength Elements (HFSE, elements with high ratios between charge and ionic radius: Ta, Nb, Zr, Hf, Ti) observed in the volcanic rocks associated with subduction zones are believed to reflect a similar feature of the mantle wedge. This is probably related to preferential mobilisation of LILE by slab-released fluids or melts (e.g., Kessel et al., 2005). However, the presence of residual phases rich in HFSE may invalidate this conclusion (see Foley and Wheller, 1990).

2.4. Isotopic composition

Studies of isotopic compositions of igneous rocks have provided an enormous advancement in our understanding of magmatic processes and of the nature and evolution of the internal of the Earth. Isotopic ratios of several elements (e.g., $^{87}Sr/^{86}Sr$, $^{143}Nd/^{144}Nd$, $^{206}Pb/^{204}Pb$, $^{207}Pb/^{204}Pb$, $^{208}Pb/^{204}Pb$, $^{176}Hf/^{177}Hf$, $^{18}O/^{16}O$) do not change significantly or fractionate at a moderate degree during partial melting of rocks and closed-system magma crystallisation. As a consequence, magmas inherit isotopic signatures of their parent rocks, furnishing important indication on composition and evolution of magma sources.

A wealth of studies (e.g., Hofmann, 1997; Stracke et al., 2005 and references therein) have shown that the radiogenic isotopic composition of Earth's mantle is variable and depends on the complex geological processes, such as melt extraction and metasomatic enrichments. Reading the isotope code of mantle-derived rocks is, therefore, of foremost importance for unravelling the evolution history of the upper mantle.

In general, metasomatic processes within the upper mantle generate an increase of Rb/Sr, Th/Pb and U/Pb and a decrease of Sm/Nd (e.g., Hofmann, 1997). With aging, these give strongly radiogenic compositions for isotopes of these elements, i.e. high $^{87}Sr/^{86}Sr$, $^{206}Pb/^{204}Pb$, $^{207}Pb/^{204}Pb$ and $^{208}Pb/^{204}Pb$, and low $^{143}Nd/^{144}Nd$ ratios, with respect to normal mantle values. In contrast, melting events deprive the residual rocks in Th–U–Rb–Nd with respect to Pb–Sr–Sm, generating mantle reservoirs that develop low Pb and Sr isotopic ratios, and high $^{143}Nd/^{144}Nd$ with aging. These reservoirs are known as Depleted MORB Mantle (DMM), showing $^{87}Sr/^{86}Sr$ around 0.7025, $^{206}Pb/^{204}Pb$ around 17.0–18.0 and $^{143}Nd/^{155}Nd$ around 0.5135 (Zindler and Hart, 1986; Stracke et al., 2005).

Recycling within the upper mantle of crustal rocks with variable Sm/Nd, Rb/Sr, Th/Pb and U/Pb, at various stages of Earth evolution, generated a number of enriched mantle sources, which are found at a global scale. The best known mantle enriched compositions are the Enriched Mantle 1 (EM1), Enriched Mantle 2 (EM2), HIMU (high-μ, where μ stands for U/Pb ratio), and FOZO (Focal Zone) (Zindler and Hart, 1986; Stracke et al., 2005). EM1 shows moderately radiogenic Sr ($^{87}Sr/^{86}Sr \sim 0.705$), and unradiogenic Nd ($^{143}Nd/^{144}Nd \sim 0.5120$), along with poorly radiogenic Pb (e.g., $^{206}Pb/^{204}Pb \sim 17.0$), which reveal recycling and aging of crustal material characterised by low Th/Pb, U/Pb and moderate Rb/Sr and rather low Sm/Nd (e.g., lower continental crust; Lustrino and Dallai, 2003). EM2 is characterised by highly radiogenic Sr ($^{87}Sr/^{86}Sr \sim 0.710$), mildly radiogenic Pb (e.g., $^{206}Pb/^{204}Pb \sim 18.5$) and unradiogenic Nd ($^{143}Nd/^{144}Nd \sim 0.5122$), which are explained by recycling of continental crust. HIMU is characterised by unradiogenic Sr ($^{87}Sr/^{86}Sr \sim 0.703$) and radiogenic Pb (e.g., $^{206}Pb/^{204}Pb \sim 20.0–21.0$) and mildly radiogenic Nd ($^{143}Nd/^{144}Nd \sim 0.5128$), which reveals recycling of low Rb/Sr, moderate Sm/Nd and high Th/Pb and U/Pb ratios (possibly oceanic crust; see Hofmann, 1997). FOZO shows intermediate Pb–Sr–Nd isotopic ratios between HIMU and DMM-EM1 (e.g., Stracke et al., 2005).

Additional heterogeneity within the upper mantle can develop locally as a result of recent introduction of old continental crust into the mantle wedge above subducting plates. These processes can generate mantle sectors with high Sr- and low Nd-isotope ratios, not much different from EM2. Distinguishing old from recent enriched mantle compositions is far from simple and is one of the debated issues in several areas, including the

Mediterranean region (see Peccerillo and Martinotti, 2006). Very much debated is the issue of the physical nature of various mantle compositions (i.e., DMM, EM1, EM2, etc.). The main problem is whether they represent particular mantle reservoirs that are sampled by uprising plumes or they simply reflect diffused heterogeneities within the upper mantle, without any relation with mantle plumes (see Foulger et al., 2005, and website www.mantleplume.org).

2.5. Effects of evolutionary processes on magma compositions

Very few, if any, of the magmas erupted at the surface represent primary compositions. Most magmas undergo chemical modification (or diversification or evolution) during their ascent to the surface. Fractional crystallisation, assimilation of country rocks and mixing are the most important processes of magma evolution. Closed system fractional crystallisation produces strong variations of major and trace element abundances, with an increase in incompatible elements and a decrease of compatible elements. The compatibility–incompatibility of trace elements may change drastically during fractional crystallisation, depending on the nature of the major and accessory phases separating from the magmas. For common rock-forming minerals (i.e. olivine, pyroxene, plagioclase, amphibole, alkali–feldspar, foids), Th, U, Ta, Nb and Light REE (La to Sm) behave as incompatible elements, at least in the mafic compositions (e.g., Rollinson, 1998). In contrast, elements that enter readily into the lattice of mafic minerals (e.g., Ni, Co, Cr, Sc) or plagioclase (Sr) have a compatible behaviour during fractional crystallisation of these phases. The equation describing the behaviour of trace elements during fractional crystallisation is:

$$\frac{C_1^i}{C_0^i} = F^{(D-1)} \tag{6}$$

where C_1^i is the concentration of the element i in the residual liquid after separation of mineral phases, C_0^i is the concentration of the same element in the parent magma, D is the bulk partition coefficient between the separating phases and residual melt, and F is the amount of residual melt (varying from 0 for complete solidification to one for no crystallisation). For strongly incompatible elements ($D \approx 0$), the element concentration in the residual magma depends on the initial abundances and on the degree of fractionation. It is simple algebra to demonstrate that ratios of incompatible elements do not change with changing F, i.e. with ongoing crystallisation. However, major element variation during fractional crystallisation, produces a dramatic modification of melt structure (e.g., degree of melt polymerisation), which leads to important modification of partition coefficients of most trace elements for single minerals (e.g., Rollinson, 1998 and references therein). Moreover, the compatibility of elements can change dramatically with the fractionation of accessory phases, a common process in silicic magmas. Therefore, care must be taken in using trace element abundances and ratios to infer the composition of primary melts and of their source rocks, especially when magmatic systems under consideration are evolved in composition.

Radiogenic isotope signatures remain constant during closed-system fractional crystallisation. Stable isotopes undergo some fractionation (e.g., Appora et al., 2003). Overall, oxygen isotopic ratios increase by a few units per mil during fractionation from mafic to felsic compositions (e.g., Taylor and Sheppard, 1986).

Assimilation and mixing have variable effects on magma compositions. These depend on the relative proportions and compositional contrast of end-members (either liquids or solid rocks and minerals) involved in the mixing and/or assimilation. Moreover, in most cases, mixing and assimilation are accompanied by concomitant fractional crystallisation, which induces complex trace element and isotopic variations (De Paolo, 1981). In these cases, compositional signatures of primary magmas are difficult to recognise. Modification of incompatible trace element ratios and radiogenic isotope signatures during assimilation of crustal material is particularly severe for magmas, such as tholeiitic basalts, that have low concentrations of incompatible elements. In contrast, the effects of assimilation processes are much less severe for magmas that have high concentration of incompatible elements, such as the potassic magmas from the Italian peninsula. These magmas are characterised by high abundances of Sr, Pb, REE and other incompatible elements that are able to effectively buffer variations of trace element ratios and Sr–Nd–Pb isotopic signatures during assimilation of crustal rocks (Peccerillo, 2005, and references therein).

It is beyond the aim of this paper to review in detail the effects of evolution processes on magma composition, which is treated in a large number of textbooks and review papers (e.g., Wilson, 1988; Rollinson, 1998). However, a main point to emphasise here is that the use of trace element and isotopic data for the study of magma mantle sources should be restricted to poorly evolved melts whose composition is as close as possible to primary melts. Therefore, the study should focus on those rocks that have Mg# ($Mg/(Mg+Fe^{+2})$) atomic ratio close or higher than 0.70, and Ni and Cr contents higher than 250–300 ppm and 500 ppm, respectively. These values are

typical of primary or poorly evolved mantle-derived melts. Rocks with high Mg#, Ni and Cr may still not be primary, but they are the closest representative of mantle-equilibrated parental melts. Also in these cases, the nature of evolutionary processes must be quantitatively established and their effects should be cleaned out before inferring on magma source composition. Much of the following discussion is based on studies that have carefully considered the effects of evolution processes on magma compositions. Unless otherwise stated, these studies concluded that evolutionary processes have played a minor role in determining the compositions of mafic magmas observed at the surface.

3. Seismic tomography and inverse problem for earth structure retrieval

Seismic tomography is a technique to image the Earth interior with waves generated by earthquakes. The method is comparable to that applied in medical tomography although it is much more complicated because: (1) apart from a few nuclear tests, it is not in our power to locate or time the natural sources of seismic waves (earthquakes); (2) apart from a few ocean-bottom seismographs (OBS), the sensors are located on land and their distribution is discrete; (3) in seismology the ray-path is usually not straight (Nolet, 1987). As a consequence of (1) and (2), some areas are sampled by wave paths that mostly go along some preferred direction, while others are not sampled, with obvious consequences of the resolving power of the data.

For the simultaneous inversion of earthquake and velocity parameters, Crosson (1976) worked out the problem for one dimension and, independently, Aki and Lee (1976) published a 3D inversion method. At about the same time, Aki et al. (1977) worked out the 3D inversion method for velocity parameters using V_p delay time of teleseismic events. This method has led to a large number of applications, ranging from large continental areas to very local structures (Mitchell et al., 1977; Romanowicz, 1979; Taylor and Toksoz, 1979; Babuska et al., 1984; Yanovskaya, 1984; Maguire et al., 1985). For the global arrival time data, Dziewonski et al. (1977) used the ISC (http://www.isc.ac.uk/) data set to determine the spherical harmonic coefficients of velocity perturbations in the Earth's mantle.

The first tomographic results using iterative techniques on a global scale were presented by Clayton and Comer (1984), and some tentative studies of the reliability of the iterative solutions were published by Ivansson (1983) and Nolet (1984, 1985). Spakman (1986) used large-scale iterative techniques to resolve a very detailed velocity structure near the convergence of the African and Eurasian plate. Seismic tomography as defined by Clayton (1984) is not limited to imaging the Earth or part of the Earth using body-wave arrival time data; it has been extended to include surface waves and waveforms as well.

In this paper we study the depth range from the Moho discontinuity to about 250 km, from where the magmas originate and where body-wave tomography does not have optimal resolution (Gobarenko et al., 1990; Spakman, 1990; Babuska and Plomerova, 1990; Alessandrini et al., 1995, 1997; Papazachos et al., 1995; Papazachos and Kiratzi, 1996; Cimini and De Gori, 1997; Parolai et al., 1997; Piromallo and Morelli, 1997; Plomerova, 1997; Bijwaard et al., 1998; Lucente et al., 1999). Pioneering surface wave tomography maps for the Mediterranean have been produced by Pilant (1979) and Panza et al. (1980a). We will focus on the Italian area and surrounding regions where the large concentrations of volcanic complexes have been studied in detail and a wealth of surface wave data (Payo Subiza, 1967, 1969; Panza, 1980; Panza et al., 1980b, 1982; Calcagnile and Panza, 1981; Calcagnile et al., 1982; Snieder, 1988; Yanovskaya et al., 1998, 2000; Martinez et al., 1997, 2000, 2001; Ritzwoller and Levshin, 1998; Pasyanos et al., 2001; Karagianni et al., 2002; Pontevivo and Panza, 2002; Marquering and Snieder, 1996; Panza et al., 2003; Panza and Pontevivo, 2004; Venisti et al., 2005) is available to be used in the joint interpretation with petrological and geochemical data.

4. Surface wave tomography

Different methodologies for body-wave tomography are described in full detail in many textbooks and scientific compilations (e.g., Aki and Richards, 1980; Nolet, 1987; Iyer and Hirahara, 1993). In this section we will describe surface wave tomography, that uses many concepts common to body-wave tomography. The main difference between the two methods is that surface wave tomography, unlike body-wave tomography, does not require the assumption of an a priori reference model. Phase and/or group surface wave velocities, observed along different paths, are widely used to map local values of the velocities for a set of periods, monitoring the horizontal and vertical variations in the Earth's structure. While surface wave tomography is particularly suitable in oceanic and continent–ocean transition zones, such as the Tyrrhenian, body-wave tomography would require a deployment of Ocean Bottom Seismometers (OBS), not otherwise available, needed for the appropriate resolving power, through the measurement of travel times of almost vertical rays.

For phase velocity measurements the two-station method is frequently used, where one measures the phase difference $\delta\psi=\int\delta k\mathrm{d}s$ of the surface wave between two stations (Aki and Richards, 1980). Because of the relation between the wave-number perturbation and the phase velocity perturbation ($\delta k / k=-\delta c / c$), one effectively extracts, from the surface wave recordings, the integral of the phase velocity perturbation between stations or between a source and a receiver (Panza, 1976; Snieder, 1996):

$$\delta\psi = \int \delta k \mathrm{d}s = -\frac{\omega}{c^2}\int \delta c \mathrm{d}s. \tag{7}$$

The group velocity is most efficiently obtained performing a moving window analysis to the signal (Dziewonski and Hales, 1972; Levshin et al., 1972 and 1992). These measurements lead to a change δt, in the arrival time of a narrow-band wave packet with centre-frequency ω, that can be related to the average group velocity perturbation along the reference ray in the laterally homogeneous background model:

$$\delta t = \int \delta\left(\frac{1}{U}\right)\mathrm{d}s = -\frac{1}{U^2}\int \delta U \mathrm{d}s. \tag{8}$$

The obtained dispersion measurements are linear integrals of the local perturbations in the phase or group velocity (Eqs. (7) and (8)). The local velocity perturbation can be obtained by a tomographic inversion of the integrals (7) and (8). Several independently developed methods and computer codes for tomographic inversions of surface wave data on phase and group velocity are in use nowadays. In the following, the main concepts of the 2D seismic tomography based on time residuals, which are directly used to estimate lateral variations of surface wave velocities, are presented referring to Yanovskaya (2001).

For regional studies it is possible to use the method for the general inverse problem for the travel times with Cartesian coordinates (x, y) because a small part of a spherical surface is easily reduced to the case of a plane by the Mercator transformation of the coordinates and velocity (Yanovskaya, 1982; Yanovskaya et al., 1990; Yanovskaya and Ditmar, 1990). The general approach for solving the plane and the spherical problem is the same but the functions used to represent the solution are different in the two cases. The 3D problem in the domain (x, y, T) may be reduced to a 2D problem. If the given data are the phase and/or group velocities at different periods and along some paths, crossing the region under investigation, and if we want to determine a function which fits the data, the general two-dimensional tomography problem can be formulated in the framework of ray theory (Yanovskaya and Ditmar, 1990), i.e., to assume surface waves to travel along paths that are lines.

It is generally supposed that the source-station travel time is given by an integral over the ray. Accordingly, the time residual relative to some initial approximation is determined, in a linearized formulation, from the functional:

$$\delta t_i = -\int_{L_{0i}} \frac{\delta V(r)}{V_0^2(r)}\mathrm{d}s \tag{9}$$

where $V_0(r)$ is the velocity in the initial approximation; $\delta V(r)=V(r)-V_0(r)$; L_{0i} is the path corresponding to the initial approximation. The initial velocity is assumed to be a constant that is equal to the average velocity on a flat Earth at a given period in the area of study. In that case L_{0i} is a straight line[3] on a flat Earth (or the epicentre-station segment of the great circle for a sphere). Denoting $m(r)=-\delta V(r)/V_0$ and replacing (8) with the integral over the 2D area of study, Ω, one has:

$$\delta t_i = \iint_{\Omega} G_i(r) m(r) \mathrm{d}(r) \tag{10}$$

where $G_i(r)$ is a function that is singular on the i-th ray, vanishes outside it, and satisfies the condition:

$$\iint_{\Omega} G_i(r) m(r) \mathrm{d}(r) = t_{0i}$$

t_{0i} being the time of travel along the i-th ray in the initial approximation model. It is important to note that the travel time is given by the integral over some area that encloses the line and not over an infinitely thin line. The desired relative residual δt_i can be expressed in terms of Eq. (10) with a kernel, $\widetilde{G}_i(r)$, that is bounded and different from zero in some vicinity of the ray. Introducing, in Ω, the coordinates s, along the ray, and n, normal to the ray, and finding the region $N(s)$ along n where $\widetilde{G}(r)$ is different from zero, one can write the integral (9) in the form:

$$\begin{aligned}\delta t_i &= \int_{L_{0i}} \mathrm{d}s \int_{N(s)} \widetilde{G}_i(n,s) m(n,s) \mathrm{d}n \\ &= \int_{L_{0i}} \bar{m}_i(s)\frac{\mathrm{d}s}{V_0} = \iint_{\Omega} \bar{m}_i(r) G_i(r) \mathrm{d}r\end{aligned} \tag{11}$$

where $\bar{m}_i(r) = V_0 \int_{N_{(s)}} \widetilde{G}_i(n,s) m(n,s) \mathrm{d}n$ is not the local value of m at the point r, but it is an average along the direction which is perpendicular to the ray at that point.

[3] The validity of this assumption, in the cases shown in the next section, has been successfully tested numerically as suggested by Yanovskaya et al. (1998) by computing, for each assumed straight path, the curved path, consistent with the pattern of the phase velocity distribution, representative of the study region.

When the velocity varies smoothly[4] and its variation is not large, then the error incurred by using Eq. (11) instead of Eq. (9) will not be large either, and can be assumed to be random.

In that case the observations (time residuals δt_i) and the desired model will be related by:

$$\delta t_i = \iint_{\Omega} G_i(r) m(r) \mathrm{d}r + \varepsilon_i.$$

In the case in which the errors ε_i can be assumed independent, the search for the unknown function $m(r)$ will reduce to minimizing:

$$\sum_i \left(\delta t_i - \int\int_{\Omega} G_i(r) m(r) \mathrm{d}r\right)^2. \quad (12)$$

The solution of the problem is not unique and hence extra restrictions should be imposed on the desired function. The methods employed to construct the solution differ in relation to the restrictions imposed. The Backus–Gilbert method imposes a restriction on the behaviour of the desired functions: the solution must have the minimum norm (to minimize the integral of the squared derivative). In the 2D case, it means minimizing the integral of the squared gradient of $m(r)$. From Eq. (12), in order to find $m(r)$, α being a regularization parameter,[5] one has to minimize the functional:

$$\sum_i \left(\delta t_i - \int\int_{\Omega} G_i(r) m(r) \mathrm{d}r\right) + \alpha \iint_{\Omega} |\Delta m(r)|^2 \mathrm{d}r. \quad (13)$$

The minimization of Eq. (13) is still not sufficient to derive the unique solution, considering that the second term in Eq. (13) contains the gradient of the function rather than the function itself, so that one needs to have some conditions given at the edge of the region Ω.

The method for constructing the solution for a flat Earth, approximation that is valid when the region is smaller than 4000 km across, is provided by Ditmar and Yanovskaya (1987) and Yanovskaya and Ditmar (1990). They show that the minimization of Eq. (13) reduces to solving the Poisson equation:

$$\nabla^2 m(r) = \sum_i \lambda_i G_i(r) \quad (14)$$

The resolution is estimated at any point by the size of the averaging area, similarly to the Backus–Gilbert method, where the resolution is given by the length of the averaging interval (for more details see Appendix).

5. Inverse problem

The estimation of physical parameters of the Earth's material from the values observed in some part of the medium (usually the Earth surface) is the inverse problem of geophysics.

The determination of the density distribution from gravity anomalies is a linear problem and can be solved in a quite straightforward way (Moritz, 1995; Zhdanov, 2002), mainly when geometrical constraints can be derived from independent data, like, for instance, seismological ones (e.g., tomography). On the contrary, the determination of the shear wave velocity–depth curve from surface wave dispersion curves is a severely non-linear problem.

The first step of the inversion is the construction of surface wave tomography maps; the second is to perform the non-linear inversion of the dispersion curves extracted from tomographic maps, to obtain shear wave velocity (V_s) models of the crust and upper mantle. This can be done superimposing to the tomography maps a grid with mesh comparable to the resolving power of the data ($1° \times 1°$ in our case), thus covering with contiguous cells the study domain Ω. Each cell of the grid can be characterised by average dispersion curves computed as the average of the values read from the relevant tomography maps at the four knots of each $1° \times 1°$ cell.

5.1. The "Hedgehog" non-linear inversion method

In the trial-and-error Hedgehog method (Valyus, 1972; Valyus et al., 1969; Knopoff, 1972), that represents an optimized Monte Carlo search, the unknown structural Earth model is replaced by a set of parameters, therefore the retrieval of the model is reduced to the determination of the numerical values of the parameters. For each cross-section, the theoretical values are computed by comparison with real data and the discrepancy between the computed data and the observed ones is calculated. The set of cross-sections for which the discrepancy is sufficiently small is the solution of the problem. Therefore the problem is reduced to find the zone of minimum of a multidimensional function in the space of the unknown

[4] The lateral surface wave velocity variations are considered small enough, so that a starting model can be taken as laterally homogeneous and the ray paths in the starting model are straight lines or great circles. According to this assumption: $|m(r)| << 1$ the function m(r) is assumed to be smooth, to satisfy the condition $(\partial m/\partial n)_{C_\Omega}=0$ on the contour C_Ω of the area Ω (at infinity).

[5] The value of the regularisation parameter is chosen so that the allowed velocity range in the solution isn't less than the velocity range in the data set.

parameters of the cross-section (Panza, 1981) and it is independent from the starting solution.

It is possible to classify three kinds of parameters; *fixed* (the value is held constant during the inversion according to independent geophysical evidences), *independent* (the value is searched during the inversion), *dependent* (the value of this parameter is linked, through a formal relationship, to the independent parameter).

The number of independent parameters has to be small in order to interpret more easily the inversion results but not too small because the result, in this case, could be too rough and therefore some interesting features could be missed. Moreover for each independent parameter the a priori limits (i.e. the region in the model space in which the parameter value is searched) have to be specified, if available. In the elastic approximation, fully satisfactory for our purposes, the unknown Earth model is divided into a stack of homogeneous isotropic layers. Each layer is defined by a number of physical functions: shear wave velocity and thickness of the layers (independent parameters), compressional-wave velocity (dependent parameter) and density (fixed parameter). The range of variability of the independent parameters is fixed according to the available geophysical information and the parameterization is controlled by the resolving power of the data (Knopoff and Panza, 1977; Panza, 1981).

The seismic profiles (refraction and reflection) that cross the studied region as well as other geophysical information available from literature are used to fix the thickness and the compressional-wave velocities in the uppermost crustal layers. In general solids are assumed to be Poissonian and the density is estimated using the Nafe–Drake relation (e.g., Fowler, 1995; Ludwig et al., 1970). However other assumptions can be used, if more pertinent to the study area.

The multidimensional region, in the investigated model space, is thus divided into a M-dimensional grid (M equals the number of independent parameters). The function of parameters is calculated in every knot of the grid and finally the points in which the function is sufficiently small are chosen.

The criteria to choose one cross-section as solution of the inversion problem is the following: for each structural model selected in the model space, surface wave dispersion curves are calculated and the differences between the theoretical and the experimental dispersion curves are computed. If, at each period, this difference is less than the measurement errors and if the r.m.s. (root mean square) of the differences, at all periods considered, is less than a chosen quantity (usually 60–70% of the average of the measurement errors), the model is accepted (Panza, 1981).

Since the problem is not unique, i.e. the inversion is multi-valued, a set of equi-probable models are accepted. A good rule of thumb is that the number of solutions obtained, n, is comparable with the number of inverted parameters, M.

5.2. The resolving power

The choice of the parameters and of their steps, so that the latter can represent the parameters uncertainty, has to be related to the description of the data variances in the M-dimensional parameter space. Therefore the partial derivatives of the dispersion curves with respect to the considered parameter (Rodi et al., 1975; Urban et al., 1993) have to be calculated, for an average representative structure (e.g., continental, oceanic, rift), at all the periods of interest. The resolving power, which is quantified by the partial derivatives, controls the suitable steps that are used in the inversion, as follows.

Starting from a known geophysical structural model, the group ($U(T_i)$) and phase ($c(T_i)$) velocity dispersion curves are calculated for each selected period T_i where $i=1,\ldots, N$. The velocities are assumed to have standard deviations $\sigma_u(T_i)$ and $\sigma_c(T_i)$, respectively. A description of model variances corresponding to the data variances in the M-dimensional parameter space is particularly complex. To simplify the task it is possible to use the M diagonal elements of the model error matrix:

$$\left[\frac{1}{N}\cdot\sum_{i=1}^{N}\left(\frac{\partial c(T_i)}{\partial P_j}\right)^2\cdot\sigma(T_i)^{-2}\right]^{-\frac{1}{2}} \tag{15}$$

which are the intercepts of the solution ellipsoid with the parameter axes P_j.

If parameter P_j is allowed to vary by an amount δP_j from its starting value, while the others are held fixed at a starting value, then the r.m.s. difference between the exact result and the model result is:

$$\left[\sqrt{\frac{1}{N}\cdot\sum_{i=1}^{N}\left(\frac{\partial c(T_i)}{\partial P_j}\right)^2}\right]\cdot\delta P_j \tag{16}$$

which can be set equal to the pre-assigned value σ_c.

The quantities given by Eq. (15) are the standard deviations in the parameters P_j for the cases in which all the other parameters P_i ($i\neq j$) are kept fixed at their starting values. Thus, the tabulation of the items (15) gives some rough information regarding resolution of the parameters P_j by the data set, and the quantities (15) can be called the resolution, despite the fact that this

definition is inconsistent with other usage in the literature (Knopoff and Panza, 1977; Panza, 1981).

It follows that the proper use of the results given by Eq. (15) is their application as guiding criteria in the structure parameterization to be used with the Hedgehog inversion procedure.

In most typical uses of least square criteria, the addition of irrelevant data to a data set weakens the quality of a parametric fit. Therefore, considering the problem of searching for the most suitable data set for the determination of any given model parameter, if it is correct that the inclusion of too much data is deleterious to the problem of optimizing resolution, then the problem of finding the proper subset of data can be approached rejecting those data which make the largest contributions to the estimate of Eq. (15). The maximum resolution for a given model parameter P_j is achieved by retaining only the datum $c(T_i)$ that satisfy the condition

$$\mathrm{Min}\left(\frac{\partial c(T_i)}{\partial P_j}\right)^{-1} \cdot \sigma(T_i) \tag{17}$$

This criterion is valid only if all the parameters, except the selected datum, are held fixed and known during the exploration for the optimum value of the parameter. But, since none of the parameters is known, we must take into account the feature that the partial derivative curves often have large wings remote from the peaks (different parameters are correlated). When two parameters are not independent, the resolution of each is poorer than the values obtained by Eq. (17) and the full problem requires the determination of the period for which the quantities δP_j are minima subject to the condition:

$$\sum_j \left(\frac{\partial c(T_i)}{\partial P_j}\right) \cdot \delta P_j = \sigma(T_i) \tag{18}$$

In applying the Hedgehog inversion procedure, the parameterization for the inversion is defined so that the parameter steps are minima, subject to the condition (17). In this way each parameter step represents a satisfactory measure of the uncertainty affecting each parameter, since all the solutions of the Hedgehog inversion differ by no more than $\pm\delta P_j$ from each other.

5.3. The choice of the representative solution

The Hedgehog inversion produces an ensemble of acceptable models consistent with the dispersion data, but, in order to summarize and interpret the results, it is very useful to identify a representative model. There are two typical approaches: the first one consists in choosing the 'Median Model' of all the solutions (Shapiro and Ritzwoller, 2002) as the representative model; the second approach chooses the model characterised by the minimum r.m.s. Other approaches are inspired by William of Occam, who wrote "it is vain to do with more what can be done with fewer" (see Russell, 1946, ch.14). What has become known as Occam's razor has become fundamental in modern science, i.e. hypotheses should be neither unnecessarily complicated nor unnecessarily numerous. Taking into account the origin of the problem (surface waves tomography — an intrinsically smoothing technique), the developed criteria of optimization consist in finding, for each cell, the representative solution so that the lateral velocity gradient between neighbouring cells is minimized. One motivation for seeking smooth global models is that we want to avoid the introduction of heterogeneities that can possibly arise from a subjective choice. Starting from the search of the representative solution in one cell (called *starting cell*) we look for the representative solution in all the other cells of the studied domain Ω, following the criteria of maximum smoothness. The method is fast but it depends from the starting cell that can be chosen either by objective criteria or by adequate geophysical and geological information. Other methods of optimization, more independent from the single starting cell, have been developed based on dynamic programming method (e.g., Bryson et al., 1975) but will not be dealt with here.

6. Regional lithospheric models from geophysical data

The available surface waves dispersion curves at regional scale (Pontevivo and Panza, 2002; Pontevivo, 2003), determined by the two-stations method (Panza, 1976) or by the Frequency Time Analysis (Levshin et al., 1972, 1992), e.g., see Fig. 2a,b, have been used to obtain tomography maps, e.g., see Fig. 2a,b, using the two-dimensional tomography algorithm developed by Ditmar and Yanovskaya (1987) and Yanovskaya and Ditmar (1990). The database of the group velocity dispersion curves and tomography maps have recently been reviewed and improved (Raykova et al., 2004). The period range of the group velocity dispersion curves derived from the records collected at regional distances (300 km–4000 km) is between 7 and 80 s, while longer period group velocity data, collected from global studies (Ritzwoller and Levshin, 1998; Shapiro and Ritzwoller, 2002), have been used to extend the period range up to 150 s. Therefore the database is

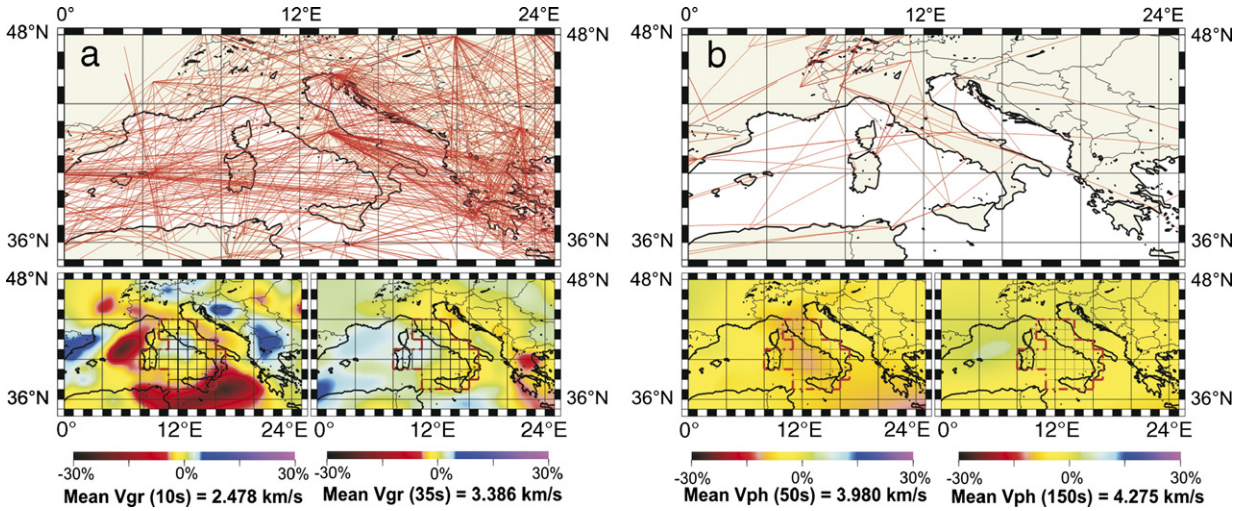

Fig. 2. Seismic paths used for surface wave tomography and examples of tomography maps: (a) group velocity, (b) phase velocity. (V_{gr}) after group velocity and (V_{ph}) after phase velocity.

suitable to explore the S-wave velocity structure down to a depth of about 300 km.

The lateral resolving power of the available dispersion data is of about 200 km (Pontevivo and Panza, 2002; Panza et al., 2004); however the availability of a priori independent geological and geophysical information, about the uppermost part of the crust, improves the lateral resolving power and justifies the choice to perform the non-linear inversion of dispersion curves averaged over cells of a $1°\times1°$ grid (Pontevivo, 2003, Panza et al., 2003) within the study area (Fig. 3) and even smaller, when appropriate a priori information is available (Chimera et al., 2003).

The updated cellular dispersion values, given in Table 2, have been inverted with Hedgehog and the explored parameter's space and the results of the inversion relevant for our purposes are summarized in Fig. 4.

The parameterization of the structure to be inverted has been chosen taking into account the resolving power of the data (Knopoff and Panza, 1977; Panza 1981) and relevant petrological information (e.g., Ringwood, 1966; Graham, 1970; Ahrens, 1973; Bottinga and Steinmetz, 1979; Della Vedova et al., 1991). In such a way we have fixed the upper limit of V_s, for the sub-Moho mantle, at 4.90 km/s, and the lower limit of V_s at 4.00 km/s for the asthenosphere at depths greater than about 60 km.

The available seismic profiles that cross most of the peninsula and adjacent seas together with other information available from literature have been used as a priori information to fix the thickness h and the compressional velocity V_p of the uppermost crustal layers, assuming that they are formed by Poissonian solids. The density of all the layers is in agreement with the Nafe–Drake relation, as reported by Ludwig et al. (1970). The structure below the inverted layers is the same for all the considered cells and it has been fixed accordingly with already published data (Du et al., 1998). In each cell the depth of the Mohorovicic discontinuity (M) and the selected solution (thick line) are indicated.

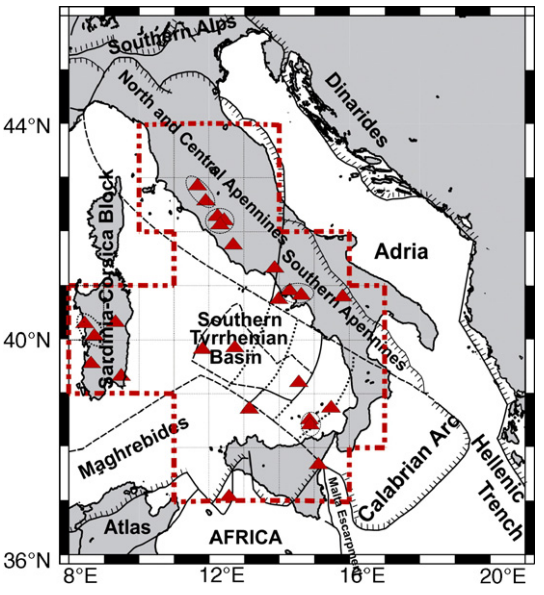

Fig. 3. The studied area subdivided in cells ($1°\times1°$), limited by the dotted lines, is superimposed to the structural and kinematic sketch of Italy and surrounding areas modified from Meletti et al. (2000). Red triangles represent the different recent and active volcanoes within the study area.

Table 2
Group (U) and phase (C) velocity values at different periods (from 7 s to 150 s and from 15 s to 150 s, respectively) with the single point error (ρ_g, ρ_{ph}) and the r.m.s. values for each cell. All phase velocities have been corrected for sphericity following Bolt and Dorman (1961). Group velocity data from 80 s and above are taken from the Centre for Imaging the Earth's Interior, Boulder University

	Cell c0 (10.5; 43.5)				Cell c1 (11.5; 43.5)				Cell c2 (12.5; 43.5)			
Period (s)	U (km/s)	ρ_g (km/s)	C (km/s)	ρ_{ph} (km/s)	U (km/s)	ρ_g (km/s)	C (km/s)	ρ_{ph} (km/s)	U (km/s)	ρ_g (km/s)	C (km/s)	ρ_{ph} (km/s)
7	2.000	0.155			2.055	0.155			2.150	0.155		
10	2.305	0.130			2.350	0.125			2.350	0.125		
15	2.610	0.115	3.110	0.200	2.525	0.110	3.095	0.200	2.480	0.105	3.075	0.200
20	2.870	0.115	3.430	0.150	2.750	0.110	3.400	0.150	2.660	0.105	3.380	0.150
25	3.060	0.115	3.545	0.110	2.950	0.110	3.530	0.110	2.860	0.105	3.540	0.110
30	3.210	0.110	3.615	0090	3.135	0.110	3.600	0.090	3.070	0.105	3.615	0.090
35	3.415	0.105	3.690	0.080	3.370	0.095	3.685	0.080	3.305	0.095	3.695	0.080
50	3.685	0.090	3.820	0.060	3.700	0.095	3.820	0.060	3.670	0.095	3.835	0.060
80	3.745	0.120	3.940	0.060	3.750	0.120	3.940	0.060	3.760	0.120	3.940	0.060
100	3.675	0.080	3.985	0.080	3.670	0.080	3.980	0.080	3.660	0.080	3.980	0.080
125	3.580	0.080			3.580	0.080	4.065	0.120	3.580	0.080	4.075	0.120
150	3.520	0.080	4.167	0.140	3.525	0.080	4.160	0.120	3.530	0.080	4.165	0.120
r.m.s.		0.071		0.077		0.069		0.070			0070	0.070

	Cell c3 (13.5; 43.5)				Cell b0 (11.5; 42.5)				Cell b1 (11.5; 42.5)			
Period (s)	U (km/s)	ρ_g (km/s)	C (km/s)	ρ_{ph} (km/s)	U (km/s)	ρ_g (km/s)	C (km/s)	ρ_{ph} (km/s)	U (km/s)	ρ_g (km/s)	C (km/s)	ρ_{ph} (km/s)
7	2.200	0.150										
10	2.315	0.125			2.440	0.130			2.527	0.135		
15	2.445	0.100			2.730	0.110			2.640	0.115		
20	2.585	0.100			3.070	0.105	3.470	0.150	2.965	0.115	3.419	0.150
25	2.780	0.100	3.566	0.110	3.300	0.105	3.550	0.110	3.210	0.115	3.558	0.110
30	3.010	0.100	3.649	0.090	3.440	0.105	3.600	0.090	3.395	0.115	3.595	0.090
35	3.210	0.100	3.726	0.080	3.580	0.100	3.685	0.080	3.535	0.110	3.684	0.080
50	3.635	0.100	3.859	0.060	3.715	0.100	3.825	0.060	3.720	0.100	3.824	0.060
80	3.765	0.120	3.946	0.060	3.730	0.120	3.930	0.060	3.740	0.120	3.935	0.060
100	3.655	0.080			3.660	0.080	3.985	0.080	3.660	0.080	3.983	0.080
125	3.580	0.080	4.078	0.120	3.560	0.080	4.060	0.120	3.565	0.080	4.064	0.120
150	3.540	0.080	4.172	0.120	3.500	0.080	4.165	0.120	3.505	0.080	4.160	0.120
r.m.s.		0.067		0.060		0.068		0.063		0.068		0.063

	Cell b2 (12.5; 42.5)				Cell b3 (13.5; 42.5)				Cell a1 (11.5; 41.5)			
Period (s)	U (km/s)	ρ_g (km/s)	C (km/s)	ρ_{ph} (km/s)	U (km/s)	ρ_g (km/s)	C (km/s)	ρ_{ph} (km/s)	U (km/s)	ρ_g (km/s)	C (km/s)	ρ_{ph} (km/s)
7	2.270	0.170			2.270	0.165						
10	2.600	0.155			2.440	0.165			2.670	0.125		
15	2.595	0.125	3.055	0.200	2.540	0.125	3.035	0.200	2.820	0.115		
20	2.860	0.125	3.370	0.150	2.735	0.125	3.340	0.150	3.170	0.105		
25	3.080	0.125	3.560	0.110	2.915	0.115	3.550	0.110	3.420	0.100	3.590	0.110
30	3.310	0.120	3.600	0.090	3.175	0.115	3.625	0.090	3.560	0.100	3.610	0.090
35	3.445	0.115	3.685	0.080	3.300	0.110	3.700	0.080	3.655	0.100	3.690	0.080
50	3.685	0.095	3.835	0.060	3.655	0.095	3.855	0.060	3.740	0.100	3.825	0.060
80	3.760	0.120	3.945	0.060	3.765	0.120	3.950	0.060	3.730	0.120	3.930	0.060
100	3.665	0.080	3.980	0.080	3.670	0.080	3.985	0.080	3.655	0.080	3.985	0.160
125	3.575	0.080	4.070	0.240	3.590	0.080	4.075	0.120	3.560	0.080	4.065	0.240
150	3.515	0.080	4.160	0.240	3.530	0.080	4.165	0.120	3.500	0.080	4.160	0.240
r.m.s.		0.075		0.085		0.078		0.070		0.066		0.085

(continued on next page)

Table 2 (*continued*)

Period (s)	Cell a2 (12.5; 41.5)				Cell a3 (13.5; 41.5)				Cell a4 (14.5; 41.5)			
	U (km/s)	ρ_g (km/s)	C (km/s)	ρ_{ph} (km/s)	U (km/s)	ρ_g (km/s)	C (km/s)	ρ_{ph} (km/s)	U (km/s)	ρ_g (km/s)	C (km/s)	ρ_{ph} (km/s)
7					2.470	0.170			2.390	0.160		
10	2.740	0.120			2.620	0.150			2.370	0.135		
15	2.800	0.110			2.735	0.115			2.605	0.110	3.000	0.200
20	3.110	0.105			.2.990	0.115			2.830	0.105	3.300	0.150
25	3.300	0.105	3.590	0.100	3.120	0.115	3.575	0.110	2.970	0.105	3.540	0.110
30	3.470	0.095	3.625	0.090	3.320	0.105	3.645	0.090	3.220	0.095	3.650	0.090
35	3.565	0.095	3.695	0.080	3.400	0.105	3.710	0.080	3.280	0.095	3.720	0.080
50	3.710	0.095	3.825	0.060	3.680	0.090	3.840	0.060	3.660	0.095	3.860	0.060
80	3.745	0.120	3.940	0.060	3.760	0.120	3.940	0.060	3.760	0.120	3.945	0.060
100	3.670	0.080			3.680	0.080	3.985	0.160	3.700	0.080	3.985	0.080
125	3.580	0.080			3.600	0.080	4.070	0.240	3.620	0.080	4.065	0.120
150	3.515	0.080			3.530	0.080	4.160	0.240	3.560	0.080	4.150	0.120
r.m.s.		0.066		0.052		0.072		0.085		0.068		0.070

Period (s)	Cell a5 (15.5; 41.5)				Cell A-2 (8.5; 40.5)				Cell A-1 (9.5; 40.5)			
	U (km/s)	ρ_g (km/s)	C (km/s)	ρ_{ph} (km/s)	U (km/s)	ρ_g (km/s)	C (km/s)	ρ_{ph} (km/s)	U (km/s)	ρ_g (km/s)	C (km/s)	ρ_{ph} (km/s)
7												
10	2.255	0.125			2.290	0.130			2.460	0.130		
15	2.470	0.105	3.000	0.200	2.960	0.120			3.005	0.110		
20	2.700	0.100	3.305	0.150	3.360	0.100			3.350	0.100		
25	2.905	0.100	3.515	0.110	3.600	0.100	3.680	0.220	3.585	0.100		
30	3.210	0.100	3.655	0.090	3.640	0.090	3.660	0.090	3.635	0.090		
35	3.295	0.100	3.725	0.080	3.690	0.090	3.740	0.080	3.700	0.090	3.725	0.220
50	3.650	0.100	3.875	0.060	3.710	0.090	3.860	0.060	3.720	0.090	3.650	0.180
80	3.750	0.120	3.945	0.060	3.670	0.130	3.935	0.060	3.680	0.130	3.650	0.160
100	3.710	0.081	3.985	0.080	3.600	0.080			3.615	0.080		
125	3.640	0.080	4.065	0.120	3.550	0.080			3.550	0.080		
150	3580	0.080	4.150	0.120	3.490	0.080			3.485	0.080		
r.m.s.		0.064		0.070		0.064		0.067		0.068		0.130

Period (s)	Cell A0 (10.5; 40.5)				Cell A1 (11.5; 40.5)				Cell A2 (12.5; 40.5)			
	U (km/s)	ρ_g (km/s)	C (km/s)	ρ_{ph} (km/s)	U (km/s)	ρ_g (km/s)	C (km/s)	ρ_{ph} (km/s)	U (km/s)	ρ_g (km/s)	C (km/s)	ρ_{ph} (km/s)
7												
10	2.550	0.130			2.580	0.135			2.650	0.130		
15	2.985	0.110			2.910	0.105			2.865	0.105		
20	3.315	0.090			3.235	0.095			3.165	0.095		
25	3.560	0.090	3.635	0.220	3.475	0.095	3.630	0.110	3.370	0.095	3.620	0.120
30	3.615	0.090	3.650	0.180	3.545	0.095	3.660	0.090	3.440	0.095	3.665	0.060
35	3.690	0.090	3.720	0.160	3.640	0.095	3.715	0.080	3.535	0.095	3.715	0.080
50	3.710	0.090	3.830	0.120	3.695	0.095	3.820	0.060	3.660	0.095	3.815	0.090
80	3.705	0.130	3.920	0.120	3.720	0.120	3.920	0.060	3.740	0.120	3.920	0.110
100	3.635	0.080			3.650	0.080			3.675	0.080		
125	3.560	0.080			3.575	0.080			3.600	0.080		
150	3.500	0.080			3.515	0.080			3.535	0.080		
r.m.s.		0.058		0.096		0.064		0.052		0.065		0.060

Table 2 (*continued*)

Period (s)	Cell A3 (13.5; 40.5)				Cell A4 (14.5; 40.5)				Cell A5 (15.5; 40.5)			
	U (km/s)	ρ_g (km/s)	C (km/s)	ρ_{ph} (km/s)	U (km/s)	ρ_g (km/s)	C (km/s)	ρ_{ph} (km/s)	U (km/s)	ρ_g (km/s)	C (km/s)	ρ_{ph} (km/s)
7									2.320	0.155		
10	2.580	0.140			2.380	0.130			2.280	0.125		
15	2.70	0.110			2.615	0.110			2.445	0.110		
20	3.070	0.100			2.910	0.105			2.760	0.100		
25	3.245	0.100	3.610	0.120	3.080	0.105	3.575	0.060	2.915	0.100		
30	3.355	0.100	3.680	0.060	3.260	0.095	3.680	0.060	3.170	0.095		
35	3.420	0.100	3.730	0.080	3.310	0.095	3.740	0.080	3.260	0.095		
50	3.630	0.100	3.680	0.090	3.610	0.095	3.840	0.090	3.600	0.095	3.855	0.240
80	3.750	0.120	3.610	0.110	3.760	0.130	3.930	0.110	3.760	0.120	3.930	0.240
100	3.695	0.080			3.710	0.080			3.730	0.080	3.985	0.160
125	3.620	0.080			3.640	0.080			3.665	0.080	4.060	0.060
150	3.555	0.080			3.580	0.080			3.600	0.080	4.145	0.060
r.m.s.		0.065		0.060		0.066		0.052		0.067		0.099

Period (s)	Cell A6 (16.5; 40.5)				Cell B-2 (8.5 ; 39.5)				Cell B-1 (9.5 ; 39.5)			
	U (km/s)	ρ_g (km/s)	C (km/s)	ρ_{ph} (km/s)	U (km/s)	ρ_g (km/s)	C (km/s)	ρ_{ph} (km/s)	U (km/s)	ρ_g (km/s)	C (km/s)	ρ_{ph} (km/s)
7	2.245	0.160										
10	2.255	0.125			2.290	0.130			2.360	0.130		
15	2.320	0.105	2.980	0.400	3.150	0.110			3.105	0.110		
20	2.615	0.100	3.295	0.300	3.450	0.100			3.370	0.110		
25	2.770	0.100	3.500	0.220	3.605	0.100			3.550	0.110		
30	3.100	0.100	3.670	0.180	3.634	0.100	3.710	0.090	3.600	0.100		
35	3.270	0.100	3.740	0.160	3.640	0.100	3.770	0.080	3.620	0.100		
50	3.595	0.100	3.865	0.060	3.675	0.100	3.860	0.060	3.665	0.100		
80	3.760	0.120	3.930	0.060	3.660	0.130			3.670	0.130		
100	3.755	0.080	3.980	0.160	3.595	0.080			3.610	0.080		
125	3.690	0.080	4.055	0.240	3.555	0.080			3.550	0.080		
150	3.625	0.080	4.140	0.240	3.505	0.080			3.500	0.080		
r.m.s.		0.067		0.131		0.066		0.054		0.067		0.000

Period (s)	Cell B0 (10.5; 39.5)				Cell B1 (11.5; 39.5)				Cell B2 (12.5; 39.5)			
	U (km/s)	ρ_g (km/s)	C (km/s)	ρ_{ph} (km/s)	U (km/s)	ρ_g (km/s)	C (km/s)	ρ_{ph} (km/s)	U (km/s)	ρ_g (km/s)	C (km/s)	ρ_{ph} (km/s)
7												
10	2.370	0.130			2.410	0.130			2.470	0.135		
15	2.965	0.110			2.840	0.110			2.800	0.105		
20	3.265	0.100			3.150	0.100			3.060	0.100		
25	3.485	0.100			3.380	0.100	3.670	0.220	3.290	0.100	3.650	0.060
30	3.550	0.100			3.455	0.100	3.710	0.100	3.370	0.100	3.705	0.060
35	3.600	0.100			3.520	0.100	3.750	0.160	3.425	0.100	3.745	0.080
50	3.650	0.100			3.160	0.095	3.825	0.120	3.570	0.095	3.810	0.090
80	3.650	0.120			3.670	0.120	3.910	0.120	3.735	0.120	3.910	0.110
100	3.630	0.080			3.650	0.080			3.675	0.080		
125	3.570	0.080			3.590	0.080			3.610	0.080		
150	3.515	0.080			3.530	0.080			3.555	0.080		
r.m.s.		0.065		0.000		0.063		0.104		0.065		0.052

(continued on next page)

Table 2 (*continued*)

Period (s)	Cell B3 (13.5; 39.5)				Cell B4 (14.5; 39.5)				Cell B5 (15.5; 39.5)			
	U (km/s)	ρ_g (km/s)	C (km/s)	ρ_{ph} (km/s)	U (km/s)	ρ_g (km/s)	C (km/s)	ρ_{ph} (km/s)	U (km/s)	ρ_g (km/s)	C (km/s)	ρ_{ph} (km/s)
7												
10	2.430	0.135			2.330	0.125			2.235	0.125		
15	2.720	0.110			2.550	0.115			2.355	0.120		
20	2.980	0.100			2.870	0.110			2.745	0.110		
25	3.195	0.100	3.630	0.110	3.040	0.110			2.825	0.110		
30	3.320	0.095	3.700	0.090	3.245	0.095			3.095	0.110		
35	3.370	0.095	3.745	0.080	3.310	0.095			3.225	0.100		
50	3.540	0.095	3.820	0.060	3.525	0.095	3.835	0.060	3.520	0.100	3.840	0.060
80	3.750	0.120	3.915	0.120	3.755	0.120	3.915	0.060	3.760	0.120	3.920	0.060
100	3.700	0.080			3.730	0.080			3.750	0.080		
125	3.640	0.080			3.665	0.080			3.690	0.080		
150	3.580	0.080			3.600	0.080			3.620	0.080		
r.m.s.		0.065		0.060		0.066		0.039		0.067		0.039

Period (s)	Cell B6 (16.5; 39.5)				Cell C1 (11.5; 38.5)				Cell C2 (12.5; 38.5)			
	U (km/s)	ρ_g (km/s)	C (km/s)	ρ_{ph} (km/s)	U (km/s)	ρ_g (km/s)	C (km/s)	ρ_{ph} (km/s)	U (km/s)	ρ_g (km/s)	C (km/s)	ρ_{ph} (km/s)
7	2.160	0.305										
10	2.190	0.125			2.310	0.125			2.325	0.125		
15	2.235	0.105			2.800	0.105			2.735	0.105		
20	2.590	0.100			2.995	0.105			2.920	0.100		
25	2.660	0.100			3.250	0.100	3.710	0.060	3.185	0.100	3.690	0.060
30	2.995	0.095			3.360	0.100	3.750	0.080	3.310	0.100	3.750	0.060
35	3.170	0.095			3.400	0.100	3.785	0.090	3.350	0.100	3.780	0.080
50	3.540	0.095			3.590	0.100	3.710	0.110	3.550	0.100	3.830	0.090
80	3.770	0.120			3.680	0.120			3.700	0.120	3.910	0.110
100	3.780	0.080			3.655	0.080			3.6780	0.080		
125	3.720	0.080	4.050	0.240	3.610	0.080			3.630	0.080		
150	3.650	0.080	4.131	0.240	3.560	0.080			3.580	0.080		
r.m.s.		0.075		0.156		0.063		0.056		0.065		0.052

Period (s)	Cell C3 (13.5; 38.5)				Cell C4 (14.5; 38.5)				Cell C5 (15.5; 38.5)			
	U (km/s)	ρ_g (km/s)	C (km/s)	ρ_{ph} (km/s)	U (km/s)	ρ_g (km/s)	C (km/s)	ρ_{ph} (km/s)	U (km/s)	ρ_g (km/s)	C (km/s)	ρ_{ph} (km/s)
7												
10	2.310	0.125			2.240	0.130			2.180	0.125		
15	2.610	0.115			2.430	0.120			2.240	0.115		
20	2.840	0.100			2.740	0.110			2.645	0.100		
25	3.080	0.100	3.660	0.060	2.905	0.110			2.720	0.100		
30	3.270	0.095	3.730	0.060	3.170	0.100			3.045	0.100		
35	3.320	0.095	3.770	0.080	3.260	0.100			3.190	0.100		
50	3.520	0.095	3.825	0.090	3.500	0.100	3.835	0.060	3.500	0.100		
80	3.720	0.120	3.910	0.100	3.735	0.120	3.910	0.060	3.760	0.120		
100	3.705	0.080			3.730	0.080			3.760	0.080		
125	3.650	0.080			3.680	0.080			3.710	0.080		
150	3.600	0.080			3.620	0.080			3.640	0.080		
r.m.s.		0.064		0.052		0.066		0.039		0.065		0.000

Table 2 (*continued*)

Period (s)	Cell C6 (16.5; 38.5)				Cell D1 (11.5; 37.5)				Cell D2 (12.5; 37.5)			
	U (km/s)	ρ_g (km/s)	C (km/s)	ρ_{ph} (km/s)	U (km/s)	ρ_g (km/s)	C (km/s)	ρ_{ph} (km/s)	U (km/s)	ρ_g (km/s)	C (km/s)	ρ_{ph} (km/s)
7												
10	2.165	0.120			2.221	0.125						
15	2.152	0.105			2.684	0.120			2.596	0.120		
20	2.556	0.095			2.803	0.105			2.765	0.100		
25	2.627	0.095			3.118	0.100	3.738	0.110	3.086	0.095	3.695	0.110
30	2.976	0.095			3.332	0.100	3.782	0.090	3.307	0.095	3.762	0.090
35	3.189	0.095			3.417	0.100	3.809	0.080	3.387	0.095	3.799	0.080
50	3.537	0.096			3.620	0.100	3.854	0.060	3.595	0.095	3.849	0.060
80	3.780	0.120			3.695	0.120			3.715	0.120		
100	3.785	0.080			3.665	0.080			3.682	0.080		
125	3.742	0.080			3.640	0.080			3.652	0.080		
150	3.667	0.080			3.592	0.080			3.607	0.080		
r.m.s.		0.076		0.000		0.065		0.055		0.065		0.055

Period (s)	Cell D3 (13.5; 37.5)				Cell D4 (14.5; 37.5)				Cell D5 (15.5; 37.5)			
	U (km/s)	ρ_g (km/s)	C (km/s)	ρ_{ph} (km/s)	U (km/s)	ρ_g (km/s)	C (km/s)	ρ_{ph} (km/s)	U (km/s)	ρ_g (km/s)	C (km/s)	ρ_{ph} (km/s)
7												
10	2.198	0.125			2.133				2.290	0.150		
15	2.457	0.120			2.286				2.150	0.115		
20	2.721	0.100			2.694				2.685	0.115		
25	3.001	0.100			2.891				2.835	0.115		
30	3.257	0.095			3.196				3.173	0.110		
35	3.347	0.095			3.294				3.292	0.105		
50	3.575	0.095			3.555				3.569	0.095		
80	3.732	0.120			3.751				3.766	0.120		
100	3.705	0.80			3.730				3.755	0.80		
125	3.670	0.080			3.692				3.720	0.080		
150	3.622	0.080			3.640				3.660	0.080		
r.m.s.		0.065		0.000		0.064		0.000		0.069		0.000

All the solutions for each cell are processed with an optimized smoothing method with the aim to define a smooth 3D model of the lithosphere–asthenosphere system, in agreement with the concept of Occam's razor (deGroot-Hedlin and Constable, 1990). In fact, the criteria of optimization used choose, for each cell, as representative solution the one that minimizes the local lateral velocity gradient.

The cellular velocity models represent, on one hand, robust average models with uncertainties consistent with the resolving power and on the other hand they do not allow the construction of suggestive smooth cross-sections and therefore deliberately enhancing the non-uniqueness of the inverse problem.

6.1. The lithosphere–asthenosphere system under the active and recent volcanic complexes

In the description that follows we will refer to the models reported in Fig. 5 as thick red lines, and to their ranges of variability, as given in Table 3. In Fig. 6 the synoptic representation of the chosen models for the cells containing the recent and active volcanoes is given down to 350 km with blow-ups of the first 100 km and 40 km depth. Panza et al. (2003) and Panza and Pontevivo (2005) have shown that an anomalous low-velocity zone, just below the Moho, with V_S, in general less than 4.20 km/s, is observed not only at the Central Tyrrhenian Sea backarc volcanoes and Ischia, but also at Amiata–Vulsini, Roccamonfina, Phlegraean Fields–Vesuvius (Guidarelli et al., 2002; Natale et al., 2005), Ustica, Vulture, Vulcano–Lipari and Stromboli. In the following, the term "mantle wedge" will be used to indicate this low-velocity zone in the uppermost mantle overlying a lid with V_S greater than about 4.35 km/s. Thus, in the mantle wedge the percentage of partial melting is greater than 1%, according to Bottinga and Steinmetz (1979) models. Furthermore, Panza et al. (2003) and Panza and Pontevivo (2004) have pointed out that, in the Tyrrhenian Sea area V_S values, that are usually observed only in crustal layers (V_S<4.0 km/s), can be

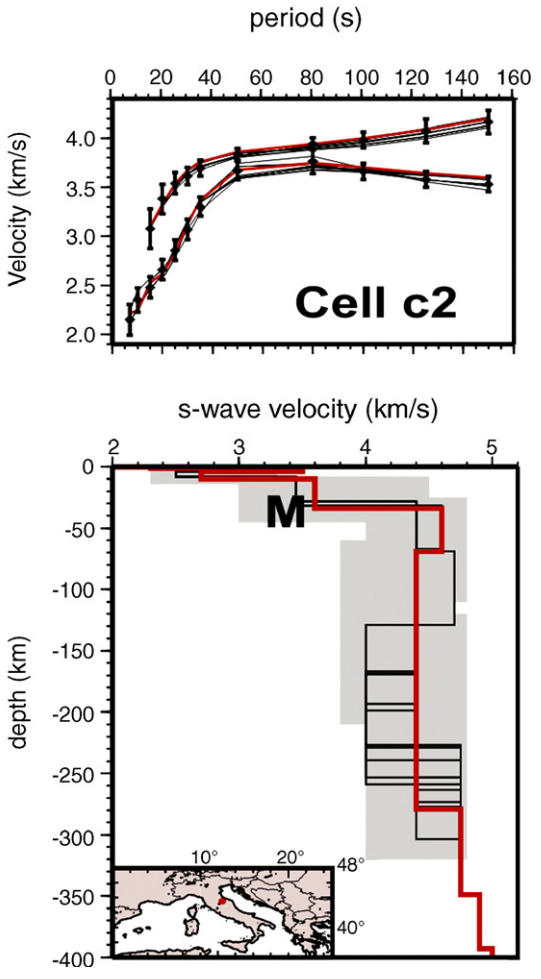

Fig. 4. Example of the averaged observed (black) dispersion measurements (vertical bars represent measurement errors), compared with the group and phase velocity values (red) computed for the accepted S-wave solution (solid bold red line) among other possible solutions (solid black lines). The grey area delimits the portion of the solution's space, sampled by the simultaneous non-linear inversion of phase and group velocity of Rayleigh waves.

interpreted as mantle material with a relatively high percentage of partial melting. This fact makes difficult the seismological definition of the nature of the crust and the identification of the crust–mantle transition. A clear example is seen beneath the area from Stromboli, Messina strait to Southern Calabria (cell C5), where a layer with V_s in the range 3.80–4.00 km/s and reaching a depth of about 44 km, is detected above high-velocity mantle material. An analysis of the seismicity in cell C5 leads two distinct interpretations for this layer (two-faced "Janus"). If we plot the hypocentres at sea, the layer is totally aseismic and therefore it can be reasonably assigned to a soft and possibly dehydrated mantle. Accordingly it may represent the deeper magma reservoir for Stromboli (Frezzotti et al., 2003), just below a ~17-km-thick crust. On the other side, if all events in cell C5 are considered, the "Janus" layer is occupied only by hypocentres of events located either in Sicily and Calabria (continental area) or close to their shoreline (as shown in Fig. 7). In such a case the layer can be reasonably assigned to the brittle continental crust. Similarly, if we analyse the structure under Albani (cell a2), the layer with V_s around 3.90 km/s can be assigned to the crust only till a depth of about 25 km, where the recorded seismicity stops. This layer is on top of a ~20-km-thick high-velocity lid, both layers being present in almost all of the retrieved solutions. The shut-down of the distribution of seismicity vs. depth within the cell, as shown in Fig. 8, at a depth of about 25 km, leaves room for an about 12-km-thick aseismic mantle layer. Therefore, the 3.90 km/s layer can be interpreted as a high-velocity lower crust, till a depth of about 25 km, above a very low-velocity soft mantle. Thus the Moho depth can be located around 25 km, as indicated by seismic refraction data (e.g., Nicolich and Dal Piaz, 1990). In this cell the asthenosphere, about 60 km thick and with V_s around 4.10 km/s, is recognizable at a depth of about 60 km and overlies a mantle material with average V_s of about 4.40 km/s. The cell a3 exhibits a negative velocity gradient within its 20-km-thick crust that overlies a low-velocity uppermost mantle layer with V_s of about 4.20 km/s and a thickness of about 30 km. Below this layer V_s increases with depth, to an average of 4.35 km/s.

To the north, in cell b1 a ~23-km-thick crust, whose lower part exhibits a ~16-km-thick layer with V_s of about 3.45 km/s, overlies a ~17 km thick low-velocity layer (V_s of about 4.20 km/s) within the uppermost mantle. Cell b2 exhibits a thicker crust, of about 33 km, with V_s of about 3.35 km/s and 3.75 km/s for its upper and lower part, respectively. Going from b1 to b2, the crust–mantle transition encompasses a crust overlying a soft uppermost mantle to a lower crust over a somehow faster mantle material. Below a depth of about 40 km both cells, b1 and b2, show similar physical characteristics: the V_s can be around 4.30 km/s till a depth of about 280 km, even though we can not exclude a gentle increment of the velocity vs. depth.

To the south-east, in A5 a ~20-km-thick crust is above a relatively low-velocity ~50-km-thick uppermost mantle layer with V_s of about 4.25 km/s. It overlies a 30-km-thick high-velocity lid with V_s as high as 4.80 km/s. Cells A4 and A5 are similar in their crust–uppermost mantle geometry and physical properties, however a main difference stands in the ~30-km-thick lid observed at a depth of about 70 km in cell A5 and absent in cell A4. To the West, in the nearby cell A3 (Ischia), the crust–mantle

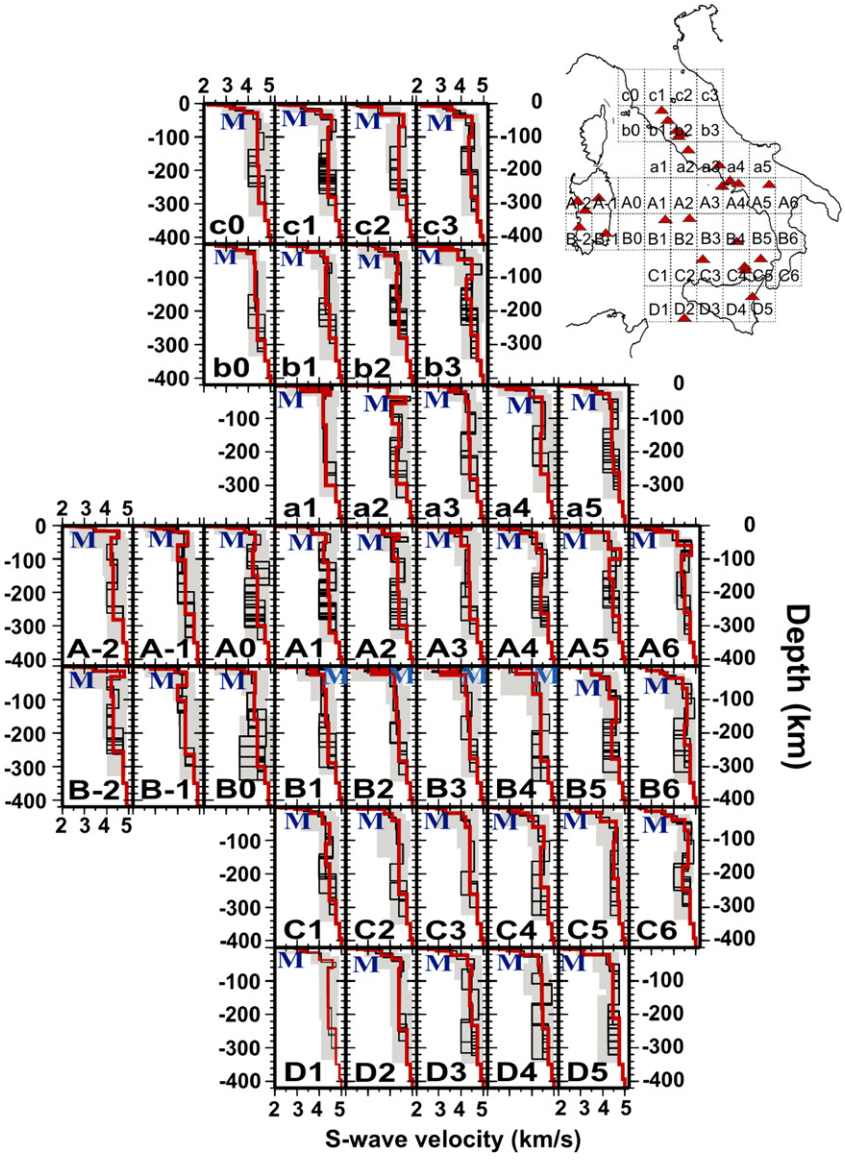

Fig. 5. The set of solutions (thin lines) for each cell (inset for location) obtained through the non-linear inversion of the dispersion relations are shown. The investigated parameter's space (grey zone) and the chosen solution (bold line) are shown as well (see Table 3).

transition is rather complex and seems to be consistent with a lithospheric doubling where the deeper Moho is at about 20 km and sits on soft mantle, or with the presence of a shallow layer of consolidated magma reservoir. Alternatively the crust–mantle transition can be very shallow, with a ~7-km-thick crust overlying a ~5-km-thick mantle layer, with V_s around 4.40 km/s, sitting on a ~10-km-thick very low-velocity mantle, with V_s around 3.50 km/s or a thin continental crust is intruded by a 5-km-thick layer of consolidated magma. The former interpretation turns out to be consistent with long-wavelength Bouguer anomaly modelling. More to the south a similar crust–uppermost mantle geometry can be observed in cells B1, B2 and B4, but with different physical parameters. In fact, the uppermost mantle layer in cell A3 has a V_s around 4.40 km/s, while in the cells B1–B2–B4 V_s varies in the range 3.15–4.05 km/s. This layering is consistent with standard schematic oceanic crustal models (e.g., Panza, 1984).

To the south, in cell C4, the ~19-km-thick crust overlies a ~12-km-thick very low-velocity mantle layer with V_s around 3.85 km/s. This layer overlies a relatively faster mantle layer with V_s of about 4.05 km/s, which sits on a ~60-km-thick lid with V_s of about 4.55 km/s.

Table 3
Range variability of the parameters h (thickness) and Vs for each layer of the chosen solution. In the table the inverted quantities are rounded off to 0.5 km or to 0.05 km/s and we take into account the a priori information used to constrain the inversion, therefore the chosen solution does not necessarily fall in the centre of the range that can be smaller than the step used in the inversion. In most of the cells of the study area, one and the same relation between Vs, Vp has been used for all the dependent parameters in the inversion $\left(V_p/V_s = \sqrt{3}\right)$. In the cells marked by * the value of $\left(V_p/V_s = 2.0\right)$ has been used, in agreement with the geophysical, geochemical and petrological model of the submarine lithosphere proposed by Bottinga and Steinmetz (1979).

The thickness marked by *** is not a truly inverted parameter, but it satisfies the condition that the total thickness from the free surface to the top of the fixed upper mantle is equal to a predefined quantity H. In this study $H = 349$ km. The structure deeper than H is the same for all the considered cells and it has been fixed accordingly with already published models (Du et al., 1998)

Cell c0 (10.5; 43.5)		Cell c1 (11.5;43.5)		Cell c2 (12.5;43.5)		Cell c3 (13.5;43.5)		Cell b0 (10.5; 42.5)	
V_s (km/s)	h (km)	V_s (km/s)	h (km)	V_s (km/s)	h (km)	V_s (km/s)	h (km)	V_s (km/s)	h (km)
–	–	–	–	–	–	–	–	0.00	0.5
2.20	4.0	2.20	4.0	1.60	0.5	1.55	1.1	3.00	0.5
2.65	1.0	2.65	1.0	2.30	1.0	2.08	2.4	2.65	6.0
3.00	1.5	3.20	2.0	3.00	1.0	3.18	1.5	–	–
–	–	–	–	3.50	1.5	3.50	1.0	–	–
3.10–3.30	7.5–11	3.25–3.45	11.5–17.5	2.60–2.80	5–7	3.25–3.40	10–13	3.35–3.55	8.5–14
3.60–4.00	13.5–20	3.95–4.25	18–23	3.55–3.65	22–25.5	3.50–3.80	16.5–23.5	3.65–4.25	7.5–9.5
4.35–4.45	45–60	4.45–4.65	35–50	4.50–4.70	35–50	4.35–4.65	45–60	4.20–4.30	30–45
4.25–4.55	75–100	4.25–4.55	85–105	4.25–4.55	80–100	4.25–4.45	90–110	4.25–4.35	90–110
4.25–4.65	85–110	4.20–4.60	75–100	4.20–4.60	85–110	4.25–4.65	70–90	4.20–4.60	90–120
4.75	***	4.75	***	4.75	***	4.75	***	4.75	***
4.90	44	4.90	44	4.90	44	4.90	44	4.90	44

Cell b1 (11.5; 42.5)		Cell b2 (12.5;42.5)		Cell b3 (13.5;42.5)		Cell a1 (11.5;41.5)		Cell a2 (12.5; 41.5)	
V_s (km/s)	h (km)	V_s (km/s)	h (km)	V_s (km/s)	h (km)	V_s (km/s)	h (km)	V_s (km/s)	h (km)
–	–	–	–	–	–	0.00	1.0	0.00	0.4
3.00	0.25	1.60	1.2	1.55	1.2	1.33	2.5	1.32	2.1
3.50	0.75	2.30	0.8	2.13	0.8	2.90	1.1	3.06	1.0
2.65	6.0	3.00	1.5	3.10	1.5	3.30	1.9	3.30	3.2
–	–	3.30	1.0	3.61	1.0	–	–	–	–
3.35–3.55	14–18	3.25–3.45	7.5–12.5	3.00–3.10	9–11.5	4.30–4.50	7.5–9	3.85–3.95	30–32
4.15–4.25	17.5–25.5	3.60–3.90	16.5–21.5	3.70–4.00	21–35	3.00–3.30	5.5–7.0	4.60–4.80	15.5–21.5
4.25–4.45	30–45	4.25–4.45	42.5–55	4.30–4.70	45–60	4.40–4.60	10–15	4.05–4.15	50–60
4.25–4.35	85–110	4.20–4.40	70–90	4.15–4.35	60–85	4.10–4.20	70–90	4.35–4.45	70–90
4.25–4.65	75–100	4.20–4.60	95–120	4.25–4.65	85–110	4.25–4.35	160–180	4.15–4.45	90–110
4.75	***	4.75	***	4.75	***	4.75	***	4.75	***
4.90	44	4.90	44	4.90	44	4.90	44	4.90	44

Cell a3 (13.5; 41.5)		Cell a4 (14.5; 41.5)		Cell a5 (15.5; 41.5)		Cell A-2 (8.5; 40.5)		Cell A-1 (9.5; 40.5)	
V_s (km/s)	h (km)	V_s (km/s)	h (km)	V_s (km/s)	h (km)	V_s (km/s)	h (km)	V_s (km/s)	h (km)
–	–	–	–	–	–	–	–	–	–
1.87	2.5	2.25	2.45	2.00	3.00	1.85	2.00	1.85	1.5
2.19	1.1	2.45	2.05	2.28	2.00	2.66	1.00	2.78	1.5
3.26	1.4	2.55	0.5	3.00	3.00	2.89	0.80	2.89	0.5
–	–	3.06	1.5	3.25	2.00	3.35	0.70	3.35	1.5
3.75–3.95	6–9	3.65–4.05	2–3	3.60–3.80	12.5–21	3.45–3.55	12–12.5	2.90–3.20	4–6
3.35–3.55	10–13	2.65–3.05	5–7.5	4.15–4.45	25–35	4.50–4.60	20–30	3.65–3.95	10–12.5
4.15–4.25	30–45	3.80–4.00	18.5–29.5	4.25–4.55	45–60	4.10–4.30	62.5–80	4.35–4.55	40–55
4.20–4.50	85–110	4.35–4.55	90–110	4.20–4.60	80–100	4.20–4.40	37.5–72.5	4.00–4.10	45.62.5
4.20–4.60	95–120	4.25–4.65	100–120	4.25–4.75	50–75	4.15–4.45	90–110	4.15–4.55	125–160
4.75	***	4.75	***	4.75	***	4.75	***	4.75	***
4.90	44	4.90	44	4.90	44	4.90	44	4.90	44

Table 3 (*continued*)

Cell A0 (10.5; 40.5)		Cell A1 (11.5; 40.5)		Cell A2 (12.5; 40.5)		Cell A3 (13.5; 40.5)		Cell A4 (14.5; 40.5)	
V_s (km/s)	h (km)	V_s (km/s)	h (km)	V_s (km/s)	h (km)	V_s (km/s)	h (km)	V_s (km/s)	h (km)
0.00	1.8	0.00	2.5	0.00	2.5	0.00	1.5	0.00	0.5
1.16	1.2	1.38	0.7	1.20	0.7	1.20	2.2	2.60	1.0
3.01	2.0	3.45	1.0	3.45	1.0	3.45	1.0	3.00	1.5
3.12	1.0	3.52	1.8	3.95	1.8	3.95	1.3	3.35	3.0
3.24	1.0	–	–	–	–	–	–	–	–
3.75–3.95	8–16	3.65–3.75	18–22	3.60–3.70	15–25	4.25–4.55	3.5–8.5	2.40–2.70	4–5.5
4.15–4.45	40–50	4.20–4.40	25–37	4.20–4.60∗	13–18	3.40–3.60∗	10–15	3.30–3.70	13–18
4.05–4.35	75–80	4.10–4.30	45–60	4.10–4.20∗	45–60	3.85–4.15∗	40–45	4.10–4.30	40–50
4.15–4.65	67.5–85	4.25–4.55	80–100	4.20–4.50∗	80–100	4.25–4.45∗	90–110	4.35–4.55	70–90
4.15–4.65	65–85	4.25–4.65	90–110	4.20–4.60∗	75–100	4.25–4.45∗	90–110	4.20–4.60	70–95
4.75	***	4.75	***	4.75	***	4.75	***	4.75	***
4.90	44	4.90	44	4.90	44	4.90	44	4.90	44

Cell A5 (15.5; 40.5)		Cell A6 (16.5; 40.5)		Cell B-2 (8.5; 39.5)		Cell B-1 (9.5; 39.5)		Cell B0 (10.5; 39.5)	
V_s (km/s)	h (km)	V_s (km/s)	h (km)	V_s (km/s)	h (km)	V_s (km/s)	h (km)	V_s (km/s)	h (km)
–	–	–	–	–	–	–	–	0.00	2.3
1.50	1.1	1.50	1.1	1.85	2.0	1.85	1.5	1.16	0.7
2.10	2.4	2.10	2.4	2.66	1.0	2.78	1.5	3.01	2.0
2.90	1.5	2.90	1.5	2.89	0.8	2.89	0.5	3.12	2.0
3.49	4.0	3.49	4.0	3.35	0.7	3.35	1.5	3.24	1.0
3.15–3.35	9.5–13.5	2.90–3.30	8–13	3.35–3.45	11–12	2.60–3.0	4–5	3.75–3.95	10–14
4.15–4.35	40–50	4.05–4.25	35–45	4.70–4.80	15–20	3.80–4.00	9–11.5	4.25–4.35	47.5–60
4.60–4.80	30–40	4.65–4.80	30–45	4.10–4.30	45–60	4.30–4.50	40–55	4.10–4.40	65–80
4.15–4.45	60–85	4.15–4.55	60–85	4.15–4.45	37.5–72.5	3.80–4.20	45–60	4.20–4.60	65–80
4.25–4.65	85–110	4.35–4.65	90–110	4.15–4.45	90–110	4.25–4.45	135–160	4.00–4.80	60–80
4.75	***	4.75	***	4.75	***	4.75	***	4.75	***
4.90	44	4.90	44	4.90	44	4.90	44	4.90	44

Cell B1 (11.5; 39.5)		Cell B2 (12.5; 39.5)		Cell B3 (13.5; 39.5)		Cell B4 (14.5; 39.5)		Cell B5 (15.5; 39.5)	
V_s (km/s)	h (km)	V_s (km/s)	h (km)	V_s (km/s)	h (km)	V_s (km/s)	h (km)	V_s (km/s)	h (km)
0.00	3.0	0.00	3.0	0.00	3.0	0.00	2.5	0.00	0.9
1.20	0.7	1.20	0.7	1.20	0.7	1.30	0.5	1.15	2.1
3.45	1.0	3.45	1.0	3.45	1.0	3.45	2.0	2.90	3.0
3.95	2.0	3.95	2.0	3.95	2.0	3.95	1.5	–	–
3.65–4.15	5.5–8.5	3.85–4.25	7.5–10.5	3.60–4.00	9–13	3.20–3.40	15–19	3.45–3.50	14–22
3.50–3.70∗	11–15	3.00–3.30∗	6.5–9.5	2.90–3.30∗	6.5–9.5	4.10–4.30∗	30–45	3.70–4.10	10.5–15.5
4.15–4.25∗	53.5–67.5	4.10–4.30∗	55–70	4.10–4.30∗	50–06	3.90–4.20∗	30–45	4.25–4.45	50–60
4.20–4.40∗	80–100	4.25–4.35∗	70–90	4.20–4.40∗	70–90	4.20–4.60∗	70–90	4.50–4.70	70–90
4.20–4.60∗	60–90	4.20–4.60∗	90–120	4.20–4.60∗	95–120	4.20–4.60∗	90–110	4.20–4.60	90–110
4.75	***	4.75	***	4.75	***	4.75	***	4.75	***
4.90	44	4.90	44	4.90	44	4.90	44	4.90	44

(continued on next page)

Table 3 (*continued*)

Cell B6 (16.5; 39.5)		Cell C1 (11.5; 38.5)		Cell C2 (12.5; 38.5)		Cell C3 (13.5; 38.5)		Cell C4 (14.5; 38.5)	
V_s (km/s)	h (km)	V_s (km/s)	h (km)	V_s (km/s)	h (km)	V_s (km/s)	h (km)	V_s (km/s)	h (km)
–	–	0.00	1.5	0.00	1.0	0.00	2.0	0.00	2.36
2.45	4.0	1.10	0.9	1.11	1.5	1.10	0.4	1.00	0.04
2.80	9.0	2.31	0.4	2.20	0.4	2.31	0.4	2.31	0.4
–	–	2.90	4.2	2.63	3.6	2.90	3.2	3.55	3.20
3.35–3.45	8–11	3.45–3.75	9–15	3.65–3.85	15–20	3.25–3.35	11.5–14.5	2.95–3.15	11–15
3.50–3.90	15–20	4.05–4.25	24–40	4.05–4.15	20–27.5	4.05–4.15	12–18	3.65–4.05	12–18
4.20–4.60	30–45	4.35–4.55	45–60	4.35–4.45	45–60	4.10–4.30	30–45	3.95–4.15	30–45
4.40–4.75	85–110	4.15–4.45	60–80	4.30–4.50	60–80	4.30–4.50	70–90	4.45–4.65	60–80
4.25–4.75	60–85	4.25–4.65	85–110	4.20–4.60	75–100	4.20–4.60	90–110	4.20–4.60	100–120
4.75	***	4.75	***	4.75	***	4.75	***	4.75	***
4.90	44	4.90	44	4.90	44	4.90	44	4.90	44

Cell C5 (15.5; 38.5)		Cell C6 (16.5; 38.5)		Cell D1 (11.5; 37.5)		Cell D2 (12.5; 37.5)		Cell D3 (13.5; 37.5)	
V_s (km/s)	h (km)	V_s (km/s)	h (km)	V_s (km/s)	h (km)	V_s (km/s)	h (km)	V_s (km/s)	h (km)
0.00	1.0	–	–	0.00	0.6	0.00	0.5	–	–
2.60	2.0	2.45	3.8	1.73	2.5	1.85	2.5	1.73	2.5
–	–	2.74	1.0	2.90	2.0	2.65	2.0	2.60	2.5
–	–	–	–	3.40	4.4	2.89	1.0	2.90	5.0
–	–	–	–	–	–	–	–	–	–
2.85–2.95	12.5–15.5	3.50–3.70	11–17	2.95–3.25	4.5–5.5	3.45–3.75	13–19	3.45–3.65	13–19
3.80–4.00	22.5–31.5	3.85–4.05	12–18	3.95–4.05	21.5–25.5	3.90–4.30	12–18	4.15–4.45	30–40
4.45–4.75	45–60	4.35–4.65	30–45	4.55–4.65	20–30	4.45–4.55	30–45	4.25–4.75	30–45
4–40–4.60	90–110	4.55–4.75	90–110	4.35–4.45	100–120	4.35–4.45	70–90	4.20–4.60	70–110
4.55–4.85	70–90	4.20–4.60	70–90	4.35–4.45	60–90	4.25–4.55	90–110	4.25–4.75	60–80
4.75	***	4.75	***	4.75	***	4.75	***	4.75	***
4.90	44	4.90	44	4.90	44	4.90	44	4.90	44

Cell D4 (14.5; 37.5)		Cell D5 (15.5;37.5)	
V_s (km/s)	h (km)	V_s (km/s)	h (km)
–	–	0.00	1.5
1.73	3.0	2.22	2.4
2.60	2.0	2.31	1.3
2.90	5.0	3.15	1.8
3.45–3.55	10–15	3.05–3.15	13.5–14.5
4.25–4.35	30–40	4.25–4.35	30–40
4.20–4.60	30–45	4.30–4.60	40–60
4.25–4.65	80–100	4.30–4.60	90–110
4.25–4.75	60.80	4.55–4.75	90–110
4.75	***	4.75	***
4.90	44	4.90	44

A similar crust–upper mantle geometry is observed in the nearby cell C3, but with different physical properties. In cell C4 the relatively high-velocity lid is absent: the ~12-km-thick soft mantle layer, underlying the crust–mantle transition, at ~19 km depth, has a V_s of about 4.10 km/s and overlies a mantle with V_s

Fig. 6. Each column gives the ranges of variability of the inverted parameters (see also Table 3) for the chosen structure (the solution of each set indicated by bold line in Fig. 5) of the cells (labeled in parenthesis) containing the recent volcanoes (indicated by full triangles in the central frame): Amiata–Vulsini (b1), Cimino–Vico–Sabatini (b2), Albani (a2), Roccamonfina (a3), Phlegraean Fields–Vesuvius (A4), Vulture (A5), Ischia (A3), Stromboli (C5), Vulcano–Lipari (C4), Etna (D5), Ustica (C3), Marsili (B4), Magnaghi (B1), Vavilov (B2), Montiferro and Monte Arci (A-2), Orosei and Dorgali (A-1), Capo Frasca (B-2), Capo Ferrato (B-1), Isola Ferdinandea (D2). Part (a) down to 350 km, parts (b) and (c) show a blow-up down to 100 and 40 km respectively.

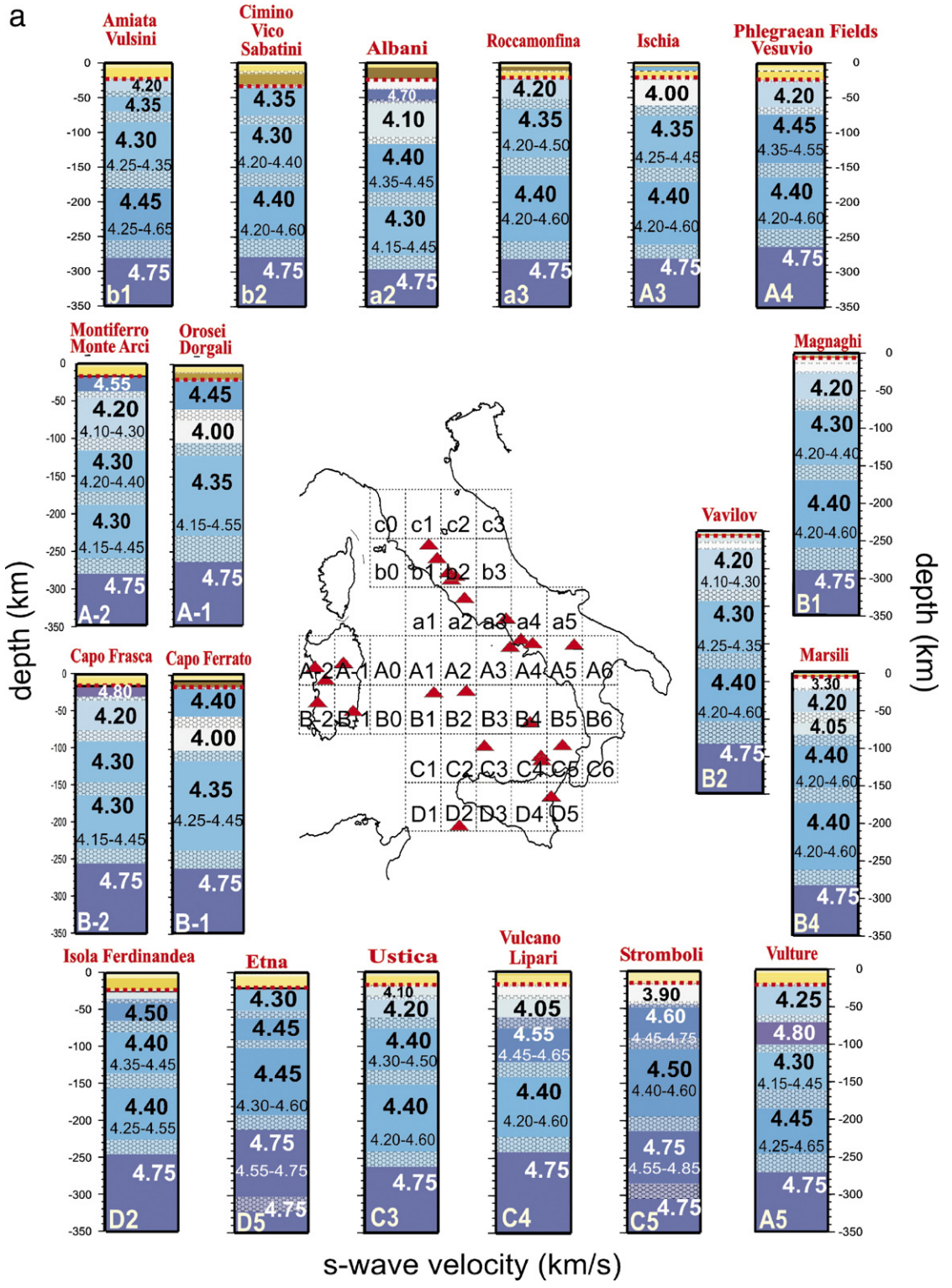
a
Amiata Vulsini
Cimino Vico Sabatini
Albani
Roccamonfina
Ischia
Phlegraean Fields Vesuvio
Montiferro Monte Arci
Orosei Dorgali
Magnaghi
Vavilov
Capo Frasca
Capo Ferrato
Marsili
Isola Ferdinandea
Etna
Ustica
Vulcano Lipari
Stromboli
Vulture
depth (km)
s-wave velocity (km/s)

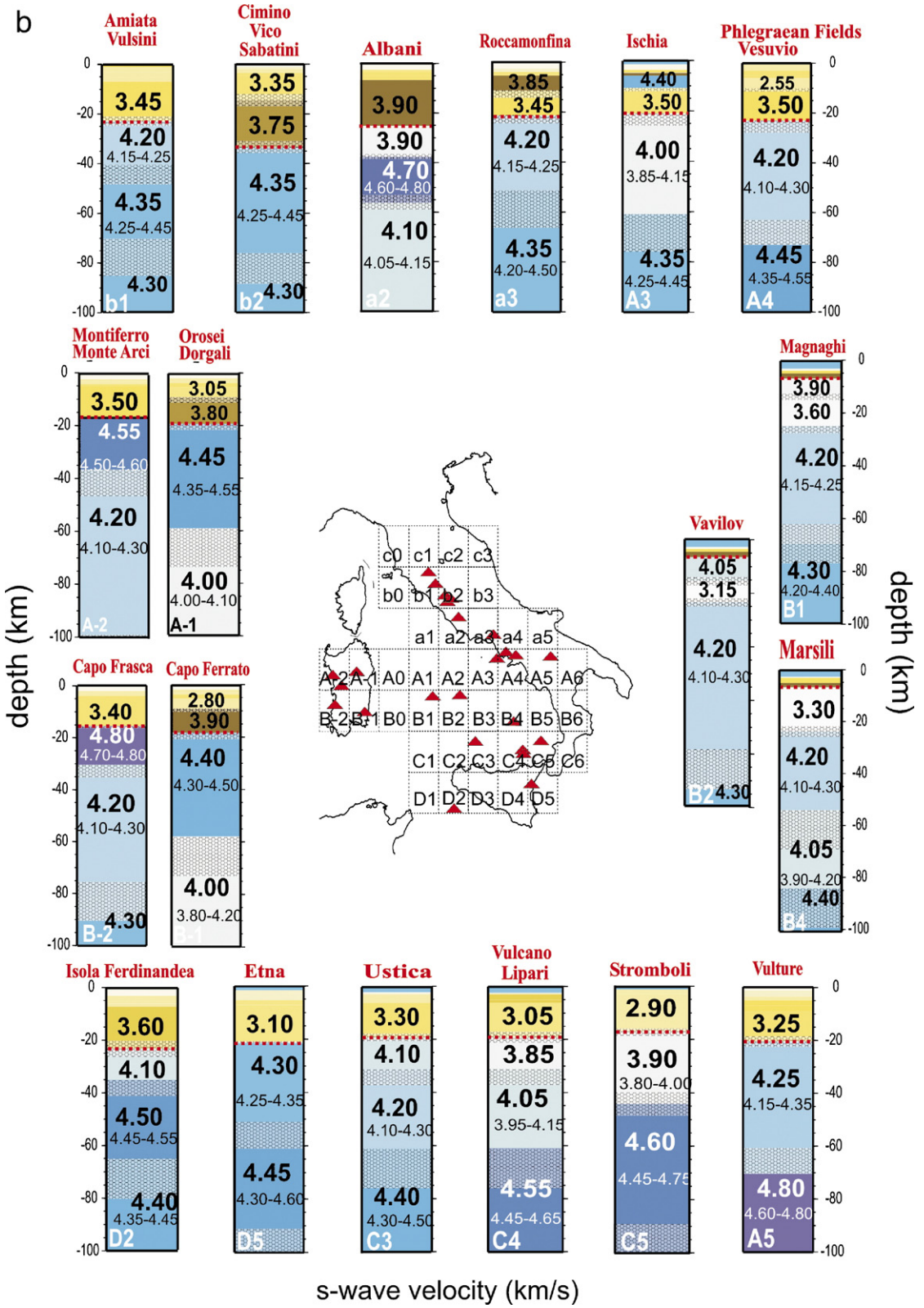

Fig. 6 (*continued*).

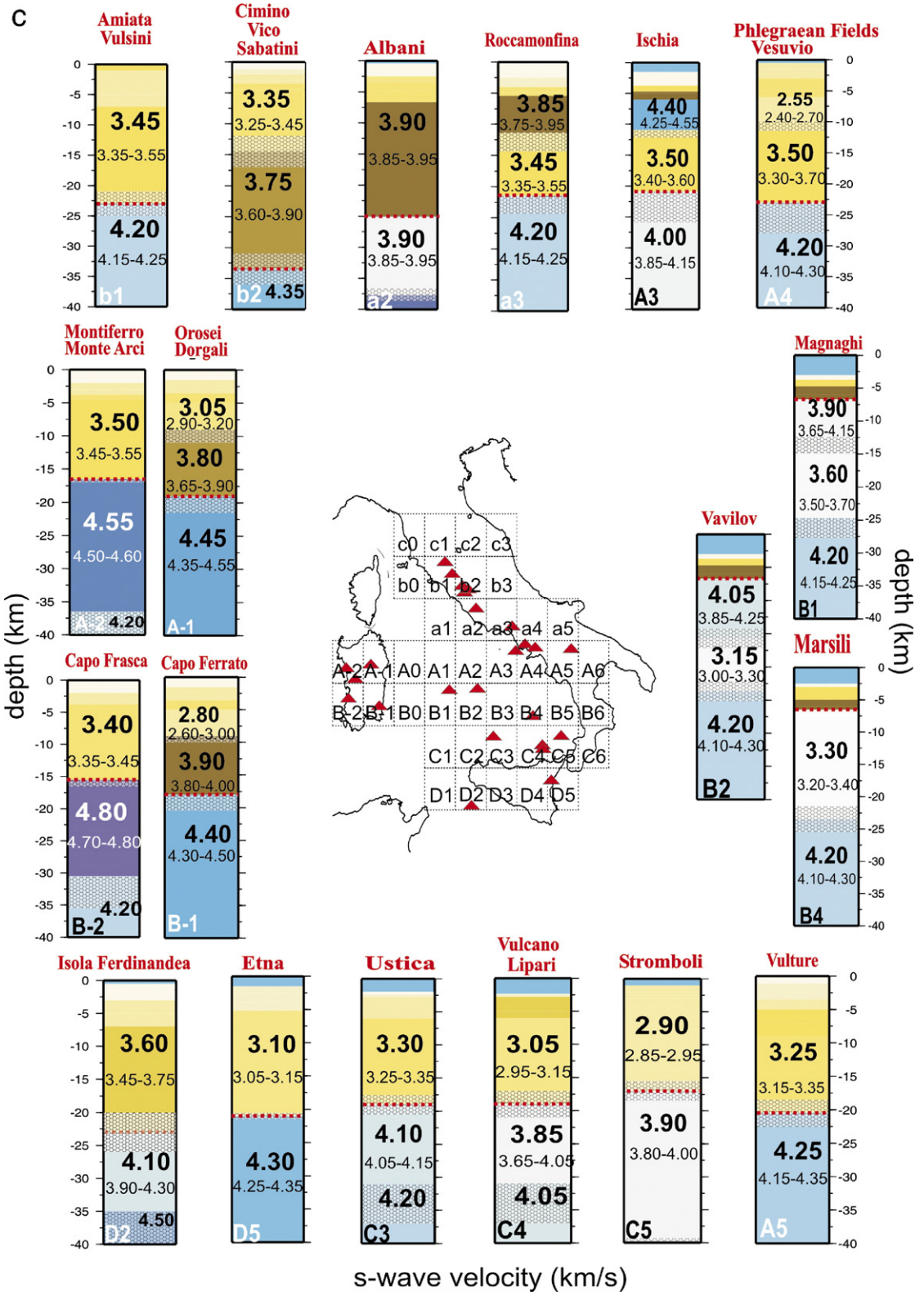

Fig. 6 (*continued*).

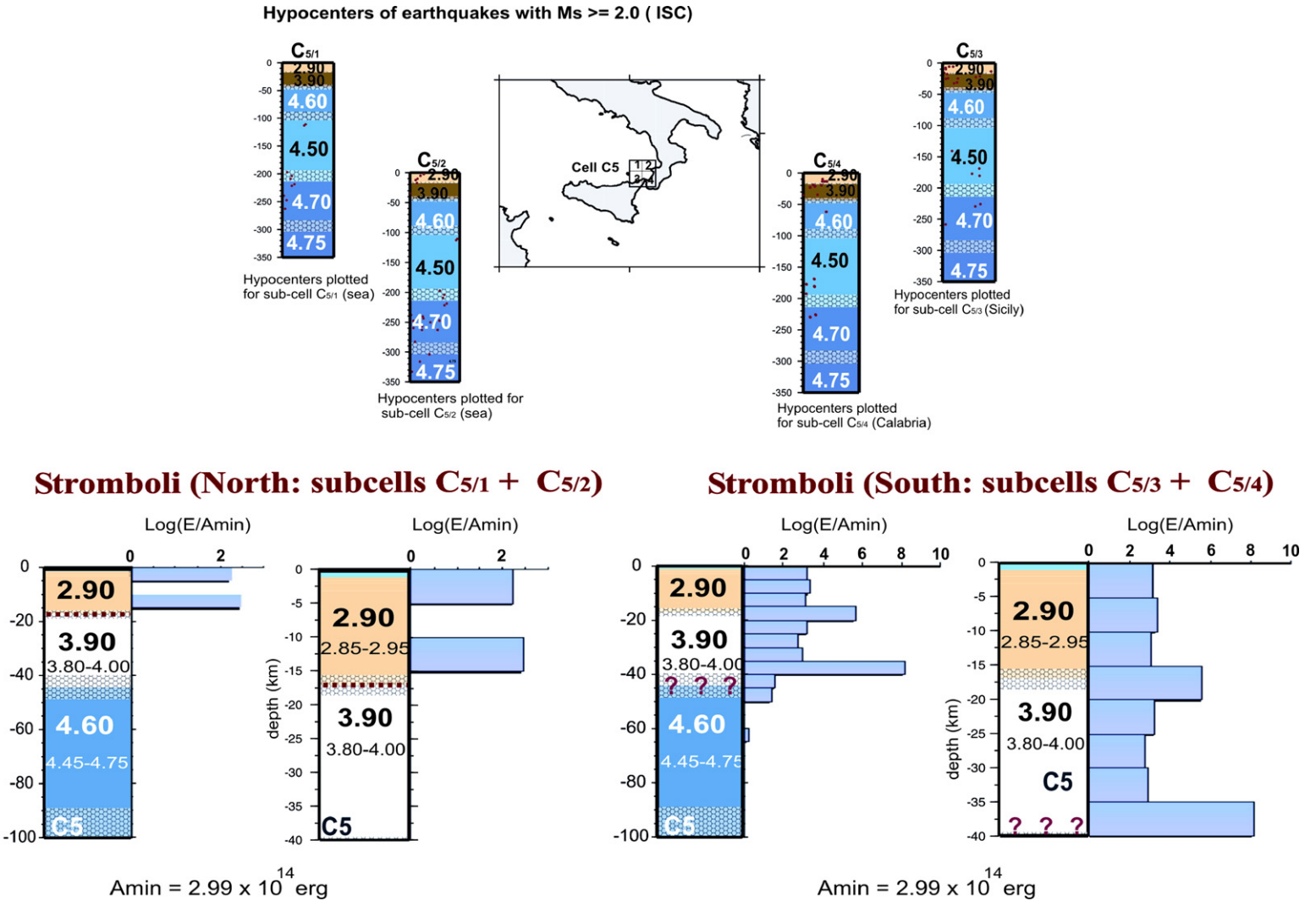

Fig. 7. Seismic energy vs. depth for all events with magnitude above the completeness threshold, defined by means of an exploratory analysis of the Gutemberg–Richter relation of the earthquake catalogue for each cell extracted from the International Seismological Centre (ISC) catalogue. Case of Stromboli: Cell C5 is divided into a northern (sub-cell C5/1+sub-cell C5/2) and a southern (sub-cell C5/3+sub-cell C5/4) part in order to highlight the seismicity space distribution and its contribution to the seismic energy as shown in the lower panel. The Moho depth is well defined (red broken line) in the northern part while uncertain (?) in the southern part of cell C5.

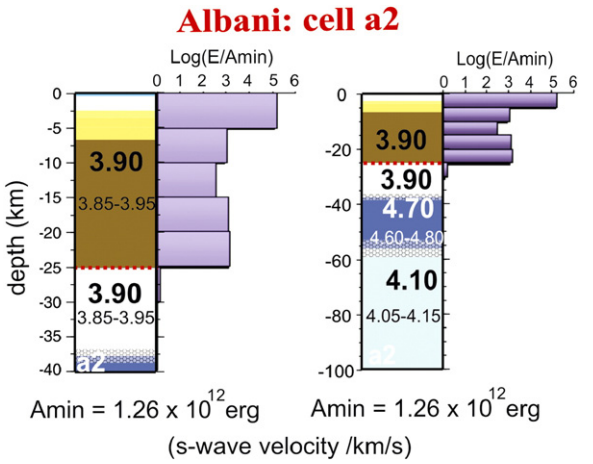

Fig. 8. Seismic energy vs. depth for Albani: Cell a2. Differentiation between crust and mantle material within a layer of constant V_s (about 3.9 km/s) using seismic distribution. The assumption is that the portion of the layer which is totally aseismic can be assigned to a soft, partially molten mantle, while the portion of the layer where seismicity is concentrated can be assigned to the brittle crust. See text for details.

of about 4.20 km/s. Below ~60 km of depth the mantle V_s of about 4.40 km/s extends to a depth of about 250 km.

More to the south, in cell D5 a 20-km-thick crust overlies a 30-km-thick mantle layer with V_s of about 4.30 km/s. Below this layer mantle material with V_s of about 4.45 km/s extends to about 200 km of depth.

The Sardinia block (cells A0, A-1, A-2, B0, B-1, B-2) is characterised by a crust about 20 km thick that is getting thicker as we move towards East; on the West (Sardinia trough) the lid is thin but fast. Therefore, the lithosphere reaches about 40 km on the West side, while it is about 70 km thick on the East. The largest difference is seen below about 50 km of depth: going from north to south, the asthenospheric velocity drops to about 4.00 km/s. Thus, the region exhibits, from East to West, a strong change in geometry of the uppermost LAS, while, from north to south, a very mild change in the physical properties of the asthenosphere is evident. For depths greater than about 120 km the mantle velocity is everywhere close to 4.3 km/s, till a depth of at least 250 km.

7. Regional lithospheric models from petrological–geochemical data

Plio-Quaternary magmatism is widespread in the Mediterranean area. The largest part of volcanic rocks represents upper mantle melts or their derivatives. Therefore, major, trace element and isotopic compositions of these rocks, especially the most mafic ones, can be used to infer the composition of the upper mantle for a wide region.

The circum-Tyrrhenian magmas show extreme variability in terms of both major and trace elements and for radiogenic isotope compositions. Fig. 9a is a classical Total Alkali vs. Silica (TAS) diagram showing that the circum-Tyrrhenian rocks spread over a very wide field, basically covering the entire spectrum of volcanic rocks occurring worldwide. Fig. 9b is a ΔQ vs. K_2O/Na_2O diagram, showing the degree of silica saturation for mafic rocks (MgO>4 wt.%), as well as

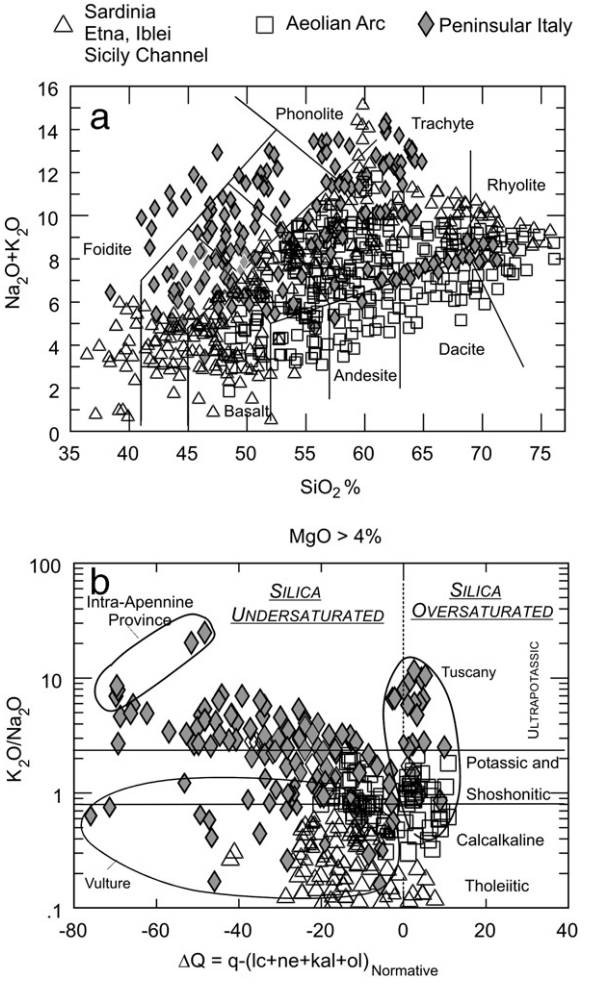

Fig. 9. (a.) Total alkalies vs. silica (TAS) classification diagram (Le Maitre, 1989) showing the large compositional variations of Plio-Quaternary volcanism around the Tyrrhenian Sea area. (b.) Classification diagram based on ΔQ vs. K_2O/Na_2O for Plio-Quaternary mafic rocks (MgO>4 wt.%) from the Tyrrhenian Sea area. ΔQ is the algebraic sum of normative quartz (q), minus undersaturated minerals leucite (lc), nepheline (ne), kalsilite (kal) and olivine (ol). ΔQ values assess the degree of silica saturation of rocks. Rocks with $\Delta Q>0$ are oversaturated in silica; rocks with $\Delta Q<0$ are undersaturated in silica. Modified after Peccerillo (2001a).

their petrogenetic affinity (Peccerillo, 2001a, 2003). ΔQ is the algebraic sum of normative quartz (q), minus undersaturated minerals (nepheline, leucite, kalsilite and forsterite), and measures the degree of silica saturation of magmas. Silica undersaturated magmas have negative ΔQ, whereas oversaturated magmas have $\Delta Q > 0$. Variable K_2O/Na_2O ratios denote different petrochemical affinity, from tholeiitic and Na-alkaline to calcalkaline, shoshonitic, potassic and ultrapotassic.

Potassic and ultrapotassic rocks in Central–Southern Italy display important petrological variations. Those from southern Tuscany are oversaturated in silica and are characterised by high Mg and low concentrations of Na_2O and CaO wt.% (see Peccerillo et al., 1988; Peccerillo, 2005). The most potassic types are known as lamproites and derive from a mantle that contained one or more potassium-rich phases (e.g., phlogopite, K-richterite), but was depleted in clinopyroxene (i.e., phlogopite-bearing harzburgite; Peccerillo et al., 1988; Melzer and Foley, 2000). These potassic phases are uncommon in upper mantle rocks and their presence beneath Tuscany and other zones around the Tyrrhenian Sea, reveals geochemical anomalies. Oversaturation in silica suggests a genesis in the uppermost mantle, possibly in the spinel stability field (e.g., Melzer and Foley, 2000).

The ultrapotassic rocks from some monogenetic volcanoes in the internal zones of Central–Northern Apennines are also low in Na_2O and Al_2O_3 but have high CaO and are strongly undersaturated in silica (Peccerillo et al., 1988; Peccerillo, 2005). These rocks are known as ultrapotassic *kamafugites* and are believed to derive from melting of a phlogopite-rich clinopyroxenite at high pressure possibly above 2 GPa (e.g., Wendlandt and Eggler, 1980; Edgar, 1987).

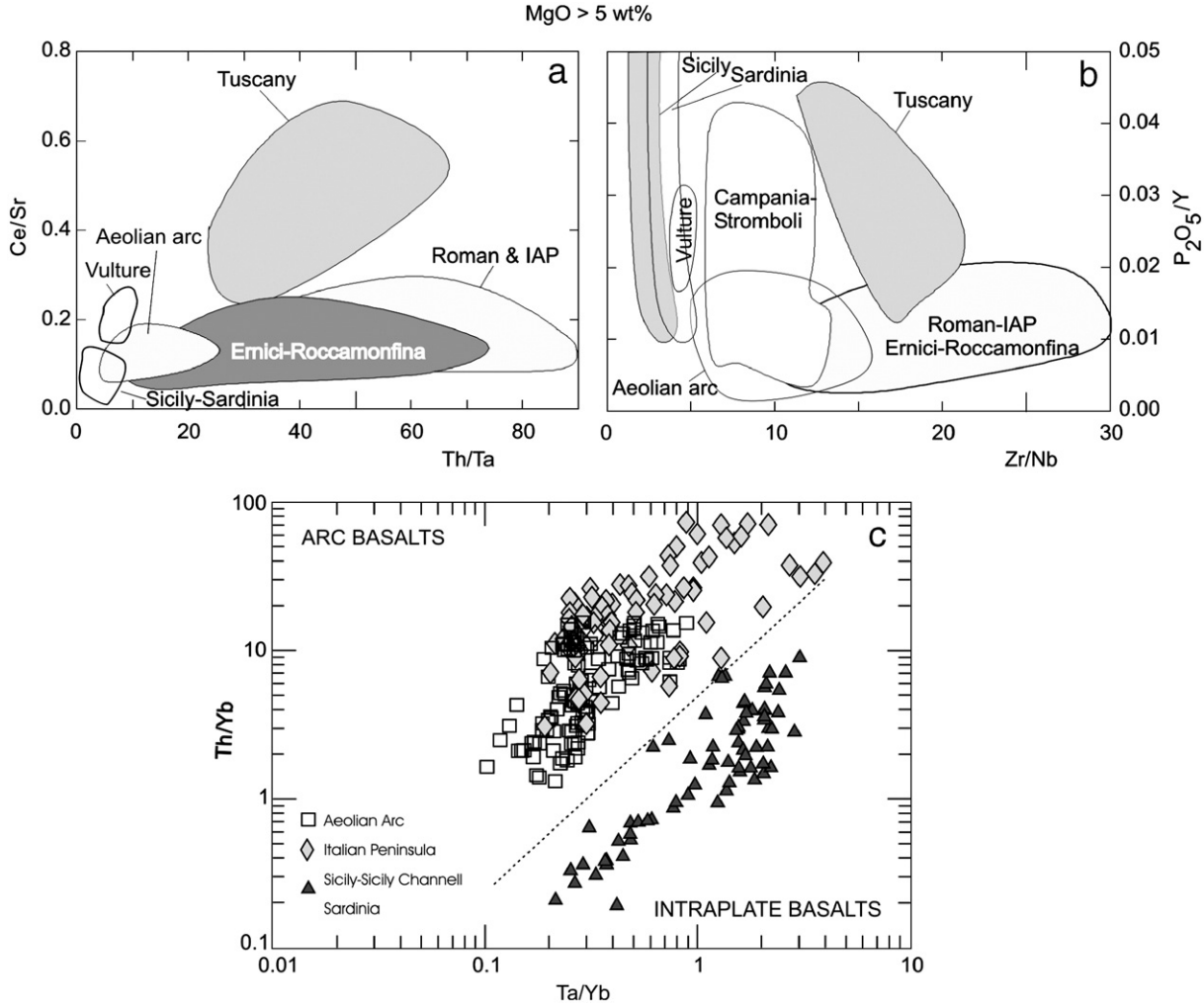

Fig. 10. Variation of trace element ratios in the Plio-Quaternary mafic rocks (MgO>4 wt.%) from the Tyrrhenian Sea area.

Potassic and ultrapotassic rocks from the Roman and Campanian areas have variable potassium contents and higher Na_2O, Al_2O_3 and CaO than lamproites. CaO is comparable or lower than kamafugites. These rocks are known as Roman-type potassic series (KS) and high-potassium series (HKS). KS rocks are moderately potassic and straddle the silica undersaturation boundary. HKS rocks have K_2O wt.% >3 and K_2O/Na_2O >2.5, and are undersaturated in silica. Except for K_2O, KS and HKS rocks do not show important differences for major elements. Their high K, Al, Na and Ca suggest a genesis in a phlogopite–clinopyroxene-bearing source, either a phlogopite–lherzolite or phlogopite–clinopyroxenite (Gupta and Fyfe, 2003). Different enrichments in potassium and degrees of silica saturation for KS and HKS are explained by variable degrees of partial melting at different pressures (possibly from 1 to 2 GPa). KS would be formed by higher degrees of melting and at lower pressure than HKS (e.g., Wendlandt and Eggler, 1980; Peccerillo, 2005 and references therein). However, variable isotopic signatures for these series found in some volcanoes (e.g., Ernici and Roccamonfina) require a heterogeneous source, characterised by variable degrees of enrichment in potassium and radiogenic isotopes.

A particular type of rocks outcrop at Mount Vulture. This volcano consists of alkaline rocks, which are very rich in both Na and K, with variable K_2O/Na_2O (De Fino et al., 1986; De Astis et al., in press with references). These characteristics make Mount Vulture distinct from any other volcano in Italy. A phlogopite–amphibole-rich peridotite may represent the parental rock of magmas of this centre (De Astis et al., in press).

The calcalkaline and shoshonitic rocks are concentrated in the Aeolian arc, but are also present in the Naples area (Campania) and in Tuscany (e.g., especially in the Capraia Island). These rocks have comparable Al, Ca and Na contents as the Roman-type KS and HKS rocks, but display lower potassium contents. The major element chemistry suggests a genesis in a lherzolitic sources, that contained moderate amounts of potassium-rich phases (Peccerillo, 2005 and references therein).

Finally, Na-alkaline, Na-transitional and tholeiitic rocks occur in eastern Sicily, Sicily Channel, Sardinia and the Tyrrhenian Sea floor. They have variable enrichments in alkalis, but, except for a few cases, sodium prevails over potassium. Various hypotheses have been suggested for the mantle sources of these rocks. However, most authors accept a common lherzolitic source containing little phlogopite and some amphibole, with tholeiitic rocks being generated by higher degrees of partial melting than alkaline magmas (e.g., Beccaluva et al., 1990; Trua et al. 1998; Lustrino et al., 2004).

In conclusion, heterogeneous and compositionally anomalous mantle sources are suggested by major element data for the volcanism in the Tyrrhenian Sea and surroundings. Regional distribution of magma types and their variable degree of silica saturation suggest strong lateral variations in the modal mineralogy of the upper mantle and different depths of partial melting (Peccerillo, 2003).

Support to this conclusion and additional information on mantle sources can be given by trace element and isotope geochemistry of mafic rocks around the Tyrrhenian Sea. Figs. 10 and 11 show the variation for some incompatible trace element ratios and for Sr–Nd–Pb isotope signatures. The most striking feature emerging from these diagrams is again the extreme compositional

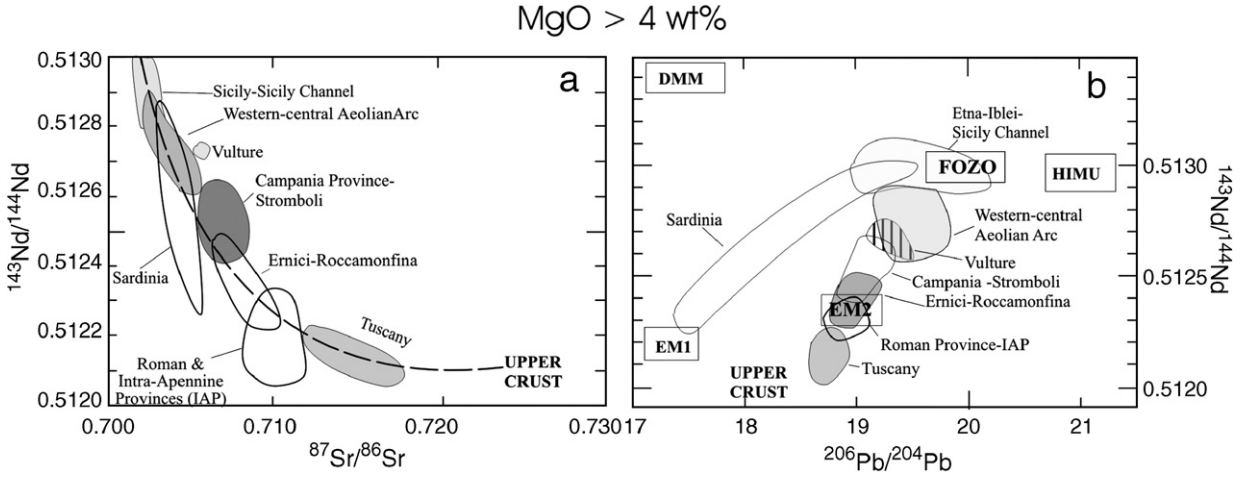

Fig. 11. Plot of $^{87}Sr/^{86}Sr$ vs. $^{143}Nd/^{144}Nd$ in the Plio-Quaternary mafic rocks (MgO>4 wt.%) from the Tyrrhenian Sea area.

variability and the strong regionality of magma compositions. This lends support to the idea that the upper mantle consists of a mosaic of compositionally distinct sectors, as indicated by major element variations. However, trace element and isotopes add details to such a picture. For instance, mafic rocks from Naples area (Campania) plot in the same field as Stromboli (Aeolian arc), whereas they show distinct compositions as the potassic rocks of the Roman area. This was not obvious from major element chemistry, and led Washington (1906) to suggest a single magmatic province for Roman and Campanian volcanoes. Moreover, Stromboli rocks are different from the equivalent types at Vulcano, in the Central Aeolian arc, in spite of the similar rock petrology of these two islands, which contain abundant shoshonitic and KS rocks (e.g., De Astis et al., 2000; Peccerillo, 2005). The rocks from Roccamonfina and Ernici have very variable trace element and isotopic characteristics for KS and HKS. KS rocks plot partially with Neapolitan volcanoes, whereas HKS resemble closely to Roman equivalents. Therefore, the

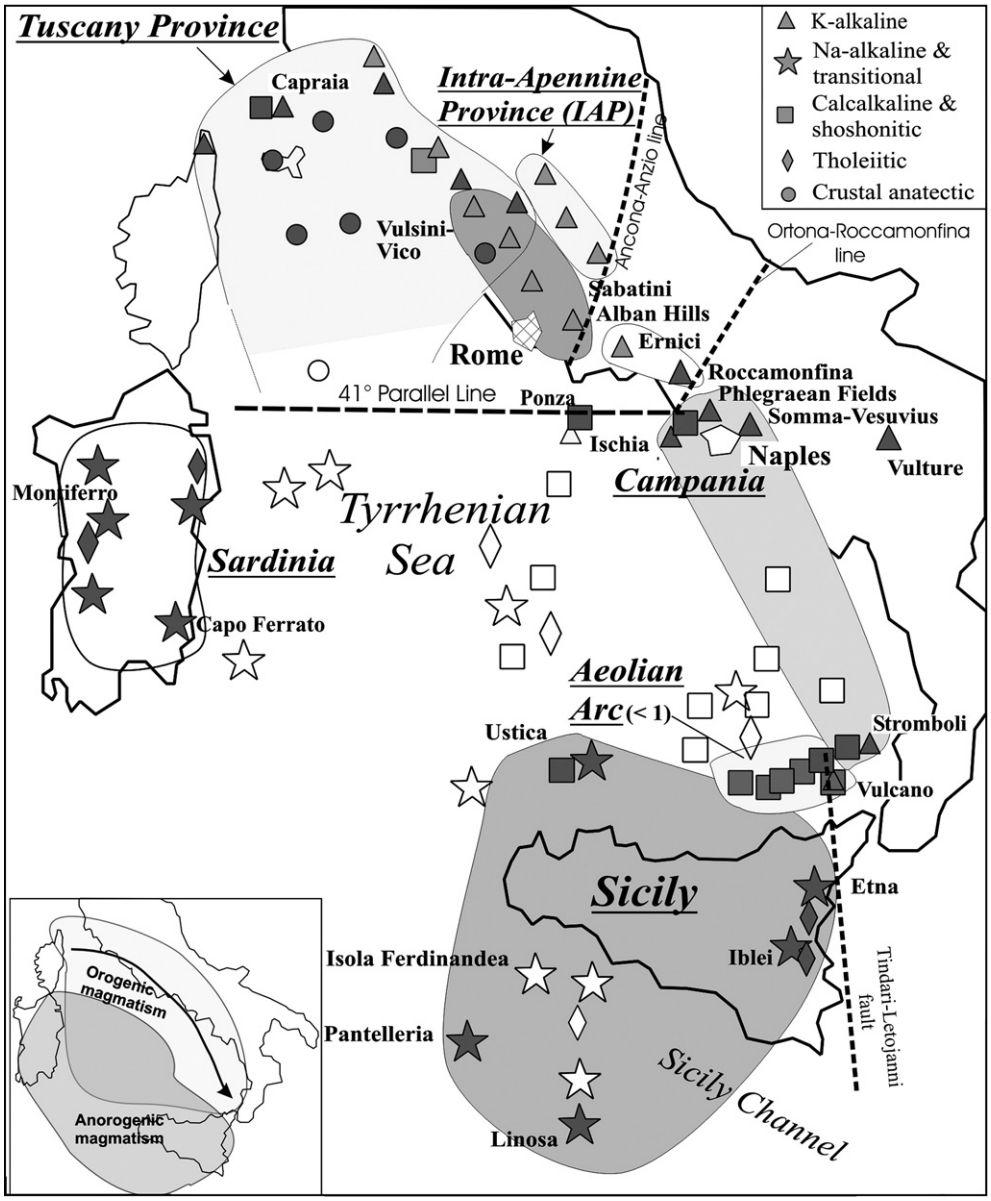

Fig. 12. Plio-Quaternary magmatic provinces in Italy. Modified after Peccerillo (2003). Inset map shows schematic distribution of orogenic and anorogenic Plio-Quaternary volcanic rocks in the Tyrrhenian area. Arrow in the inset map indicates age variation of orogenic magmatism.

Ernici–Roccamonfina region is characterised by the coexistence of two geochemically and isotopically distinct rock suites, which reveal two types of mantle sources, with Roman and Campanian affinity, respectively. Finally, calcalkaline and shoshonitic rocks from Tuscany have very different trace element and isotopic signatures than the equivalent rocks from the Aeolian arc and the Neapolitan area. The similar major element composition of these rocks suggests comparable physical conditions for magma genesis and a similar modal mineralogy for mantle sources. However, the distinct trace element and isotopic ratios require that the sources were geochemically different. Therefore, this represents the most striking case of decoupling between petrological (i.e., major elements) and geochemical (i.e., trace elements and isotopes) data, strongly substantiating the view that integrated petrological and geochemical studies are needed for fully understanding magmas and their sources.

In conclusion, major element, trace element and isotopic data on mafic rocks suggest that the Italian volcanism can be subdivided into different magmatic provinces, which were generated by petrologically and geochemically distinct mantle sources. These zones are (see Figs. 12 and 13) (Peccerillo, 1999, 2003, 2005; Peccerillo and Panza, 1999):

(1.) *Tuscany Province*. Ages of rocks in Tuscany range from about 8 Ma to some 0.1 Ma (Table 1), and become younger from west to the east. The 14 Ma old dyke of Sisco in north-eastern Corsica is also often considered as belonging to the Tuscany Province (Peccerillo, 2005 with references). Mantle-derived mafic magmas from this province range in composition from calcalkaline to ultrapotassic lamproitic, but have similar incompatible trace element ratios and high Sr isotopic signatures ($^{87}Sr/^{86}Sr$ up to 0.7170); these resemble closely some upper crustal rocks such as pelites and S-type granites. Anomalous compositions for mantle-derived melts in Tuscany are believed to reveal source contamination (or metasomatism) by upper crustal material, probably occurred during pre-Oligocene subduction processes (Peccerillo, 1999; Peccerillo and Martinotti, 2006). Crustal anactectic silicic rocks and hybrids between mantle-and crust-derived magmas do also occur in Tuscany. These have been generated by temperature increase connected with the emplacement of mafic magmas (Poli, 1992; Poli et al., 2002).

(2.) *Roman Province s.s.* or *Latium Province*. This province includes four large volcanoes (Vulsini, Vico, Sabatini and the Alban Hills) that consist of KS and HKS rocks showing variable degrees of evolution.

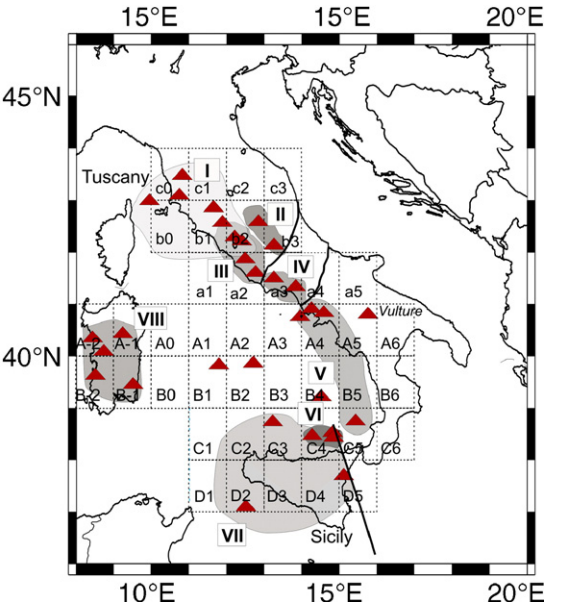

Fig. 13. Magmatic provinces, shown in Fig. 12, superimposed to the grid of the geophysical model. Gray areas represent the main magmatic provinces. I: Tuscany Province; II: Intra-Apennine Province; III: Roman Province; IV: Ernici–Roccamonfina Province; V: Campania–Stromboli; VI: Western–Central Aeolian arc; VII: Sicily Province; VIII: Sardinia. Red triangles represent the different recent and active volcanoes within the study area. (For interpretation of the references to colour in this figure legend, the reader is referred to the web version of this article.)

Trace element ratios are different from those of Tuscany potassic rocks. Radiogenic isotope compositions are also close to the crustal values, but are less extreme than in Tuscany (e.g., $^{87}Sr/^{86}Sr$ is typically around 0.710; e.g., Conticelli and Peccerillo, 1992; Conticelli et al., 2001). Roman rocks are younger than Tuscany ones, their age ranging from about 0.8 Ma to less than 0.1 Ma (Marra et al., 2004). This suggests that metasomatism of mantle sources occurred at later times than in Tuscany.

(3.) *Intra-Apennine Province (IAP)*. Strongly silica undersaturated monogenetic kamafugitic centres characterise this province. Major element composition of lavas is different from the nearby Roman Province, suggesting a distinct mineralogy for mantle sources (clinopyroxenite vs. lherzolite) and greater depth of partial melting for the strongly undersaturated kamafugites. However, ages, trace element ratios and radiogenic isotope compositions are similar, indicating that mantle sources of the Roman Province and the IAP underwent the same type of metasomatic modifications in the same geodynamic context, during subduction of the Adriatic plate beneath the Italian peninsula (Peccerillo et al., 1988; Peccerillo, 2005). Carbonate-bearing pyroclastic rocks with similar trace element and radiogenic compositions as lavas occur in the IAP and

have been suggested to represent carbonatites (Stoppa and Woolley, 1997). Such a hypothesis, however, has been rejected on the basis of the geochemically barren composition for the carbonate fraction and of the high oxygen isotopic ratios of whole rocks and separated minerals. These data strongly argue against a magmatic origin for calcite and suggest its derivation from the thick pile of sedimentary carbonate wall rocks (see Peccerillo, 2006).

(4.) *Ernici–Roccamonfina.* The province contains KS and HKS rocks that display distinct enrichments in potassium, incompatible elements and radiogenic isotopes. Calcalkaline rocks have been also recently found (Frezzotti, personal communication). As stated earlier, compositions of KS rocks overlap those of the Neapolitan volcanoes and, to a lower degree, Stromboli. HKS are very similar to the Roman equivalents, suggesting a compositionally zoned upper mantle beneath Ernici–Roccamonfina.

(5.) *Campania Province–Stromboli*. Campania volcanoes of Vesuvius, Phlegraean Fields, Procida and Ischia consist of dominant potassic and ultrapotassic rocks with a major element composition not much different from the equivalent rocks of the Roman area. However, isotopic and trace element signatures are distinct (e.g., lower Sr and higher Nd isotopic ratios, lower ratios of LILE/HFSE, etc.), suggesting a different nature for mantle sources (De Astis et al., in press). Trace elements and radiogenic isotopes show much similarity with Stromboli, which consists of calcalkaline, shoshonitic and potassic rocks (Peccerillo, 2001b). This suggests a common type of source for eastern Aeolian arc and Campanian area. Islands between Ponza and Ischia (Ventotene, Santo Stefano) also consist of shoshonitic to KS rocks similar to Campanian volcanoes.

(6.) *Aeolian arc*. Three sectors can be distinguished in the Aeolian arc, divided by a major tectonic lineament known as the Tindari–Letojanni fault system. The western Aeolian islands (Alicudi, Filicudi, Salina) mainly consist of calcalkaline lavas with low $^{87}Sr/^{86}Sr$ (=0.7035–0.7045). The central islands of Vulcano and Lipari consist of calcalkaline to shoshonitic rocks, with some undersaturated leucite-bearing shoshonites occurring at Vulcano (De Astis et al., 1997; Gioncada et al., 2003). Isotopic signatures of Vulcano and Lipari are not much different from those of the western arc. The eastern island of Stromboli consists of calcalkaline to leucite-bearing rocks, as observed at Vulcano. However, isotopic and trace element ratios are different and, as mentioned earlier, they resemble the Campanian volcanoes. Therefore, trace elements and radiogenic isotopes indicate strong variations in the nature and intensity of metasomatic modifications for mantle sources along the Aeolian arc. Note that only the central and eastern islands are volcanologically active.

(7.) *Mount Vulture*. This is the only Plio-Quaternary eruptive centre which is located east of the Apennine chain. Recent studies (De Fino et al., 1986; De Astis et al., in press) indicated that the Vulture rocks have many geochemical signatures akin to Campanian volcanoes, but also have some major and trace element ratios close to some OIB-type volcanoes such as Etna. Carbonate-rich material, believed to represent carbonatites, occur at Vulture (Stoppa and Woolley, 1997).

(8.) *Sicily and Sicily Channel.* This includes several recent to active volcanoes (Etna, Iblei, Ustica, Linosa, Pantelleria, Isola Ferdinandea or Graham Island and some seamounts), which show a tholeiitic to Na-alkaline affinity (Behncke, 2001; Rotolo et al., 2006 with references). Trace element geochemistry is typical of volcanic rocks from intraplate settings. Isotopic ratios are midway between DMM and HIMU, showing analogies with FOZO composition (Hoernle et al., 1996). Etna and Ustica show some trace element and isotopic (e.g., boron isotopes) signatures that highlight a subduction component in their origin (Cristofolini et al., 1987; Cinque et al. 1988, Armienti et al., 2004 with references). Overall, the diversity for compositional parameters indicates a distinct nature for mantle sources of Sicily volcanoes, which are situated either on the African plate (Iblei, Linosa, Pantelleria, Sicily Channel seamounts) or at the border between the African and the Ionian lithosphere (Etna), and the Tyrrhenian Sea basin (Ustica).

(9.) *The Sardinia Province.* The Plio-Quaternary tholeiitic to Na-alkaline rocks occurring in Sardinia (about 5 to 0.1 Ma) do not have significant differences with respect to similar intraplate rocks from Western Europe, except for somewhat higher silica and lower Ti (Lustrino et al., 2004 and references therein). However, except for a few occurrences in South–Central Sardinia (Capo Ferrato, Guspini and Rio Girone), the bulk of the volcanism has very peculiar trace element and isotopic composition, which are distinct from any other volcanic province in Western Europe. Isotopic compositions of northern Sardinian rocks resemble those of EM1, whereas trace element ratios are often intermediate between intraplate and arc rocks (Lustrino et al., 2004). This calls for a lateral geochemical heterogeneity of mantle sources, as well as for a unique mantle composition in northern Sardinia.

(10.) *The Tyrrhenian Sea floor.* Several volcanoes with calcalkaline, tholeiitic (MORB and arc-tholeiites) to Na-transitional and weakly alkaline affinity occur on

the Tyrrhenian Sea floor. The calcalkaline and shoshonitic seamounts form arcuate structures that become younger from west to south-east (Savelli, 1988; Locardi, 1993).

In several cases, the magmatic provinces described above are separated from each other by tectonic lines of lithospheric importance. These include the Tindari–Letojanni–Malta Escarpment fault, dividing western and eastern Aeolian arc, the Ancona–Anzio line, separating the Roman and the Ernici–Roccamonfina provinces, the 41° Parallel Line dividing the southern Tyrrhenian Sea and the Campania Province from Ernici–Roccamonfina (Fig. 12).

Another important aspect of the magmatism in the Tyrrhenian Sea area is that all the rocks along the Italian peninsula and in the Aeolian arc have high LILE/HFSE ratios (e.g., Th/Ta; Fig. 9c), with depletion of Ta, Nb and other HFSE (see Peccerillo 2005 and references therein). In contrast, Plio-Quaternary rocks from Sardinia, Sicily and Sicily Channel have relatively low LILE/HFSE with positive spikes of Ta and Nb. Since high LILE/HFSE ratios are typical of igneous rocks emplaced along converging plate margins, trace element data define two broad groups of volcanic rocks in the Tyrrhenian Sea area, with orogenic and anorogenic signatures, respectively. The distribution of these two groups is shown in the inset of Fig. 12.

8. The model for lithosphere–asthenosphere system tying petrological and geophysical data

From the joint analysis of seismic wave velocities and petrological–geochemical data it is possible to identify the following sectors for the LAS in the Tyrrhenian Sea and surrounding areas (see Figs. 6, 13 and 14):

(1.) *Vavilov* is characterised by a thin crust sitting on a thin soft lid bounding a very low-velocity layer in the mantle (Fig. 14). The crust is thin also under *Magnaghi* and *Marsili,* but, here, the lid seems to be missing or extremely thin (i.e. not detectable with our data). The very low velocities in the uppermost mantle can be interpreted as the indication of the existence of large amounts of melt (up to about 10%). This regional feature is compatible with the presence of mafic tholeiitic to transitional volcanic rocks, whose low to moderate abundances in incompatible elements support large degrees of mantle melting (Beccaluva et al., 1990; Trua et al., 2002).

(2.) *Ustica and Etna* are characterised by a thin continental crust with a thickness of about 20 km. The crust overlies a mantle whose uppermost part, in the depth range from 20 km to 60 km, has average V_s in the range from about 4.1 km/s (Ustica) to about 4.3 km/s (Etna). Notably, V_s are lower at Ustica than beneath the active volcano of Etna. Below this layer V_s is about 4.4 km/s till a depth of 210–260 km. The two volcanoes have similar geochemical signatures. Etna and Ustica have Na-alkaline affinity, and similar trace elements and FOZO to DMM radiogenic isotopic compositions (Gasperini et al., 2002; Stracke et al., 2005). Trace element ratios are in the range of intraplate volcanoes, even if evidence for a subduction-related geochemical component has been found (Cristofolini et al., 1987; Cinque et al., 1988; Armienti et al., 2004). Thus, the structure and composition of the magma sources beneath these volcanoes could be related to the contamination of intraplate-type mantle material by fluids or melts coming from a subducting slab. In the case of Etna, subduction component from Ionian plate contaminated the intraplate mantle of the side margin of the African plate during slab roll-back (Gvirtzman and Nur, 1999; Doglioni et al., 2001). The same process has been suggested for Ustica (Trua et al., 2003).

(3.) *Mount Vulture.* The upper mantle beneath Vulture differs from that beneath Etna and Ustica, because of the presence of a fast lid in the depth range 70–100 km. The Vulture magmas are the product of the interaction between intraplate and subduction-related reservoirs, but the subduction component is much stronger here than at Etna and Ustica (Peccerillo, 2005; De Astis et al., in press). These three volcanoes are all situated on a lateral position with respect to the presently active subduction zone in the southern Tyrrhenian Sea. This explains the observed interaction between intraplate and subduction-related components of magmas. Slab detachment and mantle inflow has been suggested to explain the intraplate signatures of Mount Vulture magmas (Peccerillo, 2001b; De Astis et al., in press). However, the presence of a low V_s layer below the depth of about 100 km suggests that slab detachment at Vulture eventually occurred at this depths rather than at shallow levels as envisaged by other authors (Spakman and Wortel, 2004).

(4.) *Stromboli, Phlegraean Fields and Vesuvius* are characterised by very similar trace element and radiogenic isotope signatures although the crust–mantle system shows some differences within the uppermost 70 km. Below the thin continental crust (about 23 km under Phlegraean Fields and Vesuvius and 17 km under Stromboli) there is a mantle wedge with V_s as low as about 3.90 km/s under Stromboli and 4.2 under Phlegraean Fields and Vesuvius. The layering under

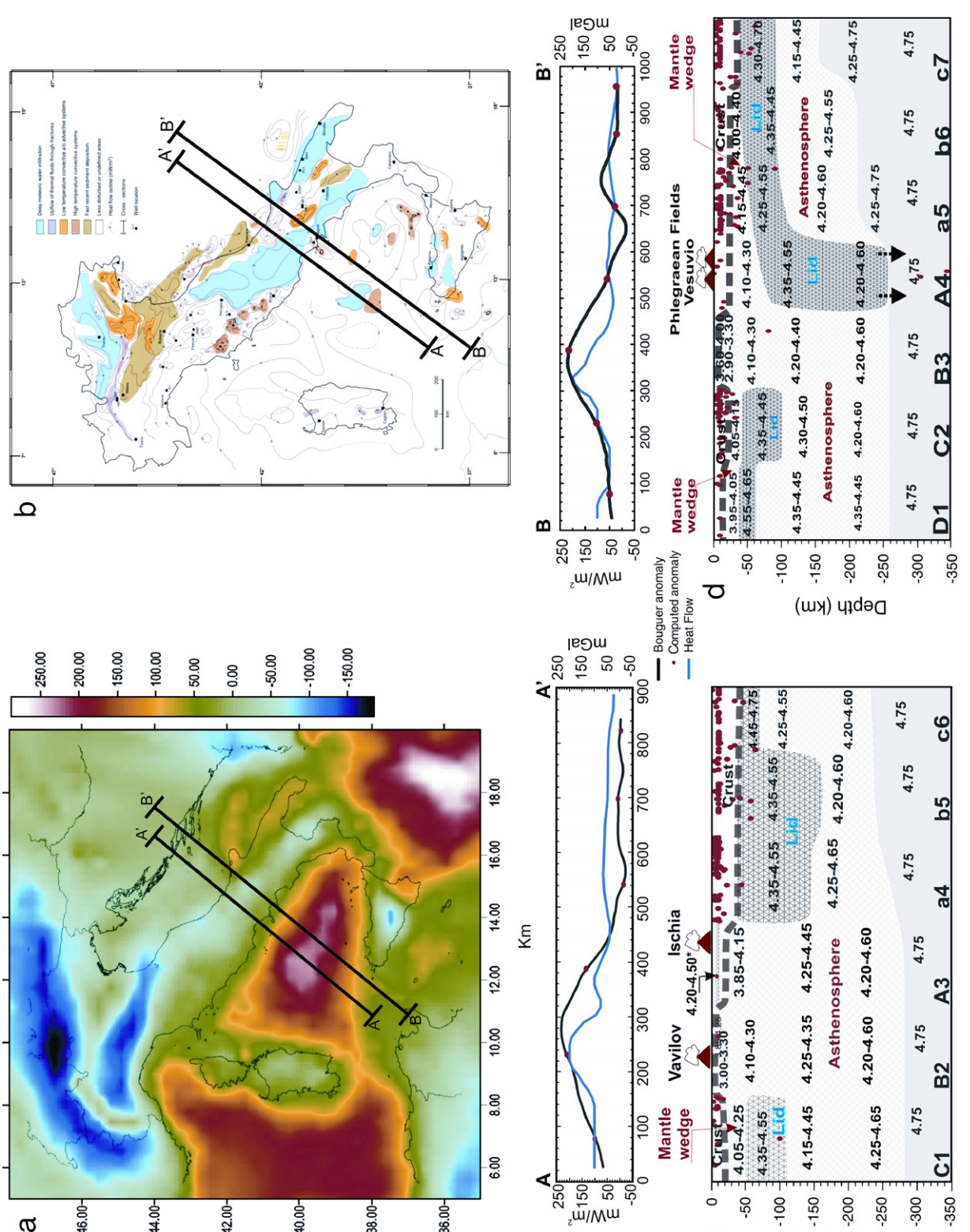
a
b
c
d
A
A'
B
B'
Km
mW/m²
mGal
Bouguer anomaly
Computed anomaly
Heat Flow
Depth (km)
Mantle wedge
Vavilov
Ischia
Phlegraean Fields
Vesuvio
Crust
Lid
Asthenosphere
C1
B2
A3
a4
b5
c6
D1
C2
B3
A4
a5
b6
c7

the wedge common to all these volcanoes is consistent with the presence of a subducted (Fig. 14) lithospheric slab (Ionian/Adriatic slab). The strong geochemical and isotopic similarity between Stromboli and Phlegraean Fields and Vesuvius may match well the matching of deep lithospheric structural models.

(5.) *Vulcano and Lipari* are in a thin continental crust, about 20 km thick, that overlies a very soft upper mantle (average $V_s \sim 3.85$ km/s). The lid, where the V_s reaches about 4.55 km/s, for depths greater than about 60 km, extends to about 120 km of depth. This lithospheric structural setting has affinities with the models described for Ustica. Due to the application of Occam's razor (see Section 6), the structural similarity between Vulcano and Stromboli lithosphere is not reflecting the different geochemical signatures. Nevertheless the sets of possible solutions are consistent with lateral variations that can satisfy the observed geochemistry. On the other side, the affinity between Vulcano, Lipari and Etna, although different in the uppermost mantle, for depths greater than about 120 km, could be explained by the common position along the Tindari–Letojanni–Malta fault zone. Ustica and Aeolian volcanic islands seem to have in common a mantle wedge with partial melting ranging from 1% to 5%, that well correlates with the presence of relevant volcanic bodies. Zanon et al. (2003) and Frezzotti et al. (2003), in their model of the Vulcano island and Aeolian arc magmatic evolution, suggest the existence of deep accumulation magma reservoirs, at about 18–21 km, and of a shallow accumulation level in the upper crust, at depths of 1.5–5.5 km. Polybaric ponding and evolution of magmas seem to be a regional feature in the Aeolian arc, as indicated by combined mineralogical, geochemical and fluid inclusion studies (Nazareni et al., 1998, 2001; Francalanci et al., 1999; Gauthier and Condomines, 1999; Frezzotti et al., 2003). It is possible to associate the layer with V_s at about 3.85 km/s, just below the Moho, to the deepest magma reservoir found by Zanon et al. (2003) and Frezzotti et al. (2003), while the resolution of our data does not allow us to sort out the uppermost (crustal) accumulation zone.

(6.) *Ischia* is geochemically and petrologically similar to the other Campanian volcanoes. Therefore the difference in the structural lithospheric model, with respect to the Phlegraean Fields and Vesuvius, and the similarity with that of the Tyrrhenian Seamounts, could be partly related to the resolving power of our geophysical data, however, this could also reveal a transition to the Tyrrhenian domain. Sr isotopic signatures of Ischia rocks are slightly less radiogenic than at Vesuvius and Phlegraean Fields, and support the coexistence of a Tyrrhenian-type and Campanian-type mantle. At Procida, situated midway between Ischia and Phlegraean Fields, Pb isotopic data are less radiogenic than in the other Campanian volcanoes, also supporting the presence of a depleted mantle source such as those of the Tyrrhenian Sea (De Astis et al., in press).

(7.) *Amiata*, *Vulsini*, *Albani*, *Ernici*, *Roccamonfina* sit on a thin continental crust not exceeding 25 km of thickness. Significant differences are seen below the Moho. Under Amiata, Vulsini, Roccamonfina the uppermost mantle is soft, with $V_s \sim 4.2$ km/s, and at larger depths the velocity is rather constant around 4.3–4.4 km/s till a depth of about 270 km, whereas at Alban Hills a low-velocity wedge overlies a high-velocity lid ($V_s \sim 4.7$ km/s), which is on top of a well developed low-velocity layer, reaching more than 110 km of depth. The presence of low-velocity layers may reveal the occurrence of melt beneath Alban Hills. The volcanism in this sector is younger than in the other Roman volcanoes, and eruptions have been reported here up to pre-Roman time (Voltaggio and Barbieri, 1995). *Cimino*, *Vico and Sabatini* are sitting on a continental crust, about 33 km thick and the underlying mantle is not too different from the one seen at Amiata, Vulsini and Roccamonfina. The region from Vulsini to Albani Hills shows similar petrological and geochemical characteristics, which match similar mantle structures, although KS and HKS rocks occur at Vico and Vulsini, whereas they are absent at Sabatini and Alban Hills. On the other side, the Roccamonfina–Ernici area differs significantly from the Latium volcanoes, especially the Alban Hills, because of the occurrence of both KS and HKS rocks with very distinct geochemical and isotopic compositions. Also in this case the differentiation of the provinces of Roccamonfina and Alban Hills finds a correspondence in the upper mantle structure. The two volcanic areas are separated by an important tectonic lineament, which is known as the Ancona–Anzio line.

Fig. 14. Selected cross-sections, AA′ and BB′, from the Tyrrhenian to the Dinarides, plotted over a) the map of the gravity anomaly (after Barzaghi et al., 2002); b) the map of the heat flow (after Della Vedova et al., 2001). (c) and (d) show, respectively, for AA″ and BB′: lower panels: cellular seismic structures down to 350 km (velocity ranges in km/s are taken from Table 3) along with a sketch of the geometry of the LAS and the recorded seismicity; upper panels: Observed vs. computed Bouguer anomaly along with the heat-flow profile. The computed gravity anomaly makes use of density models calculated from the velocity models reported in this study as described in Farina (2006). The easternmost part of the heat-flow profile makes use of Čermak and Bodri (1998) data.

(8.) *Northwestern Sicily Channel*. Volcanoes of this region include the well known ephemeral Isola Ferdinandea (Graham Island) and several seamounts (e.g., Cimotoe, Tetide etc.). They show a mafic tholeiitic to Na-alkaline composition, not much different from that of Etna and Iblei, in eastern Sicily. These volcanoes sit over a thin continental crust overlying a well developed low-velocity layer with V_S ~4.1 km/s. Below, a relatively fast layer defines an overall mantle structure that is not much different from that of the south-western Tyrrhenian Sea and Etna.

(9.) *Sardinia*. The LAS shows some significant variations between the western and eastern sectors, whereas less significant variations are observed between the northern and southern sectors. This contrasts with the strong difference in the amounts and compositions of magmatic rocks between northern and southern Sardinia (e.g., Lustrino et al., 2004). The most important peculiarity of the LAS in Sardinia is a high-velocity keel underlying the Moho in the western sectors, with V_S=4.55–4.80 km/s.

9. Geodynamic implications

The extremely variable structure of the lithosphere–asthenosphere system in the Tyrrhenian area and along the Peninsula is the result of its complex geodynamic history. Overall, the Cenozoic to Quaternary evolution has been characterised by the coexistence of compressional and extensional settings developed at the same time between converging continental plates (e.g., Doglioni et al., 1999; Faccenna et al., 2004). However, the rate of convergence between Africa and Europe has been much less significant than the east–west extension (e.g., Mantovani et al., 2002). The latter has been migrating from west to east, and has been positioned behind a compression front migrating in the same direction. As a consequence, a number of extensional basins have formed diachronously behind the Apennines–Maghrebian compression front. Orogenic magmatism followed the eastward migrating extensional regime, becoming younger from Sardinia (Oligo-Miocene) to the Tyrrhenian Sea floor and to the Southern Tyrrhenian Sea. The potassic magmatism of Central–Southern Italy is also considered as orogenic by several authors (Peccerillo, 2003, 2005 and references therein).

The eastward migration of the Apennines compression front is accompanied by a fragmentation of the Apennines lithosphere, with progressive ending of the active subduction zone from the Northern Apennines to the south (e.g., Sartori, 2003). The fragmentation of the Apennines lithosphere created sectors that had an independent evolution (Locardi, 1993; Sartori, 2003). This explains the magmatic diversity along the Italian peninsula as well as the variable structure of LAS.

Two main classes of hypotheses have been formulated to explain this evolution. Most authors suggest continuous west-dipping subduction of the Adriatic and Ionian plates beneath the southern margin of Europe (e.g., Carminati et al., 1998; Doglioni et al., 1999; Faccenna et al., 2004 and references therein). This follows an older subduction process, having an opposite dipping direction (e.g., Peccerillo and Martinotti, 2006). The subduction front has been migrating more or less continuously eastward, up to its present position in the southern Tyrrhenian Sea (e.g., Cavazza and Wezel, 2003). The opening of the western Mediterranean and Tyrrhenian Sea basins is considered as related to backarc spreading behind the eastward migrating compression front (e.g., Sartori, 2003 and references therein). Therefore, magmatism should be either related to subduction processes or to passive mantle ascent and decompression melting in a backarc extensional regime. Melting in areas outside backarc zones (e.g., Etna, Iblei and Sicily Channel) would be generated by local decompressional melting along transfer fault zones (e.g., Mantovani et al., 1997). Other hypotheses suggest the uprise of deep mantle plumes impinged into the lithosphere, generating Plio-Quaternary magmatism in Sardinia, in Sicily and Sicily Channel, but having some role also in the genesis of orogenic magmatism (Gasperini et al., 2000, 2002).

Our model of LAS, as inferred from integrated petrological, geochemical and geophysical data, argues against a plume role in the Italian magmatism. The changes in the geometry and structure of LAS are likely mimicking the changes in the distribution and chemistry of the recent and active magmatism. Accordingly, someone would better argue for a lithosphere dynamics (than plume dynamics), as a process in favor of chemical and physical interactions between crust and mantle. Furthermore, this process is required in order to reconcile both the pattern of the ongoing and recent stress field and the organized space distribution of the different magmatic provinces. Therefore recycling of crustal materials is likely to be the main contributor to the upper mantle heterogeneity of the observed magmatism. Much of this recycling is shallow therefore excluding deeper sources. Furthermore, recent studies (e.g., Balyshev and Ivanov, 2001; Anderson, 2005) have shown that simple heat conduction from the ambient mantle in which the lithosphere settles are enough to explain both high and low-velocity anomalies, without invoking deeper heat sources such as the one of a plume ascent. In addition, the thermal structure of a continent

is controlled by pre-existing compositional variations (e.g., Lee et al., 2001). A mantle plume hypothesis has been particularly invoked for northern Sardinia, to explain the peculiar EM1-type isotopic and geochemical compositions of Plio-Quaternary volcanic rocks in that region (Gasperini et al., 2000). However, our model indicates that there are no differences in the structure of the LAS in Sardinia, for depths larger than 120 km. This leads to conclude that, either the plume is deeper than the sector investigated in the present work or that the differences in the volcanic rocks geochemistry relate to differences in the lithosphere, or in the LAS above about 100 km of depth. A very rigid keel is present beneath the Moho in Sardinia, a feature that is not observed elsewhere in the Tyrrhenian Sea area. Such a particular lithospheric structure matches the particular geochemistry of Sardinia rocks, although our data do not allow to further constrain the significance of these peculiarities.

The cartoon showing the three-dimensional geodynamic scheme of the Tyrrhenian basin and bordering volcanic areas, including the subduction of the Ionian–Adria lithosphere in the Southern Tyrrhenian Sea (Fig. 15) is based on the models discussed here and reported in Table 3 and Fig. 5 and on selected cross-sections as the ones reported in Fig. 14.

In the Northern and Central Apennines, Fig. 15 clearly highlights lithospheric roots reaching depths of around 130 km. This present-day configuration of the crust and upper mantle that is the result of complex evolutionary stages of thickening and thinning of the lithosphere in interaction with the underlying asthenosphere, may contribute body forces to the regional geodynamics. As already shown by Chimera et al. (2003) the imaged uppermost mantle supports the lithospheric delamination beneath the peninsula and provides a unifying background for petrological and geochemical studies of recent magmatism and volcanism in Tuscany. Furthermore, Ismail-Zadeh et al. (2004) have shown that buoyancy forces, that result from the density distribution, govern the present-day dynamics of the lithosphere within North–Central Italy and can explain regional coexisting contraction and extension and the shallow depth and unusual distribution of intermediate depth earthquakes. A similar structure of the lithosphere–asthenosphere system with clear evidence of a low-velocity mantle wedge, which decouples the underlying high-velocity lithospheric mantle from the crust is evident up to the Alban Hills in Central Italy. In the Northern and Central Apennines the low-velocity zones seem to be more controlled by temperature than by composition, given the good agreement with the heat-flow data (e.g., Chimera et al., 2003).

The Roccamonfina region is characterised by the coexistence of two geochemically and isotopically distinct rocks suites, which reveal two types of mantle sources, with Roman and Campanian affinity and exhibits a peculiar lithosphere–asthenosphere structure in correspondence of a very sharp gradient in heat-flow data (Della Vedova et al., 2001). The seismic velocities in this region may be controlled

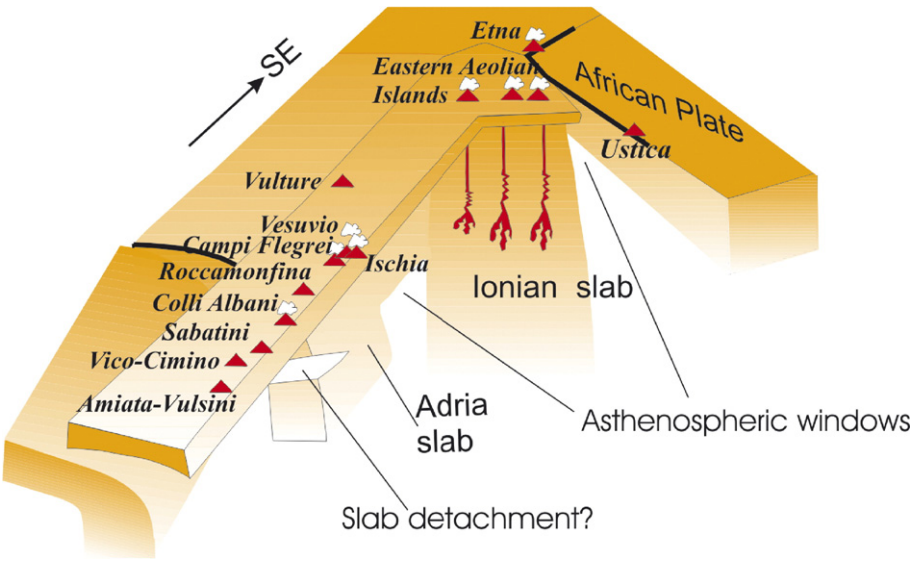

Fig. 15. Cartoon schematizing the geometry of the lithosphere in the Tyrrhenian basin and surroundings. The bold lines represent the Ancona–Anzio and Tindari–Letojanni–Malta structural features. See text for further details.

both by composition and temperature. Therefore, the known collocation, from the structural point of view, of Ernici–Roccamonfina as a boundary at the intersection between the Central and Southern Apennines is further confirmed by geophysical, petrological and geochemical data.

As shown in Fig. 15, beneath the Southern Apennines, a likely progressive detachment towards the south is inferred. Right below the Alban Hills the pronounced low-velocity layer in-between the high-velocity lithospheric mantle, also evident beneath Roccamonfina, leaves place to a continuous high-velocity subducting slab beneath the Campanian volcanoes towards the south (Fig. 14). This observation also reported by De Gori et al. (2001) on the basis of body-wave tomography reconciles the slab-enriched mantle source of the Campanian volcanism. Towards the south, below Vulture, a high-velocity lithospheric mantle is observed in the continental part of the Peninsula and no continuation of the subducting slab is reported as already reported by Panza (1978). This is interpreted as a slab-window in correspondence of north Calabria that would require a dynamics similar to that reported by Gvirtzman and Nur (1999) for the Etna volcano. This would reconcile the unifying petrological, geochemical elements of the Etna and Vulture (De Astis et al., in press). The slab-window will further support the existence of a lithospheric tear fault with a left lateral kinematics along the Sangineto line, between the Calabrian arc and the southern Apennines, acting as the equivalent of the right-lateral tear fault along the Taormina line. Tearing and roll-back of the Ionian slab will be further accelerated by sideways asthenospheric flow. The Ionian slab exhibits a well-pronounced low-velocity zone that could represent the serpentinized and attenuated continental lithosphere already reported below the Ionian by Panza and Pontevivo (2004). This layer when subducted gets thicker, consistently with the dehydration of serpentinite and may reach a depth of about 150–200 km (Ulmer and Trommsdorff, 1995). The presence of a sizeable layer of serpentinized material may be consistent with the recent strong uplift, since about 0.7 Ma as proposed by Westway (1993). The integrated use of geophysical, petrological and geochemical data led us to infer three possible types of processes that are likely governing the lithosphere dynamics in the Tyrrhenian and Italian Peninsula: delamination in the Northern and Central Apennines, slab detachment to continuous subduction in the Southern Apennines, slab roll-back and tearing with sideways asthenospheric flow through slab-windows in the Calabrian Arc with a likely slab detachment.

10. Conclusions

Integrated petrological, geochemical and geophysical studies have been used to demonstrate the capability of this integrated approach to work out reliable models for the LAS in a geological complex regions. Petrological and geochemical data about young volcanic rocks can be used to infer mantle source compositions and to detect possible compositional heterogeneities, both laterally and vertically. The parallel study of the V_s velocities provides tomography images that can be integrated with the results of geochemical–petrological studies to produce a holistic model of the LAS.

The method has been applied to the Tyrrhenian Sea and adjacent areas, a complex region characterised by a very wide variety of Plio-Quaternary volcanic rocks and by a complex lithosphere–asthenosphere structure.

The main features identified by our geophysical study are: (1) a low V_s mantle wedge, just below the Moho, as the common feature detected in most of the cells containing inactive recent volcanoes (Amiata, Vulsini, Albani Hills and Roccamonfina) in the Tuscany and Roman regions; (2) a fast body dipping westward as a common feature of Aeolian islands, Vesuvius, and Phlegraean Fields; (3) a distinct mantle structure for volcanoes of the Roman province with respect to those of Campania and Aeolian arc; (4) a very shallow crust–mantle transition and a very low V_s just below it, in correspondence of the submarine volcanic bodies (Magnaghi, Marsili and Vavilov) indicating high amounts of magma production; (5) the subduction of the Ionian lithosphere towards NW below the Tyrrhenian Basin; (6) a variable LAS, in the East–West direction, beneath Sardinia, limited to the uppermost 120 km, in spite of the large regional diversities in the amount and type of magmatism from north to south (Lustrino et al., 2004).

Petrology and geochemistry reveal rocks ranging in composition from tholeiitic to calcalkaline to sodium-and potassium-alkaline and ultra-alkaline. Scrutiny of the relevant data allows us to recognize several magmatic provinces, which display distinct major and/or trace element and/or radiogenic isotope signatures. The data from mafic volcanic rocks allowed us to establish a number of distinct provinces, that likely generated compositionally diverse mantle sources. Most of these provinces can be identified in LAS structure, as well.

The combined analysis of petrological, geochemical and geophysical data reveals a surprisingly close match

between geophysical characteristics of the lithosphere–asthenosphere and the compositions of magmatic rocks erupted at the surface in the various regions. This suggests that variations of seismic waves velocity in the mantle could be related to compositional differences of mantle sources, and not only to pressure and temperature variations. The present paper, therefore, provides important constrains that must be considered by geodynamic models for the evolution of the Alpine–Apennines systems thus highlighting that integrated petrological–geophysical studies are pivotal to achieve a better understanding of geodynamics.

Acknowledgements

The authors express their gratitude to an anonymous referee and to Eugenio Carminati for constructive reviews. Part of this research is funded by Italian MIUR Cofin (2001: Subduction and collisional processes in the Central Mediterranean; 2000: Active deformation at the northern boundary of Adria; PRIN 2004: Modelling of the mantle–crust system by petrological and geophysical methods), GNDT (2000: Determinazione dello stile di deformazione e dello stato di sforzo delle macrozone sismogenetiche italiane) and INGV (Eruptive Scenarios from Physical Modelling and Experimental Volcanology). The research on Italian magmatism has been funded by GNV-INGV, MIUR-PRIN 2004 and by the University of Perugia.

Appendix A. Estimate of resolution

When the tomography problem reduces to solving the Poisson equation (Eq. 14 in the text), the resolution is estimated at any point by the size of the averaging area, similarly to the Backus–Gilbert method, where the resolution is given by the length of the averaging interval.

The transfer of the approach to the case of two dimensions allows us to estimate the resolution from the radius of the equivalent circular or elliptical averaging area. The averaging kernel is defined as a linear combination of data kernels. Since any solution of the linear inversion can be represented as a linear combination of data:

$$\hat{m}(r) = \sum a_i(r)\delta t_i \tag{A1}$$

it follows that the averaging kernel $A(r,r')$, specified by:

$$\hat{m}(r) = \int A(r,r')m(r')\mathrm{d}r'$$

where $m(r)$ is any solution that satisfies the data, can be expressed as:

$$A(r,r') = \sum_i a_i(r)G_i(r')$$

In the 1D problem, Backus and Gilbert (1970) suggested the r.m.s. deviation of the integral of the averaging kernel from Heaviside's function as the criterion of similarity between the kernel and the delta function. Ditmar and Yanovskaya (1987), in the 2D approach, consider the following criterion of the deviation from the delta function:

$$s(r) = \int |E(r,r')-\varepsilon(r,r')|^2 \mathrm{d}r' \tag{A2}$$

the integration being over the entire area of study, while the vector function $E(r,r')$ and $\varepsilon(r,r')$, for the flat case, are given by:

$$divE = A(r,r'),$$

$$div\varepsilon(r,r') = \delta(r-r').$$

The average size of the averaging area is determined by considering a normalized circular averaging kernel that is different from zero in the circle of radius R and is centred at "r". The radius R is chosen so that the value of $s(r)$ for this kernel would equal that given by Eq. (2) based on the same data sample. The size of the averaging area at "r" is then estimated by the radius R of the equivalent circular area. It was shown by Ditmar and Yanovskaya (1987) that this equivalent averaging area for the flat Earth case has the radius:

$$R = \exp(0.75-a^T Sa + 2a^T\psi) \tag{A3}$$

where the matrix S is defined by:

$$S_{ij} = \int_{L_{0j}} \psi_i(r_i)\frac{\mathrm{d}s_j}{V_0}$$

$a(r)$ is the vector of coefficients in Eq. (1), $\psi(r)$ being the vector of base functions. When the resolution is estimated by the radius of the equivalent circular area, it does not consider the resolution along different directions. But, when there is some preferred direction for the paths, the resolution along the azimuth of preferred path directions must be worse than that in the perpendicular directions. The method for estimating an azimuth-dependent resolution for the flat Earth case is described by Yanovskaya (1997).

References

Ahrens, T.J., 1973. Petrologic properties of the upper 670 km of the Earth's mantle; geophysical implications. Phys. Earth Planet. Inter. 7, 167–186.

Aki, K., Lee, W.H.K., 1976. Determination of three-dimensional velocity anomalies under a seismic array using first P arrival times from local earthquakes. Part 1. A homogeneous initial model. J. Geophys. Res. 81, 4381–4399.

Aki, K., Richards, P.G., 1980. Quantitative Seismology. Freeman and Co., San Francisco.

Aki, K., Christoffersen, A., Husebye, E.S., 1977. Determination of the three-dimensional seismic structure of the lithosphere. J. Geophys. Res. 82, 277–296.

Alessandrini, B., Beranzoli, L., Mele, F.M., 1995. 3D crustal P-wave velocity tomography of the Italian region using local and regional seismicity data. Ann. Geofis. 38 (2), 189–211.

Alessandrini, B., Beranzoli, L., Drakatos, G., Falcone, C., Karantonis, G., Mele, F.M., Stavrakakis, G.N., 1997. Tomographic image of the crust and uppermost mantle in the Ionian and Aegean regions. Ann. Geofis. XL (1), 151–160.

Allegre, C.J., Minster, J.-F., 1978. Quantitative models of trace element behaviour in magmatic processes. Earth Planet. Sci. Lett. 38, 1–25.

Anderson, D.L., 2000. The thermal state of the upper mantle; no role for mantle plumes. Geophys. Res. Lett. 27, 3623–3626.

Anderson, D.L., 2005. Reheating Slabs by Thermal Conduction in the Upper Mantle. In: www.mantleplumes.org.

Appora, I., Eiler, J.M., Matthews, A., Stolper, E.M., 2003. Experimental determination of oxygen isotope fractionation between CO_2 vapor and soda-melilite melt. Geochim. Cosmochim. Acta 67, 459–471.

Armienti, P., Tonarini, S., D'Orazio, M., Innocenti, F., 2004. Genesis and evolution of Mt. Etna alkaline lavas: petrological and Sr–Nd–B isotope constraints. Period. Mineral. 73, 29–52.

Babuska, V., Plomerova, J., 1990. Tomographic studies of the upper mantle beneath the Italian region. Terra Nova 2, 569–576.

Babuska, V., Plomerova, J., Sileny, J., 1984. Spatial variations of P residuals and deep structure of the European lithosphere. Geophys. J. R. Astron. Soc. 79, 363–384.

Backus, G., Gilbert, J.F., 1970. Uniqueness in the inversion of inaccurate gross earth data. Philos. Trans. R. Soc. A 266, 123–192.

Balyshev, S.O., Ivanov, A.V., 2001. Low-density anomalies in the mantle: ascending plumes and/or heated fossil lithospheric plates? Dokl. Earth Sci. 380, 523–527.

Barzaghi, R., Betti, B., Borghi, A., Sona, G., Tornatore, V., 2002. The Italian quasi-geoid ITALGEO99. Boll. Geod. Sci. Affini. 1, 33–51.

Beccaluva, L., Bonatti, E., Dupuy, C., Ferrara, G., Innocenti, F., Lucchini, F., Macera, P., Petrini, R., Rossi, P.L., Serri, G., Seyler, M., Siena, F., 1990. Geochemistry and mineralogy of the volcanic rocks from ODP sites 650, 651, 655, and 654 in the Tyrrhenian Sea. In: Kastens, K.A., Mascle, J., et al. (Eds.), Proc. Ocean Drilling Program, Scientific Results, 107, 49–74.

Behncke, B., 2001. Volcanism in the Southern Apennines and Sicily. In: Vai, G.B., Martini, P.I. (Eds.), Anatomy of an Orogen. The Apennines and the adjacent Mediterranean basins. Kluwer, Dordrecht, pp. 105–120.

Bijwaard, H., Spakman, W., Engdahl, E.R., 1998. Closing the gap between regional and global travel time tomography. J. Geophys. Res. 103, 30055–30078.

Bolt, B.A., Dorman, J., 1961. Phase and group velocity of Rayleigh waves in a spherical gravitating earth. J. Geophys. Res. 66, 2965–2981.

Bottinga, Y., Steinmetz, L., 1979. A geophysical, geochemical, petrological model of the sub-marine lithosphere. Tectonophysics 55, 311–347.

Bryson, Arthur Earl, Ho, Yu-Chi, 1975. Applied Optimal Control: Optimization, Estimation, and Control. Hemisphere, Washington.

Calcagnile, G., Panza, G.F., 1981. The main characteristics of the lithosphere–astenosphere system in Italy and surrounding regions. Pure Appl. Geophys. 119, 865–879.

Calcagnile, G., D'Igeo, F., Farrugia, P., Panza, G.F., 1982. The lithosphere in the central–eastern Mediterranea area. Pure Appl. Geophys. 120, 389–406.

Carminati, E., Wortel, M.J.R., Spakman, W., Sabadini, R., 1998. The role of slab detachment processes in the opening of the western–central Mediterranean basins: some geological and geophysical evidence. Earth Planet. Sci. Lett. 160, 651–665.

Cavazza, W., Wezel, F.C., 2003. The Mediterranean region. A geological primer. Episodes 26, 160–168.

Čermak, V., Bodri, L., 1998. Heat flow map of Europe revisited. In: Clauser, C. (Ed.), Mitteilungen DGG, Sonderband II/1998, pp. 58–63.

Chimera, G., Aoudia, A., Saraò, A., Panza, G.F., 2003. Active tectonics in central Italy: constraint from surface wave tomography and source moment tensor inversion. Phys. Earth Planet. Inter. 138, 241–262.

Christensen, M.I., Mooney, W.D., 1995. Seismic velocity structure and composition of the continental crust: a global view. J. Geophys. Res. 100, 9761–9788.

Cimini, G.B., De Gori, P., 1997. Upper mantle velocity structure beneath Italy from direct and secondary P-wave teleseismic tomography. Annali di Geofis. XL (1), 175–194.

Cinque, A., Civetta, L., Orsi, G., Peccerillo, A., 1988. Geology and geochemistry of the Island of Ustica (Southern Tyrrhenian Sea). Boll. Soc. Ital. Miner. Petrol. 43, 987–1002.

Clayton, R.W., 1984. Seismic tomography. Eos, Trans. Am. Geophys. Union 65, 236.

Clayton, R.W., Comer, R.P., 1984. A tomographic analysis of mantle heterogeneities. Terra Cogn. 4, 282–283.

Conticelli, S., Peccerillo, A., 1992. Petrology and geochemistry of potassic and ultrapotassic volcanism from Central Italy: inferences on its genesis and on the mantle source evolution. Lithos 28, 221–240.

Conticelli, S., D'Antonio, M., Pinarelli, L., Civetta, L., 2001. Source contamination and mantle heterogeneity in the genesis of Italian potassic and ultrapotassic rocks: Sr–Nd–Pb isotope data from Roman Province and southern Tuscany. Mineral. Petrol. 74, 189–222.

Cristofolini, R., Menzies, M.A., Beccaluva, L., Tindle, A., 1987. Petrological notes on the 1983 lavas at Mount Etna, Sicily, with reference to their REE and Sr–Nd isotopic composition. Bull. Volcanol. 49, 599–607.

Crosson, R.S., 1976. Crustal structure modelling of earthquake data. Part 1. Simultaneous least squares estimation of hypocenter and velocity parameters. J. Geophys. Res. 81, 3036–3046.

De Astis, G., La Volpe, L., Peccerillo, A., Civetta, L., 1997. Volcanological and petrological evolution of Vulcano island (Aeolian arc, southern Tyrrhenian Sea). J. Geophys. Res. 102, 8021–8050.

De Astis, G., Peccerillo, A., Kempton, P.D., La Volpe, L., Wu, T.W., 2000. Transition from calcalkaline to potassium-rich magmatism in subduction environments: geochemical and Sr, Nd, Pb isotopic constraints from the Island of Vulcano (Aeolian arc). Contrib. Mineral. Petrol. 139, 684–703.

De Astis, G., Kempton, P.D., Pecherillo, A., Wu, T.W., in press. Trace element and isotopic variations from Mt. Vulture to Campanian volcanoes: constraints for slab detachment and mantle inflow beneath southern Italy. Contrib. Mineral. Petrol., doi:10.1007/s00410–006–0062-y.

De Fino, M., La Volpe, L., Peccerillo, A., Piccarreta, G., Poli, G., 1986. Petrogenesis of Monte Vulture volcano (Italy): inferences from mineral chemistry, major and trace element data. Contrib. Mineral. Petrol. 92, 135–145.

De Gori, P., Cimini, G.B., Chiarabba, C., De Natale, G., Troise, C., Deschamps, A., 2001. Teleseismic tomography of the Campanian volcanic area and surrounding Apenninic belt. J. Volc. Geotherm. Res. 109, 55–75.

deGroot-Hedlin, C., Constable, S., 1990. Occam's inversion to generate smooth, two-dimensional models from magnetotelluric data. Geophysics 55, 1613–1624.

Della Vedova, B., Bellani, S., Pellis, G., Squarci, P., 2001. Deep temperatures and surface heat flow distribution. In: Vai, G.B., Martini, I.P. (Eds.), Anatomy of an orogen, The Apennines and adjacent Mediterranean basins. Kluwer Acad. Publ., Dordrecht, The Netherlands, pp. 65–76.

Della Vedova, B., Marson, I., Panza, G.F., Suhadolc, P., 1991. Upper mantle properties of the Tuscan–Tyrrhenian area: a framework for its recent tectonic evolution. Tectonophysics 195, 311–318.

De Paolo, D.J., 1981. Trace elements and isotopic effects of combined wallrock assimilation and fractional crystallisation. Earth Planet. Sci. Lett. 53, 189–202.

Ditmar, P.G., Yanovskaya, T.B., 1987. A generalization of the Backus–Gilbert method for estimation of lateral variations of surface wave velocity. Izv. AN SSSR, Fiz. Zemli (Physics of the Solid Earth) 23, 470–477.

Doglioni, C., Harabaglia, P., Merlini, S., Mongelli, F., Peccerillo, A., Piromallo, C., 1999. Orogens and slabs vs. their direction of subduction. Earth-Sci. Rev. 45, 167–208.

Doglioni, C., Innocenti, F., Mariotti, G., 2001. Why Mt Etna? Terra Nova 13, 25–31.

Du, Z.J., Michelini, A., Panza, G.F., 1998. EurID: a regionalised 3-D seismological model of Europe. Phys. Earth Planet. Inter. 105, 31–62.

Dziewonski, A.M., Hales, A.L., 1972. Numerical analysis of dispersed seismic waves. In: Bolt, B.A. (Ed.), Meth. Comp. Phys., vol. 11. Academic Press, pp. 39–72.

Dziewonski, A.M., Hager, B.H., O'Connell, R.J., 1977. Large-scale heterogeneities in the lower mantle. J. Geophys. Res. 82, 239–255.

Edgar, A.D., 1987. The genesis of alkaline magmas with emphases on their source region: inferences from experimental studies. In: Fitton, J.G., Upton, B.G.J. (Eds.), Alkaline igneous rocks. Geol. Soc. Spec. Publ., 30, 205–220.

Faccenna, C., Piromallo, C., Crespo-Blanc, A., Jolivet, L., Rossetti, F., 2004. Lateral slab deformation and the origin of the western Mediterranean arcs. Tectonics 23 (1), TC1012.

Farina, B., 2006. Lithosphere–asthenosphere system in Italy and surrounding areas: optimized non-linear inversion of surface-wave dispersion curves and modelling of gravity Bouguer anomalies, PhD Thesis, University of Trieste, 274 pp.

Foley, S.F., Wheller, G.E., 1990. Parallels in the origin of the geochemical signature of island-arc volcanics and continental potassic igneous rocks: the role of residual titanates. Chem. Geol. 85, 1–18.

Foulger, G.R., Nathland, G.H., Presnall, D.C., Anderson, D.L. (Eds.), 2005. Plates, plumes, and paradigms. Geol. Soc. Am. Spec. Paper, vol. 388, 881 pp.

Fowler, C.M.R., 1995. The Solid Earth. An introduction to Global Geophysics. Cambridge Univ. Press.

Francalanci, L., Tommasini, S., Conticelli, S., Davies, G.R., 1999. Sr sotope evidence for short magma residence time for the 20th century activity at Stromboli volcano, Italy. Earth Planet. Sci. Lett. 167, 61–69.

Frezzotti, M.L., Peccerillo, A., Bonelli, R., 2003. Magma ascent rates and depths of crustal magma reservoirs beneath the Aeolian volcanic arc (Italy): inferences from fluid and melt inclusions in xenoliths. In: De Vivo, B., Bodnar, R.J. (Eds.), Melt Inclusions in Volcanic Systems: Methods, Applications and Problems. Elsevier, Amsterdam, pp. 185–205.

Gaetani, G.A., Grove, T.L., 1998. The influence of water on melting of mantle peridotite. Contrib. Mineral. Petrol. 131, 323–346.

Gasperini, D., Blichert-Toft, J., Bosch, D., Del Moro, A., Macera, P., Télouk, P., Albaréde, F., 2000. Evidence from Sardinian basalt geochemistry for recycling of plume heads into the Earth's mantle. Nature 408, 701–704.

Gasperini, D., Blichert-Toft, J., Bosch, D., Del Moro, A., Macera, P., Albaréde, F., 2002. Upwelling of deep mantle material through a plate window: evidence from the geochemistry of Italian basaltic volcanics. J. Geophys. Res. 107, 2367–2386.

Gauthier, P.J., Condomines, M., 1999. ^{210}Pb–^{226}Ra radioactive disequilibria in recent lavas and radon degassing: inferences on the magma chamber dynamics at Stromboli and Merapi volcanoes. Earth Planet. Sci. Lett. 172, 111–126.

Gioncada, A., Mazzuoli, R., Bisson, M., Pareschi, M.T., 2003. Petrology of volcanic products younger than 42 ka on the Lipari–Vulcano complex (Aeolian Islands, Italy): an example of volcanism controlled by tectonics. J. Volcanol. Geotherm. Res. 122, 191–220.

Gobarenko, V.S., Nikolova, S.B., Sokolova, S.J., 1990. Velocity structure of the western Mediterranean from inversion of P-wave traveltimes. Geophys. J. Int. 101, 557–564.

Graham, E.K., 1970. Elasticity and composition of the upper mantle. Geophys. J. R. Astron. Soc. 20, 285–302.

Green, D.H., Falloon, T.J., 2005. Primary magmas at mid-ocean ridges, "hotspots", and other intraplate settings: constraints on mantle potential temperature. In: Foulger, G.R., Nathland, G.H., Presnall, D.C., Anderson, D.L. (Eds.), Plates, plumes, and paradigms. Geol. Soc. Am. Spec. Paper, 388, 215–247.

Gudfinnsson, G.H., Presnall, D.C., 2005. Continuous gradation among primary carbonatitic, kimberlitic, melilititic, basaltic, picritic and komatiitic melts inequilibrium with garnet lherzolite at 3–8 GPa. J. Petrol. 46, 1645–1659.

Guidarelli, M., Saraò, A., Panza, G.F., 2002. Surface wave tomography and seismic source studies at Campi (Italy). Phys. Earth Planet. Inter. 134, 157–173.

Gupta, A.K., Fyfe, W.S., 2003. The young potassic rocks. Ane Books, New Delhi, 370 pp.

Gvirtzman, Z., Nur, A., 1999. The formation of Mount Etna as the consequence of slab rollback. Nature 401, 782–785.

Hoernle, K., Behncke, B., Schmincke, H.-U., 1996. The geochemistry of basalt from the Iblean Hills (Sicily) and the Island of Linosa (Strait of Sicily): evidence for a plume from the lower mantle. Goldschmidt Conf. J. Conf. Abstr. 1, 264 www.the-conference.com/JConfAbs/1/264.html.

Hofmann, A., 1997. Mantle geochemistry: the message from oceanic volcanism. Nature 385, 219–229.

ISC. International Seismological Centre On-line Bulletin, http://www.isc.ac.uk/Bull, Internat. Seis. Cent., Thatcham, United Kingdom, 2001.

Ismail-Zadeh, A.T., Aoudia, A., Panza, G.F., 2004. Tectonic stress in the Central Apennines due to lithospheric buoyancy. Trans. (Dokl.) USSR Acad. Sci., Earth Sci. Sect. 395, 369–372.

Ivansson, S., 1983. Remark on an earlier proposed iterative tomographic algorithm. Geophys. J. R. Astron. Soc. 75, 855–860.
Iyer, H.M., Hirahara, K. (Eds.), 1993. Seismic Tomography. Chapman & Hall, London.
Karagianni, E.E., Panagiotopoulos, D.G., Panza, G.F., Suhadolc, P., Papazachos, C.B., Papazachos, B.C., Kiratzi, A., Hatzfeld, D., Makropoulos, K., Priestley, K., Vuan, A., 2002. Rayleigh wave group velocity tomography in the Aegean area. Tectonophysics 358, 187–209.
Kessel, R., Schmidt, M.W., Ulmer, P., Pettke, T., 2005. Trace element signature of subduction-zone fluids, melts and supercritical liquids at 120–180 km depth. Nature 437, 724–727.
Knopoff, L., 1972. Observations and inversion of surface-wave dispersion. In: Ritsema, A.R. (Ed.), The Upper Mantle. Tectonophysics, 13, 497–519.
Knopoff, L., Panza, G.F., 1977. Resolution of upper mantle structure using higher modes of Rayleigh waves. Ann. Geophys. 30, 491–505.
Konzett, J., Ulmer, P., 1999. The stability of hydrous potassic phases in lherzolitic mantle—an experimental study to 9.5 GPa in simplified and natural bulk compositions. J. Petrol. 40, 629–652.
Kushiro, I., 1990. Partial melting of mantle wedge and evolution of island arc crust. J. Geophys. Res. 95, 15929–15939.
Lee, C.-T., Yin, Q.-Z., Rudnick, R.L., Jacobsen, S.B., 2001. Preservation of ancient and fertile lithospheric mantle beneath the southwestern United States. Nature 411, 69–73.
Le Maitre, R.W. (Ed.), 1989. A Classification of Igneous Rocks and Glossary of Terms. Blackwell, Oxford, 193 pp.
Levshin, A.L., Pisarenko, V.F., Pogrebinsky, G.A., 1972. On a frequency time analysis of oscillations. Ann. Geophys. 28, 211–218.
Levshin, A.L., Ratnikova, L., Berger, J., 1992. Peculiarities of surface wave propagation across Central Eurasia. Bull. Seismol. Soc. Am. 82, 2464–2493.
Locardi, E., 1993. Dynamics of deep structures in the Tyrrhenian–Apennines area and its relation to neotectonics. Il Quaternario 6, 59–66.
Lucente, F.P., Chiarabba, C., Cimini, G.B., Giardini, D., 1999. Tomographic constraints on the geodynamic evolution of the Italian region. J. Geophys. Res. 104, 20307–20327.
Ludwig, W.J., Nafe, J.E., Drake, C.L., 1970. Seismic refraction. The Sea, vol. 4 (Part 1). Wiley-Intersci., New York, pp. 53–84.
Lustrino, M., Dallai, L., 2003. On the origin of EM-I end-member: Neues Jahrb. Mineral. Abh. 179, 85–100.
Lustrino, M., Morra, V., Melluso, L., Brotzu, P., D'Amelio, F., Fedele, L., Lonis, R., Franciosi, L., Petteruti Liebercknect, A.M., 2004. The Cenozoic igneous activity in Sardinia. Period. Mineral. 73, 105–134.
Maguire, P.K.H., Francis, D.J., Whitcombe, D.N., 1985. Determination of the three dimensional seismic structure of the crust and upper mantle in the central midlands of England. Geophys. J. R. Astron. Soc. 83, 347–362.
Mantovani, E., Albarello, D., Tamburelli, C., Babbucci, D., Viti, M., 1997. Plate convergence, crustal delamination, extrusion tectonics and minimization of shortening work as main controlling factors of the recent Mediterranean deformation pattern. Ann. Geophys. 40, 611–643.
Mantovani, E., Albarello, D., Babbucci, D., Tamburelli, C., Viti, M., 2002. Trench–arc–backarc systems in the Mediterranean area: examples of extrusion tectonics. J. Virtual Explorer 8, 131–147.
Marquering, H., Snieder, R., 1996. Shear-wave velocity structure beneath Europe, the north-eastern Atlantic and western Asia from waveform inversion including surface-wave mode coupling. Geophys. J. Int. 127, 283–304.
Marra, F., Taddeucci, J., Freda, C., Marzocchi, W., Scarlato, P., 2004. Recurrence of volcanic activity along the Roman Comagmatic Province (Tyrrhenian margin of Italy) and its tectonic significance. Tectonics 23, TC 4013. doi:10.1029/2003TC001600.
Martinez, M.D., Lana, X., Badal, J., Canas, J.A., Pujades, L., 1997. Preliminary objective regionalization of the Mediterranean basin derived from surface-wave tomography. Ann. Geofis. XL (1), 43–59.
Martinez, M.D., Lana, X., Canas, J.A., Badal, J., Pujades, L., 2000. Shear-wave velocity tomography of the lithosphere–asthenosphere system beneath the Mediterranean area. Phys. Earth Planet. Inter. 122, 33–54.
Martinez, M.D., Canas, J.A., Lana, X., Badal, J., 2001. Objective regionalization of Rayleigh wave dispersion data by clustering algorithms: an application to the Mediterranean basin. Tectonophysics 330, 245–266.
McNutt, M.K., 1998. Superswells. Rev. Geophys. 36, 211–244.
Meletti, C., Patacca, E., Scandone, P., 2000. Construction of a seismotectonic model: the case of Italy. Pure Appl. Geophys. 157, 11–35.
Melzer, S., Foley, S.F., 2000. Phase relations and fractionation sequences in potassic magma series modelled in the system $CaMgSi_2O_6$–$KAlSiO_4$–Mg_2SiO_4–F at 1 bar to 18 kbar. Contrib. Mineral. Petrol. 138, 186–197.
Menzies, M.A., 1990. Continental mantle. Oxford University Press, Oxford, 184 pp.
Mitchell, B.S., Cheng, C.C., Stauder, W., 1977. A three dimensional velocity model of the lithosphere beneath the Madrid seismic zone. Bull. Seismol. Soc. Am. 62, 1061–1074.
Moritz, 1995. Science, mind and the universe, Wichmann. 298 pp.
Natale, M., Nunziata, C., Panza, G.F., 2005. Average shear wave velocity models of the crustal structure at Mt. Vesuvius. Phys. Earth Planet. Inter. 152, 7–21.
Nazareni, S., Molin, G., Peccerillo, A., Zanazzi, P.F., 1998. Structural and chemical variations in clinopyroxenes from the Island of Alicudi (Aeolian Arc) and their implications for conditions of crystallization. Eur. J. Mineral. 10, 291–300.
Nazareni, S., Molin, G., Peccerillo, A., Zanazzi, P.F., 2001. Volcanological implications of crystal–chemical variations in clinopyroxenes from the Aeolian Arc, Southern Tyrrhenian Sea (Italy). Bull. Volcanol. 63, 73–82.
Nicolich, R., Dal Piaz, R., 1990. Moho isobaths. Structural Model of Italy and Gravity Map. Sheet 2. Consiglio Nazionale delle Ricerche.
Nixon, P.H., 1987. Mantle xenoliths. Wiley, Chichester, 844 pp.
Nolet, G., 1984. Damped least squares methods to solve large tomographic systems and determine the resolving power. Terra Cogn. 4, 285.
Nolet, G., 1985. Solving or resolving inadequate and noisy tomographic systems. J. Comp. Phys. 61, 463–482.
Nolet, G., 1987. In: Nolet, G., Reidel, D. (Eds.), Seismic tomography with applications in global seismology and exploration geophysics. Publ. Company, Dordrecht, Holland.
Panza, G.F., 1976. Phase velocity determination of fundamental Love and Rayleigh waves. Pure Appl. Geophys. 114, 753–764.
Panza, G.F., 1978. The crust and upper mantle in southern Italy from geophysical data. Riv. Ital. Geofis. Sci. Affini. V, 17–22.
Panza, G.F., 1980. Evolution of the Earth's lithosphere. NATO Adv. Stud. Inst. Newcastle, 1979. In: Davies, P.A., Runcorn, S.K. (Eds.), Mechanisms of Continental Drift and Plate Tectonics. Academic Press, pp. 75–87.
Panza, G.F., 1981. The resolving power of seismic surface waves with respect to crust and upper mantle structural models. In: Cassinis, R. (Ed.), The solution of the inverse problem in geophysical interpretation. Plenum Publ. Corp., pp. 39–77.

Panza, G.F., 1984. Contributi geofisici alla geologia: stato attuale dell'arte e prospettive future. Cento anni di geologia italiana. Vol. giub. I Centenario S.G.I., Bologna, pp. 363–376.

Panza, G.F., Pontevivo, A., 2004. The Calabrian Arc: a detailed structural model of the lithosphere–asthenosphere system. Rend. Acc. Naz. XL (XXXVIII), 51–88.

Panza, G.F., Calcagnile, G., Scandone, P., Mueller, S., 1980a. La struttura profonda dell'area mediterranea. Le Scienze 141, 60–69.

Panza, G.F., Mueller, S., Calcagnile, G., 1980b. The gross features of the lithosphere–asthenosphere system in Europe from seismic surface waves and body waves. Pure Appl. Geophys. 118, 1209–1213.

Panza, G.F., Mueller, S., Calcagnile, G., Knopoff, L., 1982. Delineation of the north central Italian upper mantle anomaly. Nature 296, 238–239.

Panza, G.F., Pontevivo, A., Chimera, G., Raykova, R., Aoudia, A., 2003. The lithosphere–astenosphere: Italy and surroundings. Episodes 26, 168–173.

Panza, G.F., Pontevivo, A., Saraò, A., Aoudia, A., Peccerillo, A., 2004. Structure of the lithosphere–asthenosphere and volcanism in the Tyrrhenian Sea and surroundings. Mem. Serv. Geol. 64, 29–56.

Papazachos, C.B., Kiratzi, A.A., 1996. A detailed study of the active crustal deformation in the Aegean and surrounding area. Tectonophysics 253, 129–153.

Papazachos, C.B., Hatzidimitriou, P.M., Panagiotopoulos, D.G., Tsokas, G.N., 1995. Tomography of the crust and upper mantle in southeast Europe. J. Geophys. Res. 100 (B7), 12405–12422.

Parolai, S., Spallarossa, D., Eva, C., 1997. Bootstrap inversion for P_n wave velocity in North-Western Italy. Ann. Geofis. XL (1), 133–150.

Pasyanos, M.E., Walter, W.R., Hazler, S.E., 2001. A surface wave dispersion study of the Middle East and North Africa for monitoring the Compressive Nuclear–Test–Ban Treaty. Pure Appl. Geophys. 158, 1445–1474.

Payo Subiza, G., 1967. Crustal structure of the Mediterranean Sea by surface waves-pt. 1, group velocity. Bull. Seismol. Soc. Am. 57, 151–172.

Payo Subiza, G., 1969. Crustal structure of the Mediterranean Sea by surface waves-pt. 2, group velocity. Bull. Seismol. Soc. Am. 59, 23–42.

Peccerillo, A., 1999. Multiple mantle metasomatism in central–southern Italy: geochemical effects, timing and geodynamic implications. Geology 27, 315–318.

Peccerillo, A., 2001a. Geochemistry of Quaternary magmatism in central–southern Italy: genesis of primary melts and interaction with crustal rocks. Geochem. Int. 39, 521–535.

Peccerillo, A., 2001b. Geochemical affinities between Vesuvius, Phlegraean Fields and Stromboli volcanoes: petrogenetic, geodynamic and volcanological implications. Mineral. Petrol. 73, 93–105.

Peccerillo, A., 2003. Plio-Quaternary magmatism in Italy. Episodes 26, 222–226.

Peccerillo, A., 2005. Plio-Quaternary volcanism in Italy. Petrology, geochemistry, geodynamics. Springer, Heidelberg. 365 pp.

Peccerillo, A., 2006. Carbonatites vs. carbonated rocks in central Italy. A reply to comments by Bell and Kjarsgaard. Period. Mineral. 75, 93–100.

Peccerillo, A., Martinotti, G., 2006. The Western Mediterranean lamproitic magmatism: origin and geodynamic significance. Terra Nova 18, 109–117.

Peccerillo, A., Panza, G.F., 1999. Upper mantle domains beneath Central–Southern Italy: petrological, geochemical and geophysical constraints. Pure Appl. Geophys. 156, 421–443.

Peccerillo, A., Poli, G., Serri, G., 1988. Petrogenesis of orenditic and kamafugitic rocks from Central Italy. Can. Mineral. 26, 45–65.

Pilant, W.L., 1979. Elastic waves in the Earth. Developments in Solid Earth Geophysics, vol. 11. Elsevier Scientific Publish. Company, Amsterdam.

Piromallo, C., Morelli, A., 1997. Imaging the Mediterranean upper mantle by P-wave travel time tomography. Ann. Geofis. 40, 963–979.

Plomerova, J., 1997. Seismic anisotropy in tomographic studies of the upper mantle beneath southern Europe. Ann. Geofis. XL (1), 111–121.

Poli, G., 1992. Geochemistry of Tuscan Archipelago granitoids, Central Italy: the role of hybridization processes in their genesis. J. Geol. 100, 41–56.

Poli, G., Peccerillo, A., Donati, C., 2002. The Plio-Quaternary acid magmatism of Southern Tuscany. In: Barchi, R.M., Cirilli, S., Minelli, G. (Eds.), Geological and Geodynamic Evolution of the Apennines. Boll. Soc. Geol. Ital. Spec., vol. 1, pp. 143–151.

Pontevivo, A., 2003. Surface-wave tomography and non-linear inversion in Italy and surrounding areas. Ph.D. thesis, University of Trieste.

Pontevivo, A., Panza, G.F., 2002. Group velocity tomography and regionalization in Italy and bordering areas. Phys. Earth Planet. Inter. 134, 1–15.

Presnal, D.C., 1979. Fractional crystallisation and partial fusion. In: Yoder Jr., H.S. (Ed.), The evolution of igneous rocks. Fiftieth anniversary perspective. Princeton Univ. Press, pp. 59–75.

Raykova, R., Chimera, G., Farina, B., Panza, G. S-wave velocity structure of the lithosphere–asthenosphere system in Mediterranean region. 32th International Geological Congress — August, 2004, Florence, Italy, Abs. Vol., Pt.2, abs. 208–5, p. 970.

Ringwood, A.E., 1966. Mineralogy of the mantle. In: Hurley, P.M. (Ed.), Advances in Earth Science. MIT Press, pp. 357–399.

Ritzwoller, M.H., Levshin, A.L., 1998. Eurasian surface wave tomography: group velocities. J. Geophys. Res. 103 (B3), 4839–4878.

Rodi, W., Glover, P., Li, T.M.C., Alexander, S.S., 1975. A fast, accurate method for computing group-velocity partial derivatives for Raylegh and Love waves. Bull. Seismol. Soc. Am. 65 (5), 1105–1114.

Rollinson, H., 1998. Using geochemical data: evaluation, presentation, interpretation. Longman, Singapore, 352 pp.

Romanowicz, B.A., 1979. Seismic structure of the upper mantle beneath the United States by three dimensional inversion of body wave arrival times. Geophys. J. R. Astron. Soc. 57, 479–506.

Rotolo, S.G., Castorina, F., Cellura, D., Pompilio, M., 2006. Petrology and geochemistry of submarine volcanism in the Sicily Channel rift. J. Geol. 114, 355–365.

Russell, B., 1946. History of western philosophy. George Allen and Unwin, Ltd.

Sartori, R., 2003. The Thyrrhenian backarc basin and subduction of the Ionian lithosphere. Episodes 26, 217–221.

Savelli, C., 1988. Late Oligocene to Recent episodes of magmatism in and around the Tyrrhenian Sea: implications for the processes of opening in a young inter-arc basin of intra-orogenic (Mediterranean) type. Tectonophysics 146, 163–181.

Shapiro, N.M., Ritzwoller, M.H., 2002. Monte-Carlo inversion for a global shear velocity model of the crust and upper mantle. Geophys. J. Int. 151, 88–105.

Shaw, D.M., 1970. Trace element fractionation during anatexis. Geochim. Cosmochim. Acta 34, 237–243.

Snieder, R., 1988. Large scale waveform inversions of surface waves for lateral heterogeneity 2. Application to surface waves in Europe and the Mediterranean. J. Geophys. Res. 93 (B10), 12067–12080.

Snieder, R., 1996. Surface wave inversion on a regional scale. In: Boschi, E., Ekstrom, G., Morelli, A. (Eds.), Seismic modelling of Earth structure.

Spakman, W., 1986. Subduction beneath Eurasia in connection with the Mesozoic Tethys. Geol. Mijnb. 65, 145–153.
Spakman, W., 1990. Tomographic images of the upper mantle below central Europe and the Mediterranean. Terra Nova 2, 542–553.
Spakman, W., Wortel, R., 2004. A tomographic view on Western Mediterranean geodynamics. In: Cavazza, W., Roure, Spakman, W., Stampfli, G.M., Ziegler, P.A (Eds.), The TRANSMED atlas, Springer, Heidelberg, pp. 31–52.
Stoppa, F., Woolley, A.R., 1997. The Italian carbonatites: field occurrence, petrology and regional significance. Mineral. Petrol. 59, 43–67.
Stracke, A., Hofmann, A., Hart, S.R., 2005. FOZO, HIMU and the rest of the mantle zoo. Geochem. Geophys. Geosyst. 6, Q05007. doi:10.1029/2004GC000824.
Taylor, H.P., Sheppard, S.M.F., 1986. Igneous rocks: I. Processes of isotopic fractionation and isotope systematics. Rev. Mineral. 16, 227–271.
Taylor, S.R., Toksoz, M.N., 1979. Three dimensional crust and upper mantle structure of the north-eastern United States. J. Geophys. Res. 84, 7627–7644.
Trua, T., Esperança, S., Mazzuoli, R., 1998. The evolution of the lithospheric mantle along the North African Plate: geochemical and isotopic evidence from the tholeiitic and alkaline volcanic rocks of the Hyblean Plateau, Italy. Contrib. Mineral. Petrol. 131, 307–322.
Trua, T., Serri, G., Marani, M.P., Renzulli, A., Gamberi, F., 2002. Volcanological and petrological evolution of Marsili Seamount (Southern Tyrrhenian Sea). J. Volcanol. Geotherm. Res. 114, 441–464.
Trua, T., Serri, G., Marani, M.P., 2003. Lateral flow of African mantle below the nearby Tyrrhenian plate: geochemical evidence. Terra Nova 15, 433–440.
Ulmer, P., Trommsdorff, V., 1995. Serpentine stability to mantle depths and subduction related magmatism. Science 268, 858–861.
Urban, L., Cichowicz, A., Vaccari, F., 1993. Computation of analytical partial derivatives of phase and group velocities for Rayleigh waves with respect to structural parameters. Stud. Geophys. Geod. 37, 14–36.
Valyus, V.P., 1972. Determining seismic profiles from a set of observations. In: Keilis-Borok (Ed.), Computational Seismology. Consult. Bureau, New-York, pp. 114–118.
Valyus, V.P., Keilis-Borok, V.I., Levshin, A., 1969. Determination of the upper-mantle velocity cross-section for Europe. Proc. Acad. Sci. USSR 185, 3.
Venisti, N., Calcagnile, G., Pontevivo, A., Panza, G.F., 2005. Tomographic study of the Adriatic plate. Pure Appl. Geophys. 162, 311–329.
Voltaggio, M., Barbieri, M., 1995. Geochronology. In: Trigila, R. (Ed.), The volcano of the Alban Hills. University La Sapienza, Rome, pp. 167–192.
Washington, H.S., 1906. The Roman Comagmatic Region, vol. 57. Carnegie Inst. Washington, Publ. 199 pp.
Wendlandt, R.F., Eggler, D.H., 1980. The origin of potassic magmas: stability of phlogopite in natural spinel lherzolite an in the $KAlSiO_4$–MgO–SiO_2–H_2O–CO_2 at high pressures and high temperatures. Am. J. Sci. 280, 421–458.
Westway, R., 1993. Quaternary uplift in Southern Italy. J. Geophys. Res. 98, 21741–21772.
Wilson, M., 1988. Igneous petrogenesis. Unwin Hyman, London, 465 pp.
Yanovskaya, T.B., 2001. In: Keilis-Borok, V.I., Molchan, G.M. (Eds.), Development of methods for surface-wave tomography based on Backus–Gilbert approach. Computational Seismology, vol. 32, pp. 11–26.
Yanovskaya, T.B., 1982. Distribution of surface wave group velocities in the North Atlantic. Izv. AN SSSR, Fiz. Zemli 2, 3–11.
Yanovskaya, T.B., 1984. Solution of the inverse problem of seismology for laterally inhomogeneous media. Geophys. J. R. Astron. Soc. 79, 293–304.
Yanovskaya, T.B., 1997. Resolution estimation in the problems of seismic ray tomography. Izv., Phys. Solid Earth 33 (9), 762–765.
Yanovskaya, T.B., Ditmar, P.G., 1990. Smoothness criteria in surface-wave tomography. Geophys. J. Int. 102, 63–72.
Yanovskaya, T.B., Kizima, E.S., Antonova, L.M., 1998. Structure of the crust in the Black Sea and adjoining regions from surface wave data. J. Seismol. 2, 303–316.
Yanovskaya, T.B., Panza, G.F., Ditmar, P.D., Suhadolc, P., Mueller, S., 1990. Structural heterogeneity and anisotropy based on 2-D phase velocity pattern of Rayleigh waves in Western Europe. Rend. Fis. Acc. Lincei 9 (1), 127–135.
Yanovskaya, T.B., Antonova, L.M., Kozhevnikov, V.M., 2000. Lateral variations of the upper mantle structure in Eurasia from group velocities of surface waves. Phys. Earth Planet. Inter. 122, 19–32.
Yoder Jr., H.S., 1976. Generation of Basaltic Magmas. National Academy of Science, Washington. D.C, 256 pp.
Zanon, V., Frezzotti, M., Peccerillo, A., Nikogossian, I., 2003. Magmatic feeding system and crustal magma accumulation beneath Vulcano Island (Italy): evidence from fluid inclusions in quartz xenoliths. J. Geophys. Res. 108 (B6), 2298–2313.
Zhdanov, M., 2002. Geophysical Inverse Theory and Regularization Problems. Elsevier, 628 pp.
Zindler, A., Hart, S.R., 1986. Chemical geodynamics. Annu. Rev. Earth Planet. Sci. 14, 493–571.

List of acronyms

Di: diopside
DMM: depleted MORB mantle
EM1: enriched mantle 1
EM2: enriched mantle 2
En: enstatite
Fo: forsterite
FOZO: Focus Zone
HFSE: elements with high ratios between charge and ionic radius: Ta, Nb, Zr, Hf, Ti
HIMU: High μ (μ=U/Pb)
HKS: ultrapotassic series
kal: kalsilite
KS: potassic series
LAS: Lithosphere–Asthenosphere System
lc: leucite
LILE: Large Ion Lithophile Elements
LREE: Light Rare Earth Elements
MORB: Mid-Ocean Ridge Basalt
ne: nepheline
OBS: Ocean Bottom Seismograms
OIB: Oceanic Island Basalt
ol: olivine
q: quartz
REE: Rare Earth Element
T: temperature
TAS: Total Alkali vs. Silica
V_p: body-wave velocity
V_s: shear wave velocity